

Department of Physics and Astronomy
University of Heidelberg

Master Thesis
in Physics
submitted by
Lucas Altenkämper
born in Freiburg (Germany)
2016

Measurement of Direct Photons
in Proton-Proton Collisions at $\sqrt{s} = 7$ TeV
with ALICE

This Master Thesis has been carried out by Lucas Altenkämper at the
Physikalisches Institut at the University of Heidelberg
under the supervision of
Prof. Dr. Klaus Reygers

Measurement of Direct Photons in Proton-Proton Collisions at $\sqrt{s} = 7$ TeV with ALICE:

In this thesis, direct photons are analyzed in proton-proton collisions at a center-of-mass energy of 7 TeV at the LHC. The data was recorded by the ALICE detector in 2010 and the analyzed sample consists of about 420×10^6 minimum bias events. The direct photon signal is quantified with the direct photon excess ratio that makes use of the reconstructed photons and neutral pions. Hereby, the reconstruction is done with two distinct methods that are the photon conversion method and the reconstruction using the ALICE EMCal. The measurement with the conversion method is a re-analysis of previous results for which now a more recent reconstruction of the data and more statistics are available. The reconstruction with the calorimeter is a first attempt at the measurement with the EMCal, which has not been done before. Systematic uncertainties are determined for the measurement with the conversion method and no significant excess of direct photons is found. The results of the conversion method are compared to the previous results and show a reduced systematic uncertainty as well as an extended range in transverse momentum.

Messung Direkter Photonen in Proton-Proton Kollisionen bei $\sqrt{s} = 7$ TeV mit ALICE:

Diese Arbeit beschreibt die Analyse direkter Photonen in Proton-Proton Kollisionen bei einer Schwerpunktsenergie von 7 TeV am LHC. Die Daten wurden vom ALICE Detektor im Jahr 2010 aufgezeichnet und der analysierte Datensatz umfasst ungefähr 420×10^6 Ereignisse mit minimalem Bias. Das Signal direkter Photon wird mit dem Überschussverhältnis direkter Photonen quantifiziert, das auf den rekonstruierten Photonen und neutralen Pionen basiert. Die Rekonstruktion wird dabei mit zwei verschiedenen Methoden durchgeführt, bei denen es sich um die Photonkonversionsmethode und die Rekonstruktion mit dem ALICE EMCal handelt. Die Messung mit der Photonkonversionsmethode ist die Wiederholung einer schon bestehenden Messung, der nun mehr Statistik und eine aktuellere Rekonstruktion der Daten zur Verfügung steht. Die Rekonstruktion mit dem Kalorimeter ist ein erster Versuch der Messung mit dem EMCal, welches bisher nicht zur Messung direkter Photonen genutzt wurde. Für die Konversionsmethode wurden die systematische Unsicherheiten der Messung bestimmt und kein signifikantes Signal direkter Photonen wurde gefunden. Im Vergleich zu den vorherigen Ergebnissen zeigt sich eine Verringerung der systematischen Unsicherheit sowie eine größere Reichweite im transversalen Impuls.

Contents

1. Introduction	9
2. Theoretical Background	11
2.1. Quantum Chromodynamics	13
2.2. The Quark Gluon Plasma	15
2.3. Photons in High Energy and Heavy Ion Collisions	18
2.3.1. Photons from Hard Processes	19
2.3.2. Photons from Thermalized Sources	20
2.3.3. The Direct Photon Signal	20
3. The Experimental Setup	23
3.1. The Large Hadron Collider	23
3.2. A Large Ion Collider Experiment (ALICE)	24
3.2.1. Forward Detectors	25
3.2.2. T0 Detector	25
3.2.3. Inner Tracking System	26
3.2.4. Time Projection Chamber	26
3.2.5. Electromagnetic Calorimeter	27
3.2.6. Charged Particle Tracking in the Central Barrel	28
3.3. The Analysis Framework	29
4. Data Samples and Monte Carlo Simulations	31
4.1. Analyzed Data Samples	31
4.2. Event Generators and Monte Carlo Simulations	32
4.3. Quality Assurance	32
4.4. Event Selection	35
5. Inclusive Photon Measurement	37
5.1. Photon Reconstruction using PCM	37
5.1.1. Reconstruction of Secondary Vertices	38
5.1.2. Selection of Electron-Positron Pairs	39
5.1.3. Selection of Photon Candidates	42
5.2. Photon Reconstruction with EMCal	45
5.2.1. Cell Selection and Clusterizer	45
5.2.2. Cluster Selection	46
5.2.3. Cluster Energy Correction	47
5.3. Corrections to Measured Photon Spectra	49
5.3.1. Out-of-Bunch Pileup Correction	49
5.3.2. Secondary Correction	51
5.3.3. Photon Purity	54

5.3.4. Reconstruction Efficiency	56
5.3.5. Photon Conversion Probability	59
5.4. Inclusive Photon Spectrum	60
6. Neutral Pion Reconstruction	63
6.1. Reconstruction and Signal Extraction	63
6.2. Corrections to Measured Spectra	66
6.2.1. Out-of-Bunch Pileup Correction	66
6.2.2. Secondary Correction	67
6.2.3. Acceptance and Efficiency Correction	68
6.3. Inclusive Neutral Pion Spectrum	70
7. Decay Photon Cocktail	73
7.1. Cocktail Input	73
7.2. Decay Simulation	77
7.3. Photon Cocktail Results and Validation	78
8. Direct Photons	81
8.1. Direct Photon Excess Ratio	81
8.2. Systematic Uncertainties	83
8.3. Direct Photon Spectrum	88
9. Summary	91
10. Outlook	93
A. Appendix	97
A.1. Photon DCA_z Distributions	98
A.2. Neutral Pion Invariant Mass Distributions	100
A.3. Cocktail Simulation Input Parametrizations	101

1. Introduction

There is a theory which states that if ever anyone discovers exactly what the Universe is for and why it is here, it will instantly disappear and be replaced by something even more bizarre and inexplicable. There is another theory which states that this has already happened.

Douglas Adams, The Restaurant at the End of the Universe

The strive for a deeper understanding of nature and its underlying laws is fueled by the most peculiar virtues of mankind which are curiosity and wonder. The imprints can be seen in a vivid field of science as well as in popular culture, emphasizing different aspects of the same drive towards knowledge. While popular culture predominantly addresses reasons, natural sciences aim for the understanding of the fundamental laws of nature. These fundamental laws govern our physical world on all scales, from astronomical objects to subatomic particles. Starting from the Rutherford experiment in the early 1900s and the first models of the atom, it is now possible to peek much deeper into the microscopical building blocks of the universe. Modern particle accelerators are able to collide particles at unprecedented energies, allowing the study of the most scarce particles and to set foot onto unknown territory.

With high energy heavy-ion collisions in today's laboratories, it is possible to recreate the conditions the early universe is believed to have passed through shortly after its origin. These conditions are distinguished by an unusual state of matter: the Quark Gluon Plasma (QGP), in which the constituents of ordinary matter are dissolved into a strongly coupled but quasi-free plasma. Hereby, the elementary particles, that usually are bound inside the nuclei, can move freely and hadronic matter ceases to exist. Heavy-ion collisions of sufficient energy are able to provide the extreme conditions in terms of temperature and pressure that are required to cross the phase boundary from hadronic to deconfined matter. The heavy-ion programs started in the 1980s with the Alternating Gradient Synchrotron (AGS) at Brookhaven National Laboratory (BNL) and the Super Proton Synchrotron (SPS) at the European Center for Nuclear Research (CERN), where a QGP was most likely already produced. Present-day particle accelerators like the Relativistic Heavy Ion Collider (RHIC) at BNL and the Large Hadron Collider (LHC) at CERN provide even higher energies and thus allow for a more in-depth study of the extreme forms of matter that are produced. One of the experiments dedicated to the study of the QGP is the A Large Ion Collider Experiment (ALICE) at the CERN LHC.

In this thesis, measurements of the photon production from soft and hard interactions in proton-proton collisions at a center-of-mass energy of 7 TeV are described. Photons are an excellent probe to study the evolution of the QGP in heavy-ion collisions since they will leave the medium mostly unaffected. Proton-proton collisions are hereby used as a baseline to the measurements in heavy-ion collisions to deduce properties of the medium that is produced. The measurements are done using two distinct methods for

the reconstruction of photons: the photon conversion and the calorimeter method. The conversion measurement is a re-analysis of the measurements described in [1], exploiting a more recent reconstruction of the data and the increased statistics. The calorimeter measurement is a first attempt at the reconstruction with the specific calorimeter that is used.

This thesis is structured in the following way: chapter 2 provides the theoretical background that combines a general overview and an emphasized description of photons in high energy and heavy-ion collisions. The third chapter introduces the experimental apparatus with a focus on the different subdetectors of the ALICE experiment that are used in the analysis. This is followed by a description of the analyzed data sets in the fourth chapter. Chapter 5 and 6 introduce the inclusive photon and neutral pion measurement, respectively. The decay photon cocktail, that is a crucial quantity in the measurement of direct photons, is described in chapter 7. The eighth chapter is dedicated to the description of the direct photon signal extraction and the calculation of the systematic uncertainties. Eventually, the thesis is closed with two chapters where the results are summarized and compared as well as an outlook to possible future developments is given.

2. Theoretical Background

At microscopic scales, everything consists solely of particles that are bound together, interact and decay through three fundamental forces of nature: electromagnetism, the weak and the strong force. Ordered by their specific interactions strengths, the strong force is dominating, followed by electromagnetism and the weak force. The interaction strengths, however, inherit a dependency on the momentum transfer of the interaction that is explained on the example of the strong force in section 2.1. There is also a fourth fundamental force, gravity, that keeps for instance the earth in a stable orbit around the sun. Due to its tiny interaction strength, gravity plays a negligible role at the smallest scales and is therefore usually ignored in the realm of particle physics.

The electromagnetic and weak forces, although behaving very differently at low energies, merge into a single force above a unification energy that is of the order of the mass of the Z boson. This electroweak force is described by the Electroweak Theory (EWT), which was first conceived by Sheldon Glashow [2], Steven Weinberg [3] and Abdus Salam [4] in the 1960s. Their work and the prediction of the weak neutral current, that is a consequence thereof, was rewarded with the Nobel Prize in Physics in 1979. The EWT was the first step towards the theoretical description of the Standard Model and explained the existence of the weak neutral current, that is mediated by the Z boson and was first observed in 1973 [5, 6] in the Gargamelle bubble chamber at CERN. The unified theory of the electroweak interaction is based on the $SU(2) \times U(1)_Y$ gauge group, that combines the group structures of Quantum Electrodynamics (QED), the quantum field theory describing the electromagnetic interaction, and the weak interaction. The weak charged currents can be described on the basis of the $SU(2)$ symmetry group that gives rise to three gauge bosons $W^{(i)}$ with $i = 1, 2, 3$. The two physical W^\pm bosons, that mediate the weak charged current, are superpositions of two of the $SU(2)$ gauge bosons, given by:

$$W^\pm = \frac{1}{\sqrt{2}}(W^{(1)} \mp iW^{(2)}). \quad (2.1)$$

The third, neutral gauge boson under $SU(2)$ is left without a physical counterpart which implies that the weak interaction can not be fully described by a quantum field theory based on this symmetry group. This problem can be overcome by additionally taking the $U(1)_Y$ gauge symmetry into account, that retains the group structure of QED but interchanges the electric charge with the weak hypercharge Y . A fourth gauge field, B from $U(1)_Y$, is thereby added to the combined symmetry group. The local gauge symmetry under $SU(2) \times U(1)_Y$ gives rise to the two charged W bosons of the weak interaction through equation 2.1 as well as the two neutral bosons of the unified theory, that are the Z boson of the weak force as well as the photon, the exchange boson of the

electromagnetic interaction, through the superpositions given by:

$$\begin{pmatrix} Z \\ \gamma \end{pmatrix} = \begin{pmatrix} \cos \theta_w & -\sin \theta_w \\ \sin \theta_w & \cos \theta_w \end{pmatrix} \begin{pmatrix} W^{(3)} \\ B \end{pmatrix}. \quad (2.2)$$

The angle θ_w is called the weak mixing angle and has to be determined from measurements. Interestingly, at low energies the weak interaction is additionally suppressed due to the high mass of the exchange bosons that enters the propagator. At higher energies, when the weak and electromagnetic force can be unified, the suppression due to the propagator is negligible and both forces are comparable in strength.

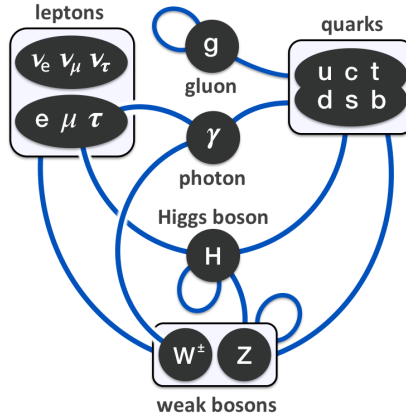


Figure 2.1.: Schematic of the fundamental particles and gauge bosons in the Standard Model. The blue lines indicate the possible interactions. [7]

Our current understanding of particle physics is summarized in the Standard Model, that incorporates the theory describing the interactions and their corresponding exchange bosons as well as the constituents of matter. The theory describing the interactions through the aforementioned three fundamental forces is a combination of the EWT and the quantum field theory describing the strong interaction, Quantum Chromodynamics (QCD). QCD, which will be described in more detail in section 2.1, is based on the $SU(3)$ gauge group that provides eight exchange bosons that are called gluons and interact only with particles carrying color charge, i.e. quarks and themselves. The full symmetry group of the Standard Model is $U(1)_Y \times SU(2) \times SU(3)$, including the gauge group of QCD. Figure 2.1 shows the fundamental particles and exchange bosons that are included in the model as well as their possible interactions which are depicted as lines connecting the different components. The fermions, leptons and quarks, are each organized into three generations of increasing mass and differing by one unit of electrical charge within the generation, for example the leptons e^- and ν_e or the up and down type quarks. Furthermore, the figure depicts an interesting difference between the electromagnetic force and the weak and strong forces. While the exchange bosons from the weak and strong force can interact with themselves, the same is not possible for the photon. As a consequence, the electromagnetic force has an indefinite range while the other two are more strongly confined in their reach.

The last missing part to the Standard Model is the Higgs mechanism that gives rise to the masses of the gauge bosons of the weak interaction, namely the W^\pm and Z , as well as the fermions. Assuming only the $SU(2) \times U(1)_Y$ gauge symmetry, the corresponding bosons should be massless, but the Higgs mechanism spontaneously breaks the electroweak symmetry to a $U(1)_{\text{em}}$ gauge symmetry. In contrast to the symmetry under weak hypercharge of the electroweak model, the new symmetry concerns only the electromagnetic interaction, preserving the vanishing mass of the photon while ensuring the generation of masses for the weak bosons through partial absorption of the Higgs field. This spontaneous breaking of the electroweak symmetry is only possible due to a very particular feature of the Higgs field, namely a non-zero vacuum expectation value. In contrast to the weak bosons that acquire their mass directly in the breaking of the electroweak symmetry, fermions obtain mass by their Yukawa coupling to the Higgs boson. The Higgs boson is the excitation of the Higgs field and was first observed by the ATLAS [8] and CMS [9] collaborations at the CERN LHC in 2012. Following this discovery, the Nobel Prize in Physics in 2013 was awarded to Francois Englert and Peter W. Higgs for the theoretical description of the mechanism that was confirmed by the discovery of the predicted particle.

2.1. Quantum Chromodynamics

The strong force, which is responsible for the existence of hadronic matter like protons and neutrons, is described by a non-abelian quantum field theory called quantum chromodynamics with the gauge group $SU(3)$. In QCD, the quantum number analog to charge in QED is called color charge and, due to the number of degrees of freedom in $SU(3)$, can take one of three values: red, blue and green. The local gauge symmetry gives rise to eight gauge bosons, called gluons, that also carry color charge, unlike the photons in QED. This particular feature of the strong interaction, that is encoded in the theory by being non-abelian, causes the gluons to interact not only with quarks but also with each other. The gauge invariant Lagrangian of QCD can be written as

$$\mathcal{L} = \bar{\psi} [i(\gamma^\mu D_\mu) - m] \psi - \frac{1}{4} G_{\mu\nu}^a G^{\mu\nu a}, \quad (2.3)$$

where D_μ is the covariant derivative that encodes the gauge invariance under $SU(3)$ that gives rise to the quark-gluon vertices. The gluon field strength tensor $G_{\mu\nu}^a$ describes the gluon fields and contains, in contrast to the QED analog, an additional term from pure gluon vertices. This is attributed to the theory being non-abelian and allows for three- and four-gluon vertices. The coupling between quarks and gluons is determined by the strong coupling constant g_s that enters the quark-gluon vertices in the covariant derivative.

The value of the coupling strength g_s depends on the energy scale of the interaction, or in a slightly different wording, on the momentum transfer Q^2 that is conveyed by the gluon. Figure 2.2 shows the energy dependence, also called running of the strong coupling, of measurements of $\alpha_s = g_s/4\pi$ together with the scale dependence of $\alpha_s(M_Z)$ using a two-loop solution of the renormalization group equation [10]. From renormalization of the gluon propagator, the dependence of α_s on the energy scale can be expressed

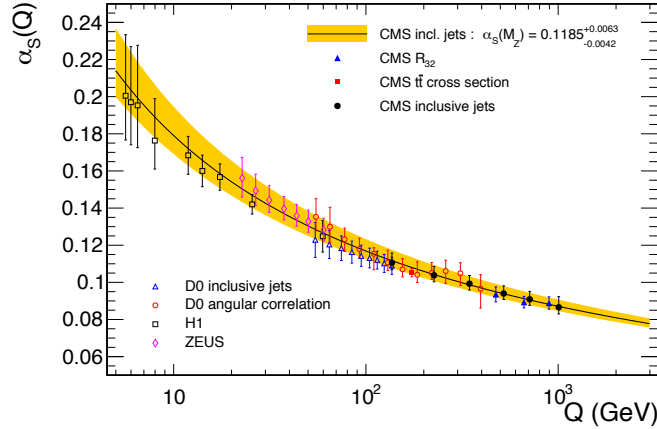


Figure 2.2.: Experimental results for α_S and momentum scale dependence of $\alpha_S(M_Z)$ from renormalization. [10]

in terms of the momentum scale μ as:

$$\alpha_s(Q^2) = \frac{\alpha_s(\mu^2)}{1 + B\alpha_s(\mu^2) \ln\left(\frac{Q^2}{\mu^2}\right)}, \quad (2.4)$$

$$\text{where } B = \frac{11N_c - 2N_f}{12\pi}. \quad (2.5)$$

The contribution from quark and gluon loops in the propagator enters B with opposite sign, where N_f and N_c are the number of available quark flavors and colors. Therefore we observe a decrease of α_s with increasing Q^2 for $N_c = 3$ colors and $N_f \leq 6$ quark flavors. This is in contrast to the scale dependency of the electromagnetic coupling which increases with increasing energy scale of the interaction. Although the dependence of the strong coupling on the energy scale can be described with the renormalization group equation, the absolute value can not be predicted and therefore the reference $\alpha_s(\mu^2)$ has to be provided from a measurement.

The running of the coupling constant with a very large value of $\alpha_s \sim O(1)$ at low momentum transfers and the existence of pure gluon vertices have several implications on the nature of the strong interaction as well as the theoretical treatment.

Due the smallness of the electromagnetic coupling constant ($\alpha \sim \frac{1}{137}$) the sum of loop contributions to a QED interaction converges rather fast and perturbative calculations are sufficient up to very large energies. This is not the case for QCD and possible theoretical approaches for the calculation of strong interactions are effectively split into two realms according to the energy scale of the process. At large values of momentum transfer, or small distances between two interacting quarks, the decrease of the running coupling restores the applicability of perturbation theory. This approach is called perturbative QCD (pQCD). At larger distances, i.e. small energies, perturbation theory breaks down. However, calculations can be performed on a discretized lattice of space-time points. This approach, appropriately named lattice QCD, is computationally very intensive.

Although the existence of quarks is an experimentally well established fact, free quarks have never been observed but are (despite in very extreme conditions) always bound into colorless hadrons. These observations are described by a hypothesis known as confinement which specifies that states of non-vanishing color charge can not propagate as free particles. While not yet analytically proven [11], this hypothesis can be qualitatively understood from the self-interaction of gluons. Two quarks at a certain distance are interacting through the exchange of (virtual) gluons which, due to the fact that they also carry color charge, are in turn interacting with themselves. The result of these attractive interactions is that the color field connecting the two quarks is compressed into a tube rather than spreading out in all directions like it's the case for QED. Exceeding a certain distance, the energy density in this tube is constant which leads to a proportionality between the separation of the two quarks and the energy that is stored inside the color field [11]. The potential can therefore be phenomenologically written as:

$$V(r) \sim \kappa r. \quad (2.6)$$

Because of the linear increase in energy with the distance it would require an infinite amount of energy to disconnect the two quarks. Moreover, when two quarks are flying apart, the energy stored in the color field connecting them will at some point be sufficient to produce a new quark-antiquark pair coupling to the initial quarks. This will continue until eventually there is no energy left to separate any pair and all quarks will be confined in colorless objects, a process referred to as hadronization.

The opposite effect can be observed when quarks are packed very densely. The short distances correspond to very large transfers of momentum between the quarks which lead to a strongly decreased coupling constant according to the scale dependence shown in equation 2.5. The coupling strength approaches zero in the limit of $Q^2 \rightarrow \infty$, a phenomenon that is called asymptotic freedom and has been proven valid by many measurements [12]. But although the quarks are moving in a quasi-free manner, they are still subject to the strong force which requires the consideration of loop corrections to the diagrams when calculating the interactions. In 2004, the Nobel Prize in Physics was awarded to David J. Gross [13, 14], H. David Politzer [15] and Frank Wilczek [13, 14] for the discovery of asymptotic freedom.

2.2. The Quark Gluon Plasma

The asymptotic freedom of quarks at high energy scales has the consequence, that hadronic matter dissolves into a strongly coupled soup of quasi-free quarks and gluons at very high temperatures. This state of deconfined matter is called Quark Gluon Plasma (QGP) and it is believed that the early universe passed through this phase in its evolution very shortly after the Big Bang. Already as early as 1965, Hagedorn proposed a maximum temperature for the existence of hadronic matter [16]. The model is based on a self-similarity of the fireball produced in hadronic collisions and describes the resonance spectrum, which was experimentally found to rise exponentially, as a density of self-similar resonances. Assuming that the fireballs can be described using statistical thermodynamics, the numerical calculations yielded a maximum temperature

of 150 MeV [16] for hadronic matter.

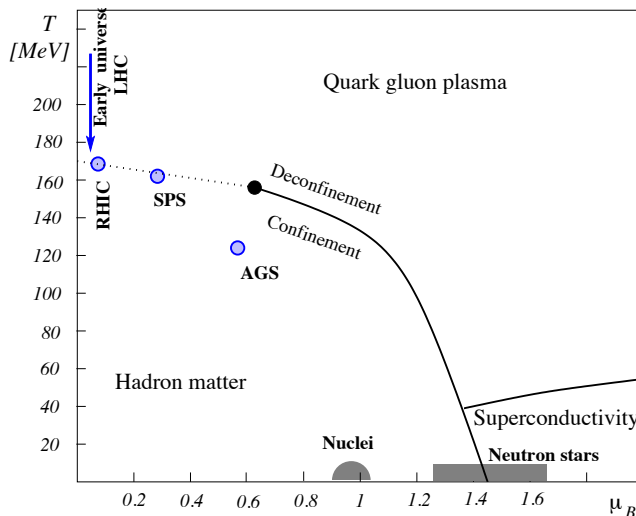


Figure 2.3.: The QCD phase diagram in the $\mu_B - T$ plane, showing the different phases including the assumed phase of color superconductivity at large baryon chemical potentials and low temperatures. The solid line separating the confined and deconfined phase depicts a first order phase transition, adjoining the cross over region that is shown as a dashed line in the critical point. [17]

More recent calculations of the transition temperature T_c , at which the phase transition from hadronic matter to the deconfined phase occurs, were done using lattice QCD. Lattice QCD allows for the calculation of strong interactions at low momentum transfers but is limited to vanishing baryon chemical potentials μ_B . The baryon chemical potential is a measure for the net baryon density, indicating the imbalance between matter and antimatter. Figure 2.3 shows the different QCD phases in dependence of the baryon chemical potential and the temperature. The early universe is expected to sit at low values of μ_B , close to where lattice QCD is applicable, which is also the region that is probed by heavy ion collisions at RHIC and the LHC. At low baryon chemical potentials, calculations rather suggest a crossover behavior than a phase transition [18]. This is depicted by the dashed phase boundary in figure 2.3. The crossover likely turns into a first order phase transition at higher values of μ_B , with a critical point separating the two regimes [18, 19]. Going to very high net baryon densities, the transition temperature approaches zero and an additional phase is expected, that is distinguished by color superconductivity with quarks forming Cooper pairs. Transition temperatures of $T_c \sim 150 - 170$ MeV were calculated by several groups with the use of lattice QCD at $\mu_B \sim 0$ [20, 21].

In the transition from hadronic matter to the deconfined phase, hadrons are dissolving into quarks and gluons which increases the number of degrees of freedom of the system. This can be seen in the steep rise in the energy density (in units of T^4) calculated using lattice QCD at the transition temperature in figure 2.4. After the steep rise the energy density flattens out which can be attributed to a further heating of the

system without additional degrees of freedom being liberated. The energy density is calculated for $n_f = 2 + 1$ quark flavors with physical masses, corresponding to the two light (up and down) and one heavier (strange) quark, on three different lattice spacings. The characteristic temperature of the crossover transition to the deconfined state was determined to $T_c = 152 \pm 4$ MeV [22]. Figure 2.4 also indicates the Stefan-Boltzmann limit at $T \rightarrow \infty$ where the formerly strongly coupled system approaches a state that can be described as an ideal gas due to asymptotic freedom.

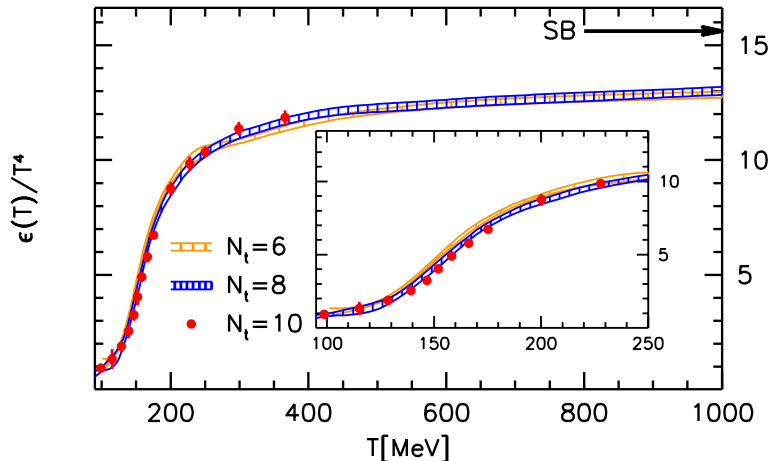


Figure 2.4.: Energy density in units of T^4 calculated with lattice QCD on three different lattice spacings $N_t = 6, 8$ and 10 . [22]

It is crucial for the production of the QGP in the laboratory, that the system can reach a state of (local) thermal equilibrium such that thermodynamic quantities like temperature, pressure or energy density are defined. The collision of heavy nuclei instead of hadrons ensures a high multiplicity of particles being produced. This is essential to the formation of a strongly coupled system because of the need for a high probability of interactions between the emerging particles. Given the initial collision produces a high number of particles in a very confined region of space, these particles are more likely to interact and drive the system towards an equilibrated state rather than leaving the initial collision individually. Furthermore the lifetime of the system must be large enough for it to reach local equilibrium [19].

The evolution of the fireball, that is produced in a heavy ion collision and forms a QGP, can be separated in several steps, starting with the pre-equilibrium phase that is dominated by hard processes like the production of jets or prompt photons (see section 2.3). After the system reaches local equilibrium and its temperature exceeds T_c , the plasma is formed. The probes that originated earlier are now modified and the production of particles is dominated by soft processes. Then the system expands further and cools down, when the temperature drops below the critical value the quarks will recombine into hadrons. This phase is called chemical freeze-out with the system being transformed into a hadron gas. Hereby, the hadron gas is still in local equilibrium and shows thermodynamic quantities but with the degrees of freedom now being hadrons instead of quarks and gluons. However, the chemical freeze-out is not instantaneous,

thus the QGP and hadron gas phases can overlap for some time. As soon as the system spreads too far for the hadrons to interact with each other, the kinematic quantities are fixed. This last phase of the evolution is called kinetic freeze-out.

There are many different and interesting probes and possible signatures of the plasma, like jet-quenching due to interactions with the medium or a modification of quarkonia production compared to the case where no plasma is formed. But since a detailed description of the full spectrum of different measurements that can shed light on the strongly interacting medium would go beyond the scope of this work, the next section will only focus on photons as a probe in high energy collisions in general and of the quark gluon plasma in particular.

2.3. Photons in High Energy and Heavy Ion Collisions

Photons are a particularly interesting probe in heavy ion collisions. They are created at every stage of the collisions and the evolution of the fireball thereafter and leave the strongly interacting medium mostly unaffected due to the comparably small coupling constant of the electromagnetic interaction. In contrast to hadronic probes, which originate in later stages of the evolution, photons can carry information about the initial collision and the thermalization of the medium outwards to the detectors. The production of photons is modified by the strongly interacting medium at low and intermediate transverse momenta. At high transverse momenta, photons can be used as a test of pQCD calculations of their production processes. This is not restricted to heavy ion collisions but can obviously also be performed in hadronic collisions. The measurements of photons in proton-proton collisions at RHIC and the LHC are very well reproduced by pQCD calculations [23]. Typically, interactions that can be calculated using perturbative techniques are referred to as hard processes due to the large momentum transfers at which they occur. In contrast to hard processes, soft processes occur at low momentum transfers and can be calculated using lattice QCD techniques. The different production mechanisms result in photons at different transverse momenta, with hard and soft processes yielding high and low momentum photons, respectively. Although it is not perfectly clear yet down to which value of transverse momentum pQCD is applicable, the soft and hard scales can be separated at $p_T \sim 1 - 2 \text{ GeV}/c$ where perturbative calculations still agree well with the data [23].

The measurements of the photons described above is an experimental challenge due to the fact that the dominant part of the photon yield does not originate in the soft or hard interactions that one would like to probe but from electromagnetic decays. The majority of decay photons are created in the decays of neutral pions which, being the lightest hadron, exist in large abundancies and decay only electromagnetically. Photons that are not produced in particle decays are usually referred to as direct photons and can be further classified according to their production mechanism. Prompt photons are large momentum direct photons from hard processes like quark-gluon Compton scattering that can also occur in the vacuum. Photons produced as a byproduct in the jet fragmentation of a parton or in parton-medium interactions like quark bremsstrahlung are typically called fragmentation photons and can also be linked to hard interactions. Soft interactions in a thermalized medium like the plasma or a hadron gas will produce

low momentum photons that are commonly named thermal photons although their production is not equivalent to thermal radiation from a black body radiator.

2.3.1. Photons from Hard Processes

Prompt photons with large momenta are produced in hard processes like partonic Compton scattering or quark-antiquark annihilation. The lowest order contributions to these interactions, shown in figure 2.5 (a) and (b), are independent of the fragmentation of the involved partons. Hard photons can also be produced by the fragmentation of a parton, i.e. a quark or a gluon. This can happen via the hadronization into a jet with many final state particles including photons or through bremsstrahlung by quarks if a recoil partner is present. Photons from these production mechanisms were earlier called fragmentation photons and the next-to-leading order diagram of the interaction is shown in figure 2.5 (c). At large transverse momenta, hard photons are by far the dominant source of direct photons, implying that the relevant energy scale of the production process correlates with the momentum of the final state photon. The production cross sections for hard photons can be calculated using pQCD. For proton-proton collisions, the invariant cross section can be written as [23]

$$E \frac{d^3\sigma}{dp^3} = \sum_{a,b,c} f_{p/a}(x_a, Q^2) \times f_{p/b}(x_b, Q^2) \times d\hat{\sigma}(Q^2) \times D_{\gamma/c}(z, Q^2), \quad (2.7)$$

where $f_{i/p}(x_i, Q)$ with $i = a, b$ are the parton distribution functions. These depend on the relevant energy scale of the interaction that is given by the momentum transfer Q^2 and describe the probability to find parton i with momentum fraction x_i inside either of the colliding hadrons. The cross section $d\hat{\sigma}(Q^2)$ of the interaction of the two partons can be evaluated as a perturbative expansion in the QCD coupling for hard processes. Equation 2.7 also includes the parton-to-photon fragmentation function $D_{\gamma/c}(z, Q^2)$, that governs the fragmentation of a scattered parton c to a photon with momentum fraction z . Prompt photons from interactions (a) and (b) in figure 2.5 are already final state objects and do not require the fragmentation function. The energy scale Q^2 coincides with the transverse momentum of the produced photons up to a constant factor. Photons from hard or soft processes can therefore be associated with different regimes in transverse momentum.

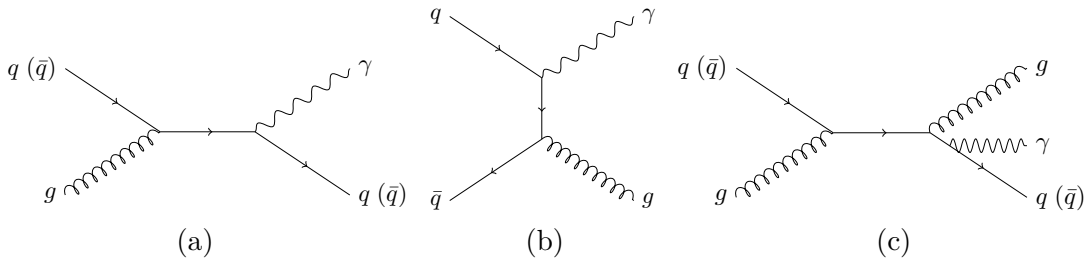


Figure 2.5.: Leading and next-to-leading order diagrams for prompt and fragmentation photon production through (a) quark-gluon Compton scattering, (b) quark-antiquark annihilation, (c) quark fragmentation or bremsstrahlung.

The mean free path for photons in the strongly interacting medium produced in heavy ion collisions is much larger than the size of the fireball [24]. This is due to the much smaller coupling strength of the electromagnetic interaction compared to the strong interaction and ensures that the medium is transparent for photons. Even if produced in the early stages of the collision, they leave the medium mostly unaffected. Nevertheless, the prompt and fragmentation photon production can be modified due to initial and final state effects of the nucleus-nucleus collision. Initial state effects can be understood as modifications of the parton distribution functions in collisions of nuclei compared to single hadrons. Furthermore, effects in the final state of the collisions can modify the photon production if the photon sources lose energy through interactions with the medium. The momentum distribution of the partons is thereby affected by the strongly interacting medium which in turn alters the momentum distribution of fragmentation photons.

2.3.2. Photons from Thermalized Sources

In contrast to prompt or fragmentation photons, the photons from soft processes are an indication of the formation of a strongly interacting medium in heavy ion collisions. Soft photons are produced through the same interactions as hard photons that are shown in figure 2.5 although not in the initial collision but in the interactions of thermalized particles. They are therefore emitted during the QGP phase and the following hot hadron gas phase respectively. Albeit soft photons do not originate from thermal radiation, they are often referred to as thermal photons with regard to the thermalized sources. The spectrum of thermal photons resembles thermal radiation due to the momentum distribution of the sources, which are in thermal equilibrium in the medium.

However, the theoretical treatment of soft processes differs from the hard processes discussed in the previous section. Due to the low momentum transfers in the interactions, the perturbative approach is not applicable anymore. Typical models use a macroscopic description of the system to calculate the production of thermal photons. When the evolution of the system is known, for example from viscous hydrodynamics (see [23]), the thermal photon spectrum can be calculated from the emission rates [25]. The thermal photon yield exhibits a proportional behavior,

$$E \frac{d^3N}{dp^3} \propto \exp\left(-\frac{E}{T}\right), \quad (2.8)$$

where T is the effective temperature of the system and should not be confused with the initial temperature at the formation of the plasma. This is due to the fact that photons are emitted during all stages of the evolution of the fireball and increasingly blue shifted because of the increasing expansion velocity of the medium.

2.3.3. The Direct Photon Signal

The total yield of photons that is produced in collisions of both hadrons and heavy ions, however, is greatly dominated by photons from particle decays. While insights on the underlying physics are gained from the study of the direct photon signal, direct photons and those coming from decays can not be distinguished in the measurements.

This of course is rather an experimental challenge than a theoretical one, but it is worth mentioning the approach here to acquire a better understanding of the structure this thesis is presented in. The use of ratios is always experimentally worthwhile if the numerator and denominator share common sources of systematic uncertainties to (partially) cancel the overall systematic uncertainty of the measurement. Therefore, the excess of direct over decay photons is expressed as the photon double ratio:

$$R_\gamma = \frac{(\gamma_{\text{inc.}}(p_T)/\pi^0(p_T))_{\text{meas.}}}{(\gamma_{\text{dec.}}(p_T)/\pi^0(p_T))_{\text{sim.}}}, \quad (2.9)$$

where $\gamma_{\text{inc.}}(p_T)$, $\gamma_{\text{dec.}}(p_T)$ and $\pi^0(p_T)$ are the inclusive (direct plus decay) photon, the decay photon and the π^0 spectrum respectively. The numerator is obtained from the measurement whereas the decay photons can not be distinguished and must be taken from a decay simulation containing several sources. Due to the reconstruction of the neutral pions from the two photon decay channel, the systematic uncertainties cancel partially in the numerator. The direct photon spectrum is then obtained from the double ratio and the measured inclusive photon spectrum:

$$\gamma_{\text{dir.}}(p_T) = \gamma_{\text{inc.}}(p_T) - \gamma_{\text{dec.}}(p_T) = \gamma_{\text{inc.}}(p_T) \cdot (1 - R_\gamma^{-1}(p_T)). \quad (2.10)$$

The analysis aims for the direct photon spectrum and will therefore cover the different ingredients in order of their appearance in equations 2.9 and 2.10.

Figure 2.6 shows a previous analysis of the direct photon spectrum in lead-lead collisions at center-of-mass energies of $\sqrt{s_{\text{NN}}} = 2.76$ TeV measured by ALICE. The spectra are shown for three different collision centralities and compared to different model calculations. Collision centralities are related to the aforementioned impact parameter, with small centrality percentages (i.e. central collisions) being attributed too small impact parameters and vice versa. The left panel shows the measured spectra compared to full model calculations including pQCD photons by different groups as well as an exponential fit to the low p_T part of the spectrum that illustrates the proportionality stated in equation 2.8. In the right panel, the direct photon spectrum is shown in comparison to pQCD predictions for proton-proton collisions. The predictions are at the same center of mass energy and scaled by the number of binary collisions, assuming no initial and final state effects as well as no contribution from thermal photons. The spectra show an excess above the calculations at low p_T for the two more central classes whereas they coincide with the predictions within the systematic uncertainties at higher p_T . This illustrates that initial and final state effects hardly modify the direct photon spectrum. The model predictions seem to be in good agreement with the measured direct photon spectra, also at low transverse momenta where a substantial contribution of photons from soft processes is observed.

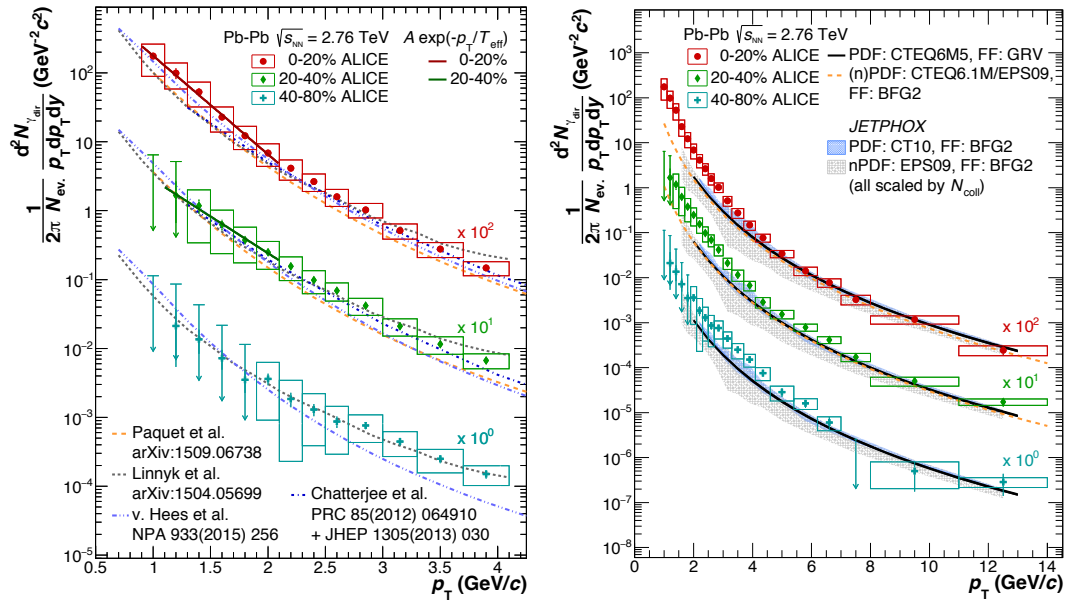


Figure 2.6.: Direct photon spectra in Pb-Pb collisions at $\sqrt{s_{NN}} = 2.76$ TeV measured by ALICE compared to model calculations including pQCD photons (left) and NLO pQCD predictions for pp collisions at the same energy scaled by the number of binary collisions (right). [26]

3. The Experimental Setup

The Large Hadron Collider (LHC) as well as the ALICE detector systems are introduced in this chapter. First, the LHC will be described briefly with the main focus on the specifics of the proton-proton running. Followed by the detector description, focused on the sub-detectors relevant to the photon measurement. The description of their working principles is concluded with a brief overview over the combination of the different sub-detectors in the tracking system. Finally, the software framework that is used for the analysis is described briefly.

3.1. The Large Hadron Collider

The European Organization for Nuclear Research (CERN) at Geneva, Switzerland, is the host of the world's largest particle collider, the Large Hadron Collider (LHC). As the name suggests, the LHC is designed to collide hadrons, namely protons, but lead ions are also utilized in the heavy ion program. Rather than being a perfect circle, the LHC is divided into eight arcs containing the dipole bending magnets that keep the circulating hadrons in their orbit and eight intersections whose layouts depend on the specific use. The different intersections are for example designed for the injection and acceleration of the beam or the beam collisions within the detectors in the four experiment caverns that house the detectors of ALICE, ATLAS, CMS and LHCb. Furthermore, there are three smaller experiments exploiting collisions in the LHC: TOTEM, LHCf and MoEDAL. Situated in a tunnel of approximately 27 km circumference that previously housed the Large Electron Positron Collider (LEP), the LHC is the last stage of a series of accelerators that is shown in figure 3.1.

The acceleration begins with a hydrogen bottle that provides protons after the electrons are stripped from the atoms using an electric field. The protons then encounter the first accelerator, LINAC 2, which brings them to an energy of 50 MeV. As sketched in figure 3.1, following the LINAC 2, the proton beam is injected into the Proton Synchrotron Booster (PSB) that increases the energy to 1.4 GeV and is succeeded by the Proton Synchrotron (PS) that raises the energy of the beam to 25 GeV. The last accelerator before the LHC, the Super Proton Synchrotron (SPS), finally pushes the proton beam to its injection energy of 450 GeV [27]. In the LHC, the beams are further accelerated to the record energy of 6.5 TeV per beam, with a maximum possible beam energy of 7 TeV. In addition, most of the accelerators in the chain also have their own experimental halls with experiments designed for lower beam energies.

For completeness it should be noted that the acceleration chain for heavy ions slightly differs from the one for protons due to the more complex procedure required to obtain the desired ionization state.

The LHC is designed to deliver peak luminosities of $\mathcal{L} = 10^{34} \text{ cm}^{-2}\text{s}^{-1}$ and $\mathcal{L} = 10^{27} \text{ cm}^{-2}\text{s}^{-1}$ for proton-proton and lead-lead collisions, respectively [28]. The lumi-

osity is proportional to the number of events per seconds and is therefore a measure for the amount of data recorded and the level of statistics that can be achieved. The proton beams are separated in several bunches, consisting of $1.15 \cdot 10^{11}$ protons each, with a nominal spacing of 25 ns in between and a maximum total number of 2808 bunches. [29].

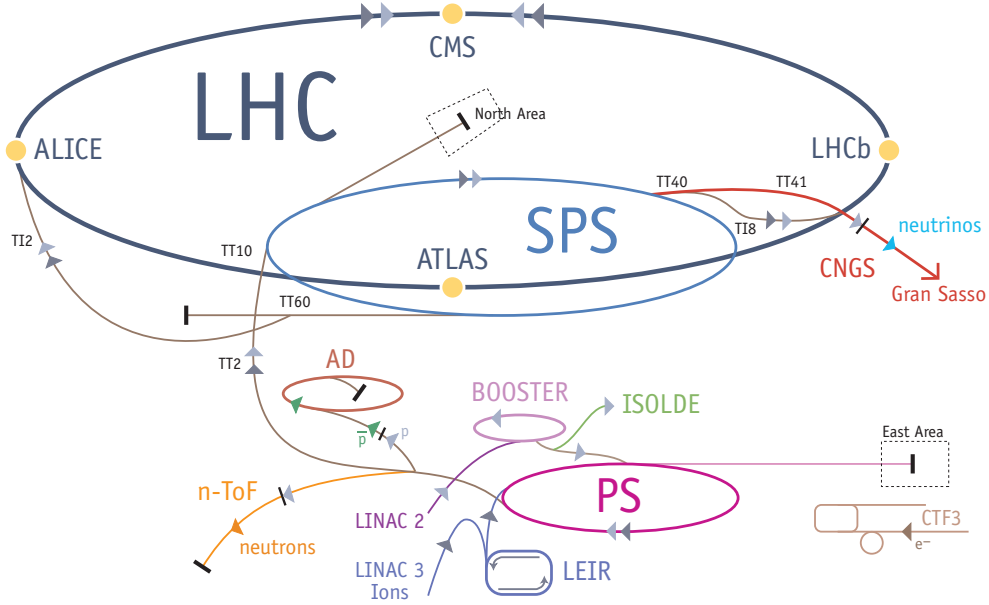


Figure 3.1.: Sketch of the layout of the CERN accelerator complex. [30]

3.2. A Large Ion Collider Experiment (ALICE)

ALICE is the designated experiment to study the extreme states of matter created in heavy-ion collisions at the LHC. In order to be able to disentangle signals from different phases of the evolution of the fireball, the detector needs optimal particle identification (PID) capabilities. Furthermore, a high momentum resolution especially for low p_T tracking is of crucial importance to allow for a precise measurement of the soft particles produced by the thermalized source.

The ALICE detector, shown in figure 3.2, consists of the central barrel inside the solenoid L3 magnet and the independent muon arm in forward direction, which is not used in the analysis presented in this thesis and therefore not covered. The solenoid magnet was built for the L3 experiment at LEP and can provide a magnetic field of up to 0.5 T that is aligned with the beam pipe. Particle identification and tracking at mid rapidity is provided by the central barrel which is divided in many different subsystems. Particles that are created in collisions at the interaction point and will first encounter the Inner Tracking System (ITS), which is situated at small radii around the beam pipe. Then the particles enter the Time Projection Chamber (TPC), a large ionization chamber, followed by the Transition Radiation Detector (TRD) and the Time-of-Flight

(TOF) system. Depending on the polar and azimuthal angle, the particles may encounter one of the three calorimeters, the Electromagnetic Calorimeter (EMCal), the Di-Jet Calorimeter (DCal) or the Photon Spectrometer (PHOS), which cover different regions of the solid angle.

In the following sections, all relevant sub-detectors for the measurement presented in this thesis will be described in more detail.

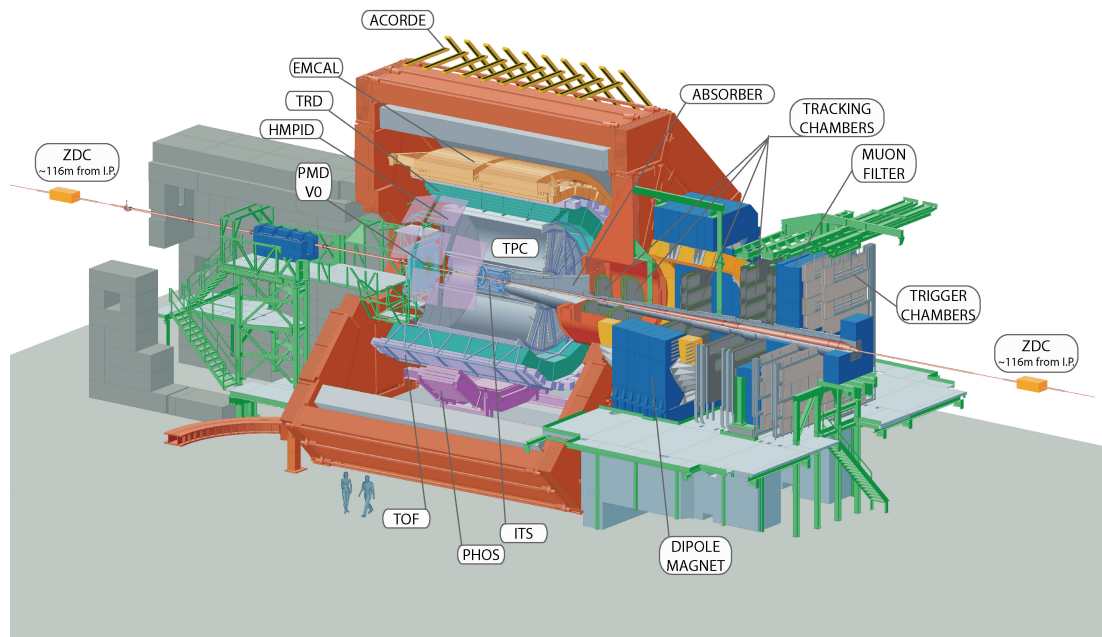


Figure 3.2.: Overview of the ALICE detector and the subsystems. The L3 magnet can be seen in red, enclosing the central barrel detectors. [31]

3.2.1. Forward Detectors

The V0 detector [32] is used as a Minimum Bias (MB) trigger as well as a fast multiplicity counter to estimate the collision centrality in proton-lead and lead-lead events. The detector consists of two scintillator arrays, V0A and V0C, located at $z = 340$ cm and $z = 90$ cm, respectively, on both sides of the interaction point with the distances dictated by other central barrel detectors. The two parts of the V0 detector cover the pseudorapidity ranges of $2.8 < \eta < 5.1$ (V0A) and $-3.7 < \eta < -1.7$ (V0C).

3.2.2. T0 Detector

The T0 detector [32] provides the earliest trigger signal and therewith the start time for the TOF detector. Furthermore, it measures the position of the collision vertex and can discriminate against beam-gas interactions. It consists of two arrays of 12 Cherenkov counters each, that are based on photomultiplier tubes. The two parts of the detector,

called T0-A and T0-C, are situated at a distance of 375 cm and 72.7 cm to the nominal vertex and cover a pseudorapidity range of $4.61 \leq \eta \leq 4.92$ and $-3.28 \leq \eta \leq -2.97$, respectively.

3.2.3. Inner Tracking System

The detector closest to the collision point is the Inner Tracking System (ITS) [32], a cylindrical silicon detector directly encircling the beam pipe. Making use of three different pad designs, the system consists of six layers with two neighboring layers sharing the same technology. The innermost two layers are Silicon Pixel Detectors (SPD) which have the highest granularity and spatial resolution in z -direction of the system. This provides a good primary vertex resolution and secondary vertex separation in the highest track density environment close to the interaction point. Following are two layers of Silicon Drift Detectors (SDD) and the two outermost layers which are Silicon Strip Detectors (SSD).

The whole system is designed to have a small X/X_0 reduce the number of photon conversions in the material, which is achieved by using a lightweight carbon-fibre support structure. Furthermore, it needs to be able to handle charged particle multiplicities of up to $dN_{\text{ch}}/dy \approx 8000$. The detector has a spatial coverage of 2π in azimuthal direction and $|\eta| < 0.9$ in pseudorapidity for all vertices. Primary vertices are measured with a resolution better than $100 \mu\text{m}$ and the relative momentum resolution for pions with $p_{\text{T}} = 0.1 - 3 \text{ GeV}/c$ is better than 2%.

It is possible, that several collisions happen during one bunch-crossing. This leads to an overlap of events in the detector with different tracks belonging to different collision vertices. Due to the good vertex resolution of the SPD, these so called pileup events can be rejected. If this would not be the case, tracks would be attributed to the current event although not belonging to primary vertex that has been selected.

Additionally to the tracking, the four outermost layers can be used for particle identification via a measurement of the specific energy loss per unit length (dE/dx) in the non-relativistic region (low p_{T}) due to their analogue readout. The particle identification capabilities of the ITS are worse than those of the TPC due to the worse resolution in the specific energy loss measurement.

3.2.4. Time Projection Chamber

The Time Projection Chamber (TPC) [32, 33], shown schematically in figure 3.3, is a cylindrical drift chamber surrounding the ITS and is the largest tracking and PID device within ALICE. The detector covers the full range of 2π in azimuth and $|\eta| < 0.9$ in pseudorapidity and is designed to be able to reconstruct a maximum number of charged particles per unit rapidity of $dN_{\text{ch}}/dy \approx 8000$ which translates to about 20000 charged tracks in the TPC acceptance.

The drift gas of the TPC is confined inside the cylindrical field cage with the drift volume being divided by the central electrode at $\eta = 0$ and $z = 0$. Following the electric field, charges freed by the ionization of the gas are read out in the read-out chambers at the end plates of the barrel on both sides. The drift gas was a mixture of 85.7% Ne,

9.5% CO₂ and 4.8% N₂ that was used until the end of 2010. The nitrogen was removed for further data taking, leaving a mixture of 90% Ne and 10% CO₂.

A high voltage of 100 kV is applied at the central electrode and the voltage gradient in the field cage towards the readout chambers is 400 V/cm which translates to a maximum drift time of 92 μ s for electrons from the ionization of the gas. The tracks of charged particles traversing the TPC are reconstructed in three dimensions combining the hit positions of the ionized charges on the end plates and the drift times with the starting time given by the T0 detector. The maximum luminosity that can be processed by the ALICE detector's central tracking system is limited by the readout time of the TPC. Proton-proton collisions with a luminosity and an interaction rate of $\mathcal{L} = 5 \cdot 10^{30} \text{ cm}^{-2}\text{s}^{-1}$ and 350 kHz, respectively, will result in tracks of about 60 proton-proton events being stored in the drift volume at the same time. The current (triggered) event is thereby overlapping with several past and future events, an effect that is called pileup. Due to the much faster read-out time of the ITS, only the triggered event is stored and some of the tracks from past and future events can be rejected by track matching between the TPC and ITS. This, however, only works for tracks with ITS information and not for those that are only measured in the TPC, like electrons from photon conversions at the inner shield of the TPC, for example. In that case, other techniques (presented in section 5.3.1) have to be used to correct for the contribution from overlapping events.

The transverse momentum of reconstructed tracks is calculated from the curvature in the transverse plane with the tracking algorithm limiting the measurement to a minimum of 50 MeV/ c for secondary tracks, i.e. tracks that do not originate from the primary vertex. Primary tracks can be measured in the transverse momentum range of 100 MeV/ c to 100 GeV/ c with the lower limit again given by the strong curvature of the track in the magnetic field. Low momentum tracks are bent so strongly, that they do not traverse the minimum length of 1/3 of the radial range of the TPC that is required for the tracking.

In addition to being the main tracking tool of the central barrel, the TPC is also the main particle identification system for charged particles. The specific ionization energy loss in the drift gas of the TPC can be used to identify charged particles, given the momentum of the track and using the description of the energy loss. The specific energy loss can be described by the Bethe-Bloch formula that relates the mean energy loss of a certain particle to its $\beta\gamma$.

3.2.5. Electromagnetic Calorimeter

The Electromagnetic Calorimeter (EMCal) [32, 34] is one of the calorimeters installed at ALICE. The calorimeter is designed as a lead-scintillator in sampling architecture, segmented into 12288 towers. The towers are grouped into 12 supermodules, six of which are in azimuthal direction for $\eta < 0$ and the same structure is mirrored for $\eta > 0$ with the separation in the center at $\eta = 0$. 10 of the supermodules are 'full size', spanning $\Delta\eta = 0.7$ and $\Delta\phi = 20^\circ$, while the remaining two supermodules are 'one-third size' with a coverage of $\Delta\eta = 0.7$ and $\Delta\phi = 7^\circ$. The full detector therefore has a geometrical acceptance of $|\eta| < 0.7$ and $\Delta\phi = 107^\circ$. While PHOS, due to its higher granularity and non-sampling architecture, delivers a better position and energy

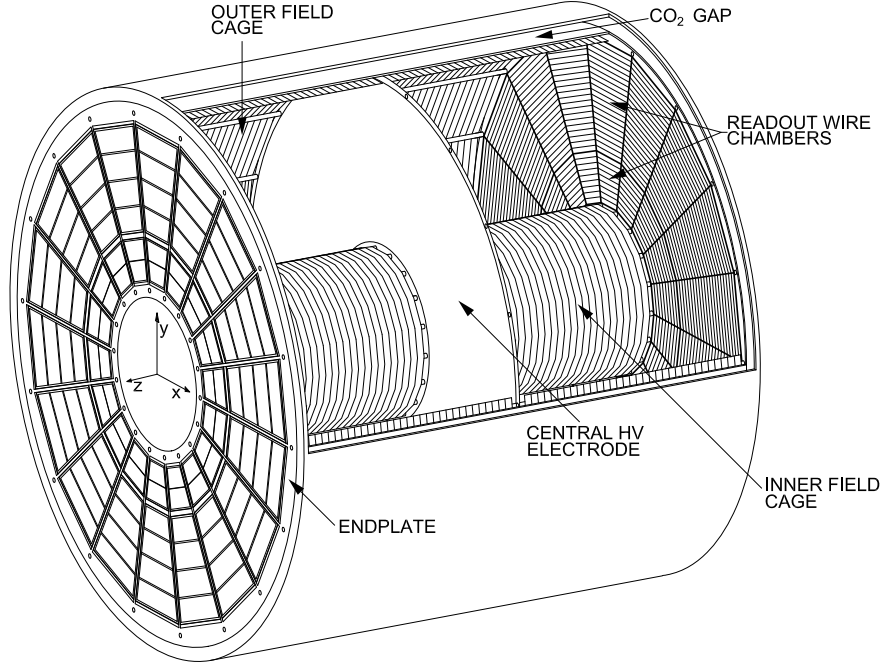


Figure 3.3.: Schematic of the ALICE TPC. [33]

resolution especially at lower p_T , the EMCal has the advantage of a larger acceptance. The overall material budget of the calorimeter is about 20 radiation lengths.

3.2.6. Charged Particle Tracking in the Central Barrel

The event reconstruction in the ALICE central barrel starts with the determination of the primary vertex using the two innermost layers of the ITS that provide the highest granularity. The identification of the primary vertex is first done preliminary and later optimized when the full information of the tracks pointing towards the primary vertex is available. A linear extrapolation of pairs of hits in the two SPD layers of the ITS is used to determine the z position of the preliminary vertex at $x = 0 = y$. The same algorithm is then used in the transverse plane, but with a worse resolution due to the bending of the tracks in the magnetic field.

After the preliminary vertex is identified, the tracking procedure starts with the track segments inside the TPC. The measured clusters, a set of ionization signals in all three dimensions, are combined using a Kalman filter algorithm to reconstruct the track inside the TPC. This is done starting at the end of the TPC and going inwards, once with the constraint that the track points to the primary vertex and once without. In both cases the results are stored and the tracks are propagated to the outermost layer of the ITS. The track finding procedure is reproduced in the ITS with the TPC tracks used as seeds and going inwards. If space points from the ITS can not be unambiguously assigned to the TPC track, all possibilities are calculated and the most probable track is used. Hereby, again the two sets of parameters are stored.

Then, the tracks from the combination of the TPC and ITS are used as seeds and

the Kalman filter approach is reversed, starting at the innermost layer of the ITS. The track parameters are optimized by removing fake hits in the ITS or clusters in the TPC. Instead of stopping at the outer shield of the TPC, the tracks are extrapolated further to the TRD where the information from the TRD layers are added to the track if available.

The last step of the tracking is a refitting of the reconstructed tracks inwards, which again is done with and without the assumption of the track pointing to the primary vertex. The final tracks are then stored for both cases.

The final primary vertex can then be found using the final tracking information. Like for the preliminary vertexing, each track in the ITS and now also in the TPC is fitted with a straight line constrained by the position of the preliminary primary vertex. The final primary vertex is found by minimizing the distances of closest approach for track pairs using a χ^2 method. It is possible that more than one primary vertex is found due to pileup events which further complicates the procedure.

3.3. The Analysis Framework

The large amounts of data accumulated by big experiments like ALICE require specialized software packages to deal with them. These packages are used to process the raw data from the detector, produce the simulations of events that are needed to correct for detector effects and eventually combine everything in a meaningful, physical manner.

In ALICE, the whole framework is separated in two packages: AliRoot [35] and AliPhysics [36], which are both based on ROOT [37], an object-oriented programming toolset for physics analysis that was developed at CERN and is continuously improved and maintained. Like ROOT, also AliPhysics and AliRoot are continuously being further developed and improved to adapt to the ever changing challenges in the data analysis and achieve a better performance.

The processing of the raw data is taken care of by the AliRoot package, which covers features like the detector data reconstruction and the production of Monte Carlo (MC) simulations of events using integrated generators like PYTHIA [38, 39] and particle interaction simulations to transport the generated particles through the detector like GEANT [40, 41, 42]. The different software tools used for the different physics analyses of the data are collected in the AliPhysics package. Besides the analysis of the detector data, also MC events are analyzed with the software in the AliPhysics package, eventually combining the measured and simulated samples to gain insight into the physical quantities not convoluted with the detector response.

4. Data Samples and Monte Carlo Simulations

The analyzed data sets and corresponding Monte Carlo (MC) simulations are presented in this chapter. The data sets consist of proton-proton collision events at center-of-mass energies of $\sqrt{s} = 7$ TeV, recorded with the ALICE detector in 2010. In order to be able to correct the data for detector effects like the reconstruction efficiency, MC events are produced with a subsequent simulation of the detector response.

First, the analyzed data samples are presented, followed by a description of the simulations used for the corrections of the measured raw spectra. The quality assurance of the data and MC samples is described in the section following thereafter. The chapter is closed with a section on the selection of the events that have been analyzed.

4.1. Analyzed Data Samples

The analyzed data set of proton-proton collisions is separated in five periods: LHC10b, LHC10c, LHC10d, LHC10e and LHC10f. These periods are subdivided into runs which correspond to one continuous time of data taking of the detector. MC event simulations have to be anchored specifically to the runs due to possible different running conditions and detector settings. The data was taken with a comparably low interaction rate of a few to a few tens of kHz [43], resulting in a small contribution of out-of-bunch pileup as can be seen in section 5.3.1.

A minimum bias event, corresponding to the exclusion of rare triggers, e.g. triggers on high multiplicity events, is accepted if the minimum bias trigger, MB_{OR} , conditions are fulfilled. The trigger accepts an event if a hit in one of the V0 detectors or the first two layers of the ITS is detected.

The two reconstruction methods that are used, have different requirements on the data which is reflected in the quality assurance and therefore the number of events that are analyzed. Table 4.1 summarizes the numbers of events for the different periods and reconstruction methods that are obtained after the quality assurance and event selection presented in sections 4.3 and 4.4, respectively. The total number of events that is ultimately used for the analysis is also quoted and labelled LHC10[b-f], representing the sum of all periods. It can be seen that the data set that is obtained for the analysis with the calorimeter amounts to about 70% of the statistics available for the conversion measurement. This is due to specific problems with several runs concerning the reconstruction with the calorimeter.

4.2. Event Generators and Monte Carlo Simulations

The corrections that are applied on the raw measured particle spectra rely on Monte Carlo event simulations and the subsequent transport through a simulation of the detector. The event generator used for the analyzed collision system and energy is PYTHIA 6.4 [38], which is inspired by pQCD. Nearly all leading order $1 \rightarrow 2$ and $2 \rightarrow 2$ processes as well as selected $2 \rightarrow 3$ processes are included in PYTHIA. Parton showering, i.e. initial- and final-state radiation, and the hadronization of partons via the Lund fragmentation model are also implemented in the simulations. The generator is tuned to LHC energies.

The implementation of the detector and the transport of the particles through the simulated detector is done using GEANT3 [40]. It uses a simulated replica of the ALICE detector that is tuned to represent the state of the detector in the specific runs. All particles that are transported through the detector interact with the detector material through all known material interactions and the response of the detector is simulated. Therefore, the simulated events can be reconstructed like data while still holding all MC information. This enables the use of the simulated events to correct the data.

The MC periods, that are anchored to and used alongside the data, are: LHC14j4b, LHC14j4c, LHC14j4d, LHC14j4e and LHC14j4f. While the recorded collisions have to pass certain event selection criteria, the MC events are specifically generated to reproduce minimum bias events. Thus, the selection of events in the simulations is only subject to a very reduced set of criteria. However, the generated events that are grouped into runs have to be crosschecked with the data in order to ensure the coincidence between data and MC. This is covered by the quality assurance where 'bad' runs are discarded. Hence, the same runs that are rejected in data are also rejected in MC and vice versa. The numbers of events for both reconstruction methods that are obtained are summarized in table 4.1. Again, a smaller number of events is available for the calorimeter measurements. It can also be seen, that the numbers of events in data and MC agree very well for the respective methods.

4.3. Quality Assurance

Quality assurance (QA), in this context, is the examination of coincidences of relevant quantities between MC and data. These checks have to be performed runwise since the detector should be running stable during one run with settings possibly differing between the runs. The MC is also produced runwise and anchored to the specific run in data to reproduce the measured spectra as well as the detector conditions. Additionally, this has to be done separately for the two reconstruction methods presented due to the different requirements. The conversion method, for example, is not sensitive to hot calorimeter cells that have to be considered in the calorimeter analysis.

During the QA, runs are excluded if they show problems due to the running condition or if they do not match with the corresponding simulations in critical quantities like the number of photon candidates in the case of the conversion method or clusters in the case of the calorimeter measurement. Another reliable quantity that is compared is the mass position of the neutral pion peak, integrated over p_T , that should be consistent

period	conversion method N_{events}	calorimeter method N_{events}
Data		
LHC10b	2.74×10^7	2.12×10^7
LHC10c	7.59×10^7	6.14×10^7
LHC10d	1.75×10^8	1.17×10^8
LHC10e	1.47×10^8	8.28×10^7
LHC10f	3.89×10^7	3.63×10^7
LHC10[b-f]	4.64×10^8	3.19×10^8
MC Simulation		
LHC14j4b	2.79×10^7	2.17×10^7
LHC14j4c	7.29×10^7	5.89×10^7
LHC14j4d	1.76×10^8	1.12×10^8
LHC14j4e	1.48×10^8	9.08×10^7
LHC14j4f	3.98×10^7	4.13×10^7
LHC14j4[b-f]	4.65×10^8	3.25×10^8

Table 4.1.: Numbers of accepted events for both reconstruction methods in data and MC simulations after quality assurance and event selection.

within data and MC, otherwise pointing to problems in the reconstruction. Additional quantities that were examined include, amongst others, the fraction of accepted events and the overall number of charged particle tracks. Unfortunately, many runs had to be excluded for the calorimeter measurement due to problematic cells in the calorimeter. The concerned cells were continuously firing at high energies and could have caused a bias in the energy of clusters for which they were included. A calorimeter cluster is the combination of signals from different cells that are attributed to the same incident particle. In general, the rejection of the affected runs can be avoided by an exclusion of the specific cells but this was prevented by time constraints on the analysis.

The list of runs that is left after the procedure is used for data as well as MC. Figures 4.1, 4.2 and 4.3 show a selection of the quantities that were checked, after the selection of good runs. The figures show the fraction of accepted events, the photon candidates or number of clusters and the mass positions of the neutral pion peaks for the different periods and methods per run. It can be deduced that for the accepted runs, the different quantities are in qualitatively good agreement. The slight differences between data and MC that can be observed do not point to any particular problems and therefore do not affect the analysis. The biggest difference between data and MC can be observed in the number of photon candidates per event for the conversion method, figure 4.2 top, for the period LHC10b. However, this difference is still of the order of 5% and does not affect the analysis negatively. The mass positions of the neutral pion peaks, depicted in figure 4.3, show a good agreement between data and MC and are stable within and in between the periods. Overall, the conversion method provides a slightly higher value for the mass that is closer to the literature value. This can be understood considering the better transverse momentum resolution of the conversion method, especially at low p_T where the largest amount of neutral pions is produced.

4. Data Samples and Monte Carlo Simulations

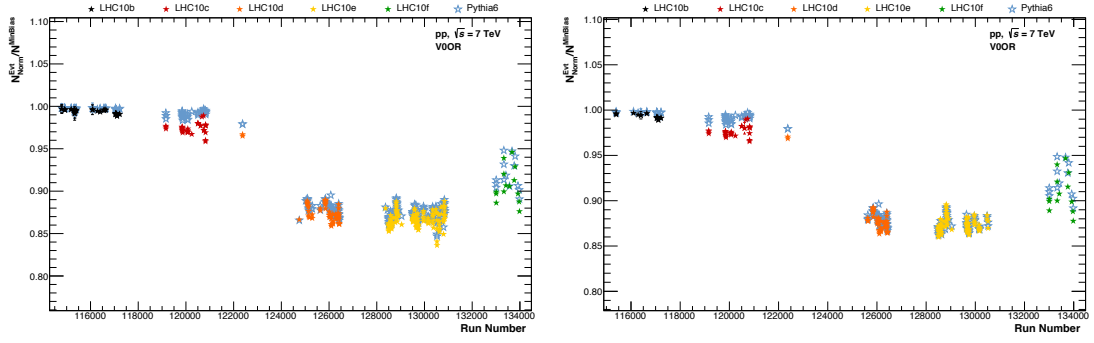


Figure 4.1.: Fraction of accepted events to the total number of recorded minimum bias events per run after the selection of good runs for the conversion (left) and calorimeter (right) measurement.

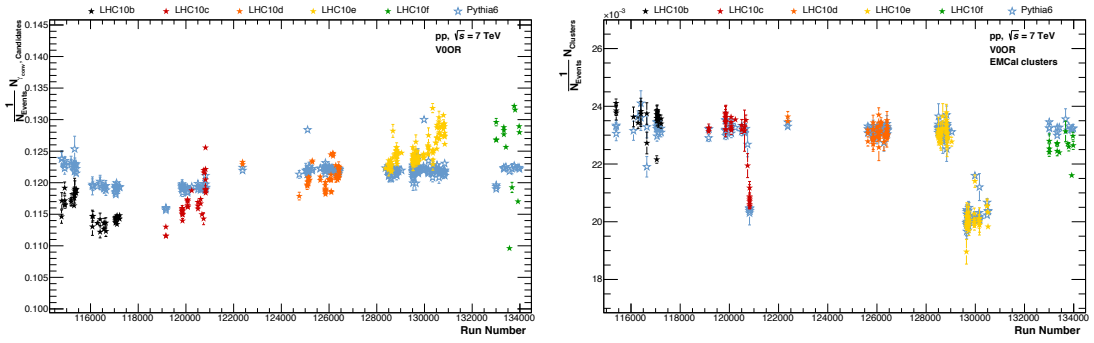


Figure 4.2.: Number of conversion photon candidates (left) and clusters (right) per event and run after the run selection.

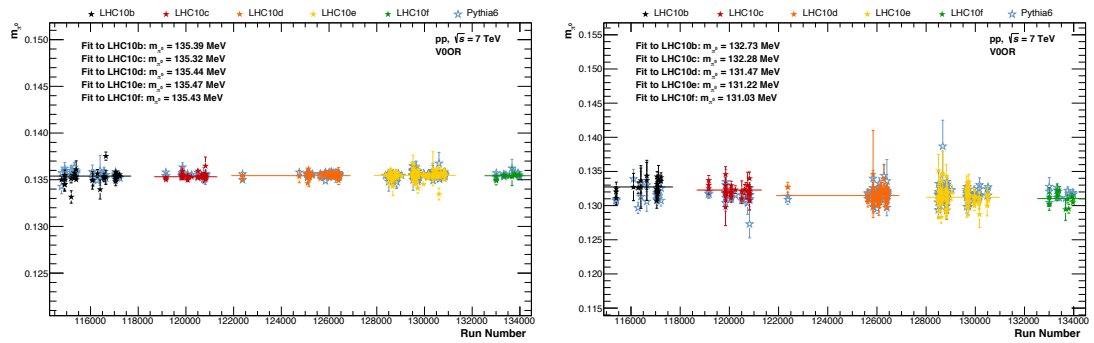


Figure 4.3.: Reconstructed masses of neutral pions, using the conversion (left) and calorimeter (right) method, per run, after the selection of good runs. Additionally, a constant fit to the reconstructed masses per period is shown.

4.4. Event Selection

Events need to pass the event selection in order to be considered in the analysis. This ensures, that only physically interesting events are used, discarding for example beam-gas events that originate in interactions between the beam and residual particles in the non-perfect vacuum of the beam pipe. Such events might still trigger the read-out and must therefore be removed from the sample. Since events are explicitly produced to model proton-proton collisions in the simulations, the event selection on the MC sample is limited to the position of the primary vertex. In order to pass the selection, events must obey the following criteria:

1. The physics selection, that selects the correct trigger assignment has to be passed. Rejecting all interaction that do not originate from beam-beam collisions, i.e. beam-gas interactions, cosmic ray events or noise.
2. The event must have a reconstructed primary vertex from the collision.
3. The position of the primary vertex must be within $|z_{\text{vtx}}| < 10$ cm of the interaction point in order to guarantee optimal reconstruction capability.
4. The event must not be an in-bunch pileup event as discussed in section 3.2.3.

The number of events used for the normalization of the spectra and quoted in table 4.1 can be calculated according to:

$$N_{\text{events}} = N_{\text{MB},|z_{\text{vtx}}|<10 \text{ cm}} + \frac{N_{\text{MB},|z_{\text{vtx}}|<10 \text{ cm}}}{N_{\text{MB},|z_{\text{vtx}}|<10 \text{ cm}} + N_{\text{MB},|z_{\text{vtx}}|>10 \text{ cm}}} \cdot N_{\text{MB,no vtx}}. \quad (4.1)$$

The number of events accepted by the selection criteria is indicated by $N_{\text{MB},|z_{\text{vtx}}|<10 \text{ cm}}$, while events that are discarded due to the position of the primary vertex are labelled with $N_{\text{MB},|z_{\text{vtx}}|>10 \text{ cm}}$. However, there can still be events that end up being recorded but the primary vertex is not identified due to the low multiplicity of the event and therefore an insufficient number of tracks pointing to it. These events, $N_{\text{MB,no vtx}}$, are also considered in equation 4.1, increasing the total number of events that are used. Hereby, the same z distribution is assumed as for events with a reconstructed primary vertex. Therefore, the number of events without primary vertex is scaled by the fraction of events that have a primary vertex within the allowed range in z to the total number of events with reconstructed primary vertex.

5. Inclusive Photon Measurement

The ALICE detector offers two distinct approaches for the reconstruction of photons, which are both used in the analysis presented in this thesis. These techniques are the Photon Conversion Method (PCM) and the reconstruction using calorimeters, explained in more extensive detail in sections 5.1 and 5.2, respectively. Photons can be reconstructed in each calorimeter of the ALICE detector, but this analysis utilizes the EMCal. In general, the energy resolution of a calorimeter improves with energy, but this benefit is limited to some extent in the photon analysis due to the merging of electromagnetic showers in the calorimeter cells.

The PCM reconstructs photons by measuring the electron and positron produced from pair production in the interaction of the photon with the detector material. Due to the excellent tracking capabilities of the TPC, this method provides a very good transverse momentum resolution and can measure photons down to a transverse momentum of $100 \text{ MeV}/c$. The disadvantage of this method is the low conversion probability as well as a reduced resolution at higher momenta due to the decreased bending of the electron and positron tracks in the magnetic field. Above a photon energy of 700 MeV , the calorimetric method can be used for reconstruction. The full EMCal provides a good acceptance, however, in 2010 the coverage of the solid angle was reduced since only four of the total twelve supermodules were installed. In comparison to the conversion method, the EMCal has its strength at larger transverse momenta.

In the following sections, the different reconstruction methods will be described. Furthermore, the different corrections that have to be applied on the measured photon spectra are introduced. The chapter is closed with the calculation of the invariant yields.

5.1. Photon Reconstruction using PCM

Photons that convert to electron-positron pairs in the detector material can be reconstructed by measuring the conversion products. Although the process of pair production is not a particle decay, the topology is identical to the decay of a long-lived particle and can be associated with a secondary vertex that is displaced from the primary vertex of the initial collision. Therefore, it can be processed by the same tracking algorithms that are used for the reconstruction of decays of particles with a long lifetime like the K_s^0 . The full reconstruction of photon candidates using the conversion method proceeds in three steps that are the reconstruction of secondary vertices, the selection of vertices with associated electron-positron pairs and eventually the selection of photons from the conversion products.

5.1.1. Reconstruction of Secondary Vertices

The secondary vertex, that is the starting point of the photon measurement with the conversion method, is reconstructed using a so-called V0 finder. The algorithm searches for vertices where two oppositely charged particles emerge from a single point in space to which no charged mother track can be associated. One such vertex is sketched in figure 5.1, that illustrates the topology and contains the definitions of the parameters associated to the V0. These are the momentum of the V0, the minimum distance of closest approach (DCA) of the two daughter tracks and the radial distance of the primary vertex. The radial distance is referred to as the conversion radius if the secondary vertex is associated to a photon conversion. The parameters of the V0 object are labelled 'P', 'DCA' and 'R', respectively.

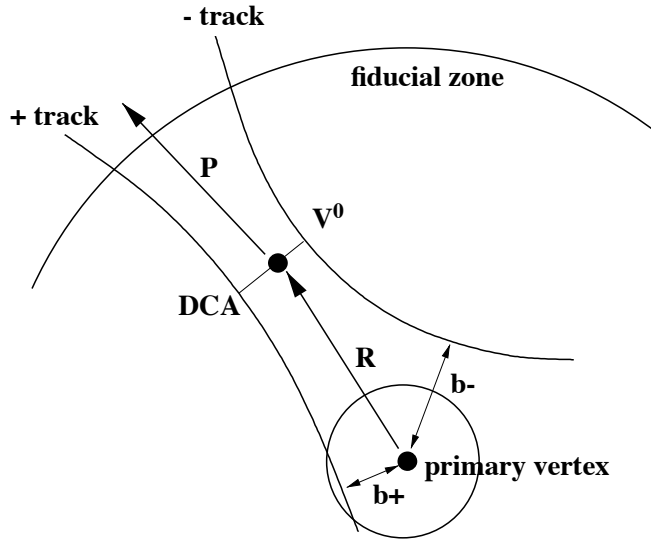


Figure 5.1.: Schematic of the topology of a V0 candidate showing the two oppositely charged tracks with their distance of closest approach (DCA) and the resulting momentum vector. Modified based on [44]

The two V0 finder algorithms used in ALICE are the on-the-fly and offline finder, which are both applied during the initial processing of the data and reconstruction of the tracks. The on-the-fly algorithm is able to modify the tracks under the assumption that they originate from a secondary vertex. In contrast, the offline finder operates on already reconstructed tracks, which can not be modified by the algorithm. Thus a better spatial and momentum resolution of the reconstructed vertices can be achieved by the on-the-fly V0 finder. The on-the-fly finder is therefore used in this analysis. The working principle of the V0 finder is the combination of two oppositely charged tracks under certain criteria to obtain a V0 candidate. The four momentum of the V0 candidate is given by the sum of the four momenta of the two associated tracks. Both component tracks must have a DCA, as indicated in figure 5.1, that is below 1.5 cm for the combination into a V0 candidate. Furthermore, the distances of the extrapolated daughter tracks to the primary vertex, labelled 'b+' and 'b-' in figure 5.1, are checked. This rejects V0 candidates if one or both of the daughter tracks point to the primary

vertex and therefore do not originate from a secondary vertex.

Further cuts on the tracks building the V0 candidates are applied to increase the quality at the first stage of the photon reconstruction. A TPC refit, as described in section 3.2.6, is required for each track component of the V0 candidate and tracks with kinks, that are produced by a decay of a charged particle into a neutral and an equally charged particle, are rejected. The rejection of tracks with a kink topology already removes background V0 candidates since electrons, being the lightest elementary particles, are not expected to decay. The tracks are also required to have a transverse momentum above 50 MeV/ c to reduce the amount of combinatorial background, which is the combination of oppositely charge tracks that do not originate from the same secondary vertex. A minimum fraction of found clusters in the TPC over the theoretically findable clusters, $N_{\text{cluster TPC}}/N_{\text{findable clusters}}$, discards wrong combinations of non-related clusters to tracks. The number of theoretically findable clusters is calculated from the particles trajectory through the TPC. Furthermore, the reconstruction is limited into a fiducial region by a cut on the tracks and V0 candidates pseudorapidity η , that is determined from the angle between the momentum and the direction of the beam line. However, the candidates can lie outside the fiducial region despite fulfilling the criterium of the η cut, since the mother particles have a non-zero decay length. In this case, they are displaced from the position of the primary vertex along the direction of the beam pipe at $Z = 0$. An additional cut, the so-called line cut, that is given by:

$$R_{\text{conv}} > |Z_{\text{conv}}| \cdot \tan(2 \cdot \arctan(e^{-\eta})) - Z_0, \quad (5.1)$$

where $Z_0 = 7$ cm, removes such V0 candidates.

The V0 candidates are associated with a position of the conversion point in radial direction, R_{conv} , as well as in the direction of the beam pipe, Z_{conv} , as it is used in equation 5.1. Since the V0 finder algorithms are designed to reconstruct secondary vertices from the decays of heavier particles, the real conversion point can be displaced from the reconstructed secondary vertex due to an overestimation of the opening angle. In the case of a photon conversion, the opening angle of the emerging electron-positron pair vanishes. Thus, the momenta of the pair are, in reality, parallel in the conversion point. With this additional constraint, the conversion point that is obtained from the V0 finder is recalculated. Further geometric cuts on conversion point are applied to keep the candidates in the fiducial region of the detector. A minimum value of $R_{\text{conv}} > 5$ cm is used on the conversion radius to reject V0 candidates that originate from Dalitz decays of neutral mesons. In contrast to the decay into two real photons, one photon is instantaneously decaying into a electron-positron pair in the Dalitz channel. This electron-positron pair might be reconstructed as a real photon although it originates from a virtual one. All cuts that are used for the track selection are summarized in table 5.1.

5.1.2. Selection of Electron-Positron Pairs

So far, no identification on the particle species of the two component tracks of the V0 candidates was applied. Therefore, the V0 candidates can either be converted photons or neutral particles that decayed into two oppositely charged daughters. The next step

V0 and track selection	
V0 finder	on-the-fly
minimum track p_T	$> 50 \text{ MeV}/c$
$N_{\text{cluster TPC}}/N_{\text{findable clusters}}$	$> 60\%$
maximum pseudorapidity η	$ \eta < 0.9$
R_{conv}	$5 \text{ cm} < R_{\text{conv}} < 180 \text{ cm}$
Z_{conv}	$ Z_{\text{conv}} < 240 \text{ cm}$

Table 5.1.: Cuts applied on the V0 candidates and the associated component tracks.

towards the sample of reconstructed photons, although not yet ensuring perfect purity, is the selection of electron-positron pairs by exploiting the particle identification capabilities of the ALICE detector. The main particle identification tool of the detector is the TPC, providing a measurement of the specific energy loss per unit length, dE/dx . The mean energy loss of a charged particle via ionization can be described with the Bethe-Bloch formula [45, 46]. The formula relates the mean energy loss to the particle's velocity and charge. Different particle species can therefore be distinguished by comparing their energy loss at a given momentum. The differences in energy loss at the same momentum can be related to differences in the particle's velocity, which in turn gives information about the differences in mass. Therefore, particle species can either be selected or rejected according to the deviation of their specific energy loss from parametrizations of the mean values for different species at a certain momentum. The deviation between the measured and expected energy loss of a particle of species X can be expressed in terms of numbers of standard deviations around the hypothesis. Hereby, the hypothesis can be identified with the parametrization of the mean energy loss of a certain species. With the standard deviation given by the resolution of the energy loss measurement, the deviation can be expressed as:

$$n\sigma_X = \frac{dE/dx - \langle dE/dx|_X \rangle}{\sigma_{\langle dE/dx|_X \rangle}}. \quad (5.2)$$

The upper panel of figure 5.2 shows the TPC dE/dx , that is used to select electron and positron tracks for the V0 candidates. All tracks that lie within a certain $n\sigma$ range of the parametrization of the electron energy loss curve are accepted. The deviations from the electron hypothesis in terms of standard deviations are shown in the bottom panel of figure 5.2. Furthermore, pions are rejected using the information on the deviation to the pion hypothesis. Because the electron and pion dE/dx bands cross at momenta between $0.1 \text{ GeV}/c$ and $0.2 \text{ GeV}/c$, as can be seen in figure 5.2, the pion rejection can only be done down to $p > 0.4 \text{ GeV}/c$. This limit is ultimately given by the width of the pion band at the crossing. The energy loss distribution in the Monte Carlo simulations would have to reproduce the data in this regime very precisely to avoid large uncertainties when cutting into the region of the crossing of the bands. This can not be guaranteed and thus pions are only rejected down to a transverse momentum of $0.4 \text{ GeV}/c$. The comparison of the left and right panels in figure 5.2, that correspond to the distributions before and after all selection cuts were applied, show that a rather

clean electron sample is obtained. The main contamination that is left after the particle identification is the contribution of pions at momenta between 0.1 GeV/c and 0.2 GeV/c, that can not be removed safely. All cuts that are applied on the specific energy loss measured in the TPC are summarized in table 5.2.

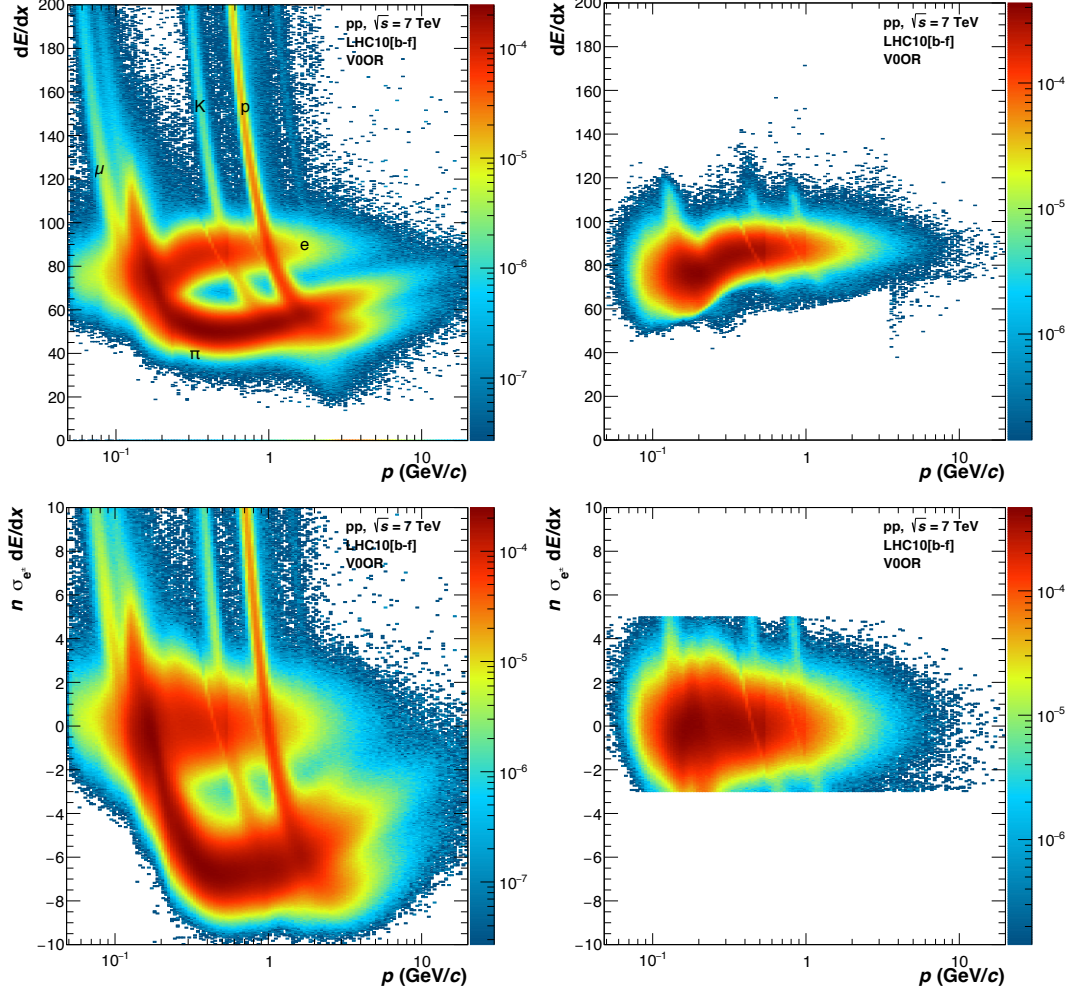


Figure 5.2.: Specific energy loss of different particles before (left) and after (right) all selection cuts were applied. The top panel shows the TPC dE/dx information with the deviation from the electron hypothesis shown in the bottom panel.

Figure 5.2 also shows contributions from other particle species like kaons and protons that cross the electron band at different momenta. Unfortunately, these contaminations can not be removed by cuts in the energy loss distributions without losing the signal in the corresponding momentum regions. These contributions are, however, of much smaller magnitude than the pions that are produced in large abundancies in the collision and are later corrected for, using information from the Monte Carlo simulations.

There are, in general, also other particle identification methods available with the

Electron selection			
$n\sigma_e$	TPC dE/dx	$-3 < n\sigma_e < 5$	
$n\sigma_\pi$	TPC dE/dx	$n\sigma_\pi > 1$	$0.4 \text{ GeV}/c < p < 3.5 \text{ GeV}/c$
		$n\sigma_\pi > -10$	$p > 3.5 \text{ GeV}/c$

Table 5.2.: Summary of $n\sigma$ TPC dE/dx ranges around the respective energy loss parametrizations used for the selection of electrons.

ALICE detector, that are, for example, provided by the Transition Radiation Detector (TRD) or the TOF system. However, additional particle identification methods only marginally improve the signal to background ratio while mainly decreasing the efficiency of the measurement due to the strong selection cuts that are applied. Thus, no additional particle identification is used in the analysis.

5.1.3. Selection of Photon Candidates

The track selection criteria and particle identification cuts have removed a large amount of V0s with non-electron tracks as well as secondary vertices from particle decays. However, the V0 sample can still contain candidates from combinatorial pairs of oppositely charged particles or candidates from particle decays which were not discarded by the particle identification cuts. These random combinations or falsely identified secondary vertices can only be removed by a selection of photon-specific criteria on the V0 candidates.

The easiest selection that can be done is on the angle between the momentum of the V0 and the vector pointing from the primary vertex to the conversion point, labelled 'R' in figure 5.1. This angle, $\theta_{\text{point.}}$, is called pointing angle and takes values close to zero for real secondary vertices, while the values for combinatorial background are randomly distributed. Therefore, a cut on this value can reject random combinations of tracks that are paired to V0s.

In the absence of a magnetic field, the opening angle of an electron-positron pair coming from a photon conversion is small due to the vanishing invariant mass. The measured opening angle can be enlarged when the pair production is happening inside a magnetic field due to the bending of the charged tracks and a displacement of the measured track coordinates from the conversion point. When these effects are disentangled, a cut can remove a lot of combinatorial background with non-vanishing and randomly distributed invariant masses. The variable that can be used for this is the angle Ψ_{Pair} between the plane that is defined by the electron-positron pair and the plane perpendicular to the magnetic field [47]. In ALICE, the latter is given by the x - y -plane since the magnetic field is pointing along the beam line, which defines the z direction. Due to the geometry of the magnetic field, that only bends charged tracks in azimuthal direction, this angle can be defined as:

$$\Psi_{\text{Pair}} = \arcsin\left(\frac{\Delta\theta_{e^-e^+}}{\xi_{\text{Pair}}}\right), \quad (5.3)$$

where $\Delta\theta_{e^-e^+} = \theta_{e^-} - \theta_{e^+}$ is the opening angle of the pair with respect to the polar

angle. The second angle in equation 5.3 is the opening angle in the plane that is defined by the momenta of the pair. This angle can be written as:

$$\xi_{\text{Pair}} = \arccos \left(\frac{\vec{p}_{e^-} \cdot \vec{p}_{e^+}}{|\vec{p}_{e^-}| \cdot |\vec{p}_{e^+}|} \right). \quad (5.4)$$

Figure 5.3 shows the geometry of the electron-positron pair and the angles to the different planes. The angle Ψ_{Pair} is narrowly peaked at zero for pairs from conversions of real photons due to the vanishing opening angle of the pair in the absence of a magnetic field. It takes larger and randomly distributed values for the background of combinatorial pairs.

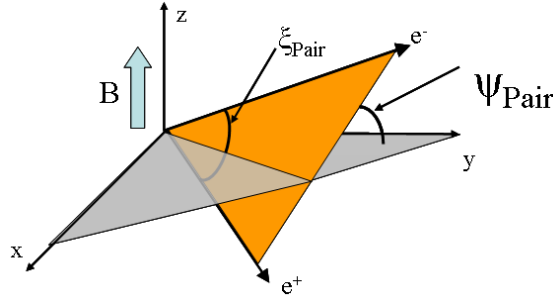


Figure 5.3.: Angle Ψ_{Pair} between the plane that is defined by the conversion pair, with the opening angle ξ_{Pair} , and the x - y -plane. [47]

The conversion topology can further be exploited by selecting the appropriate region in the Armenteros-Podolanski plot shown in figure 5.4. The plot shows the relative momentum of the daughters with respect to the V_0 momentum and perpendicular to it,

$$q_{\text{T}} = \frac{|\vec{p}_{e^\pm} \times \vec{p}_{V_0}|}{|\vec{p}_{V_0}|}, \quad (5.5)$$

versus the longitudinal momentum asymmetry of the two conversion daughters,

$$\alpha = \frac{p_{L,e^-} - p_{L,e^+}}{p_{L,e^-} + p_{L,e^+}}, \quad (5.6)$$

where the longitudinal direction is given by the direction of the V_0 momentum. The area that is spanned by these variables allows for a good discrimination between symmetric and asymmetric pairs from particle decays or conversions, which can nicely be seen in figure 5.4. For pairs of equal mass, like electron-positron pairs from a photon conversion or a pair of oppositely charged pions from the decay of a K_S^0 , the distributions are symmetric and peaked at $\alpha = 0$. In the case of asymmetric decays, like $\Lambda \rightarrow p\pi^-$ or $\bar{\Lambda} \rightarrow \bar{p}\pi^+$, the distributions are shifted with respect to α . Combinatorial background is randomly distributed since there is no physical relation between the relative momenta of the tracks and the asymmetry in longitudinal direction. A two-dimensional cut in the $q_{\text{T}}-\alpha$ -plane is applied, that selects an elliptical region around the photon signal to

reject combinatorial and decay background:

$$\left(\frac{\alpha}{\alpha_{\max}}\right)^2 + \left(\frac{q_T}{q_{T, \max}}\right)^2 > 1 \quad (5.7)$$

Figure 5.4 shows the Armenteros-Podolanski plot for photon candidates in data before and after the elliptical cut was applied. It can be seen that the contributions from decays of K_S^0 or Λ and $\bar{\Lambda}$ are removed to a large extent. However, there can still be combinatorial background lurking in the selected region due to the random distribution in the q_T - α -plane.

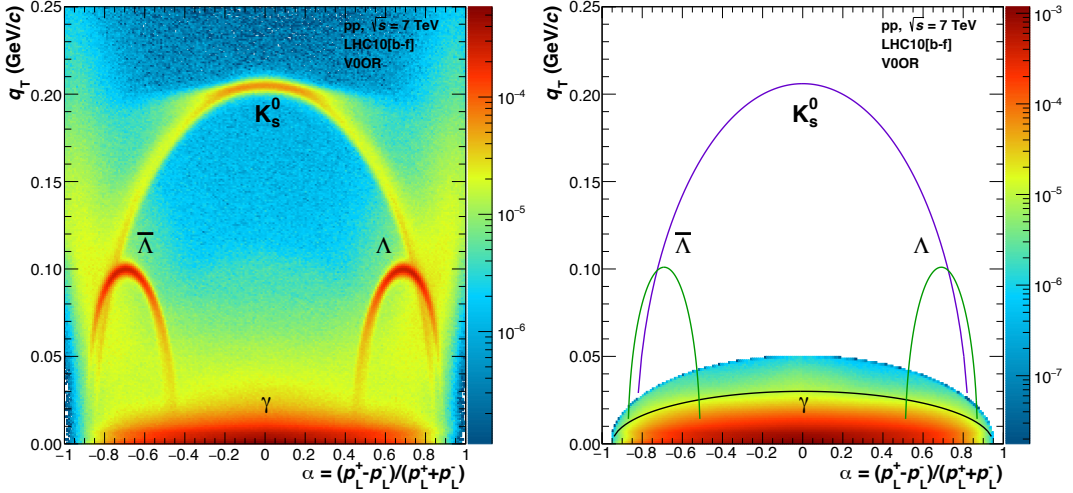


Figure 5.4.: Armenteros-Podolanski plot before (left) and after (right) the selection according to equation 5.7 was applied. Contributions from decays of K_S^0 , Λ and $\bar{\Lambda}$ are labelled accordingly.

Furthermore, a selection can be done based on the quality of the Kalman filter method to build the secondary vertices. This algorithm performs a fit to the decay topology that is constrained by the mass, which is set to zero for photon candidates. The fit quality χ^2 and the number of degrees of freedom of the fit, which are given by the amount of parameters included in the hypothesis, can be used for a discrimination between signal and background. Therefore, a cut on the reduced χ^2 , that is $\chi_{\text{red.}}^2 = \chi^2/\text{ndf}$, is introduced. In this analysis, a two-dimensional cut is applied that combines the information on the angle Ψ_{Pair} and the reduced χ^2 in a triangular form:

$$\left(1 - \frac{\chi_{\text{red.}}^2}{\chi_{\text{red., max}}^2}\right) \cdot \Psi_{\text{Pair, max}} > |\Psi_{\text{Pair}}| \quad (5.8)$$

The combination of the information on the quality of the Kalman filter approach and the angle Ψ_{Pair} ensures the optimal discrimination that can be achieved with the use of these variables.

All cuts that are described above are used in the analysis to select photons from the sample of V0 candidates. The values of the cuts, that are summarized in table 5.3, were

chosen to optimize the signal to background ratio while still maintaining an adequate efficiency. The maximum values for the two dimensional cuts defined in equations 5.7 and 5.8 are quoted.

Photon selection	
pointing angle	$\cos(\theta_{\text{point.}}) > 0.85$
Armenteros-Podolanski plot (eq. 5.7)	$q_{\text{T, max}} < 0.05 \text{ GeV}/c$ $ \alpha_{\text{max}} < 0.95$
Ψ_{Pair} and $\chi_{\text{red.}}^2$ (eq. 5.8)	$\Psi_{\text{Pair, max}} < 0.1$ $\chi_{\text{red., max}}^2 < 30$

Table 5.3.: Summary of the cuts applied on the sample of V0 candidates for the selection of photons.

5.2. Photon Reconstruction with EMCal

In this section, the photon reconstruction with the EMCal is presented. Photons are reconstructed in calorimeters by measuring the energy deposit from electromagnetic showers in the calorimeter cells. The dominant processes hereby are pair production by photons and bremsstrahlung of electrons with the emerging particles contributing to the shower likewise. While PHOS has already been used for the measurement of direct photons, the same has not been done with the EMCal up to now. This poses a particular challenge on the analysis and it is not aimed for fully comprehensive results including an evaluation of the systematic uncertainties. The reconstruction using the EMCal should rather be perceived as a first attempt at the measurement in order to identify possible obstacles. However, all ingredients to the direct photon measurement, including the excess ratio, are analyzed.

The reconstruction of photons with the calorimeter starts with the identification of calorimeter clusters. These are then selected according to different criteria to obtain the candidates that were most likely produced by photons. In analogy to the V0 candidates in the conversion measurement, the clusters are then considered as photon candidates that have to be corrected further using MC information.

5.2.1. Cell Selection and Clusterizer

The calorimeter is designed such that the energy which is deposited by the electromagnetic shower is typically not contained in a single calorimeter cell, but distributed over several. These cells are combined into clusters by clusterizer algorithms. In this analysis, the so-called V2 clusterizer, which is a clusterizer algorithm implemented in AliRoot, is used. The first step in this process is the search for a seed cell that must have an energy above the threshold value of $E_{\text{seed}} = 0.5 \text{ GeV}$. Adjacent cells are perpetually added as long as they have an energy lower than the neighbouring cell but above 0.1 GeV. The clusterization continues as long as cells are found that fulfill these requirements and are not yet contributing to a different cluster. In addition, the energy signal in the cells must be recorded within a certain cluster time of flight window to be

considered. All cell selection conditions in the clusterization procedure are summarized in table 5.4.

Cell selection	
clusterizer algorithm	V2
seed energy threshold	$E_{\text{seed}} > 0.5 \text{ GeV}$
cell energy threshold	$E_{\text{min}} > 0.1 \text{ GeV}$
cell time	$ t_{\text{cell}} < 500 \text{ ns}$

Table 5.4.: Cell selection thresholds in the clusterization procedure.

5.2.2. Cluster Selection

Once the calorimeter clusters are identified by the clusterizer algorithm, further cuts are applied to select those, that are most likely produced by a photon. Clusters are required to be composed of at least two calorimeter cells to reject electronic noise fluctuations from single cells. The cluster energy must be above 0.7 GeV to remove contamination and ensure a reasonable energy resolution. Furthermore, calorimeter clusters that can be matched to a charged particle track within a certain window in the η - ϕ -plane are discarded, since neutral particles like photons will not leave a track in the detector's tracking devices. The distances that are chosen depend on the transverse momentum of the charged particle track and are listed in table 5.5. Charged tracks are propagated to the surface of the EMCal if their momenta are large enough and if they lie within the geometrical acceptance of the calorimeter. If the propagation is not possible, the track is not considered in the track matching.

Furthermore, the shape of the clusters can be used to identify photon candidates. Hereby, the cluster can be described as an ellipse in the η - ϕ -plane with the long axis expressed as:

$$\lambda_{\text{long}}^2 = 0.5 \left(\sigma_{\phi\phi}^2 + \sigma_{\eta\eta}^2 + \sqrt{(\sigma_{\phi\phi}^2 - \sigma_{\eta\eta}^2)^2 + 4\sigma_{\phi\eta}^2} \right), \quad (5.9)$$

where $\sigma_{xy}^2 = \langle xy \rangle - \langle x \rangle \langle y \rangle$ is the covariance of two variables x and y . The mean values in the covariance depend on the energy of the cell they are attributed to and are given by:

$$\langle x \rangle = \frac{1}{w_{\text{tot.}}} \sum_i w_i x_i \quad \text{and} \quad \langle xy \rangle = \frac{1}{w_{\text{tot.}}} \sum_i w_i x_i y_i, \quad (5.10)$$

with the sum running over all cells in the cluster and the cells being weighted with $w_i = \max(0, 4.5 + \log E_i/E)$ [48]. The total weight $w_{\text{tot.}}$ is given by the sum over all weights w_i of the cluster. The energies E_i and E are the energy of a single cell in the cluster and the energy of the cluster, respectively. The selection of the cluster shape is based on a cut on the long axis of the ellipse λ_{long}^2 , with the values quoted in table 5.5. The minimum value of $\lambda_{\text{long}}^2 > 0.1$ is applied to discard nuclear interactions which deposit most of the energy in a single cell. Electron and photon showers are

broader spread over several cells with real photons resulting in values of $\lambda_{\text{long}}^2 \approx 0.25$. These showers can become more elliptical due to conversions that happen close to the calorimeter, with a single cluster produced by the electron-positron pair. Additionally, clusters can become even stronger elongated if a high transverse momentum neutral pion decays into two photons and both are reconstructed in a single cluster. The background from neutral pion decays and conversions close to the calorimeter is suppressed by a maximum value of $\lambda_{\text{long}}^2 < 0.5$.

All cuts that are used to select the photon candidates from the sample of clusters that was obtained by the clusterizer algorithm are summarized in table 5.5.

Cluster selection	
cluster energy threshold	$E_{\text{cluster}} > 0.7 \text{ GeV}$
min. number of cells per cluster	≥ 2
shower shape parameter M_{02}	$0.1 \leq \lambda_{\text{long}}^2 \leq 0.5$
track matching	$ \Delta\eta \leq 0.010 + (p_{\text{T}} + 4.07)^{-2.5}$ $ \Delta\phi \leq 0.015 + (p_{\text{T}} + 3.65)^{-2}$

Table 5.5.: Cuts applied on clusters to select photon candidates.

The η - ϕ distributions of the clusters after all selection cuts are applied are shown in figure 5.5 for data and MC. The distributions are normalized to the number of events and the overall average number of clusters per η - ϕ bin. At the time the data was taken, only four of the total twelve supermodules of the EMCal were installed, hence the additionally reduced coverage that is given by the geometrical acceptance of the calorimeter. The clusters are reasonably uniform distributed over the supermodules and the dead areas are correctly reproduced by the MC. However, the structures that are visible for $\eta < 0$ are slightly more expressed in the data than in the corresponding simulations.

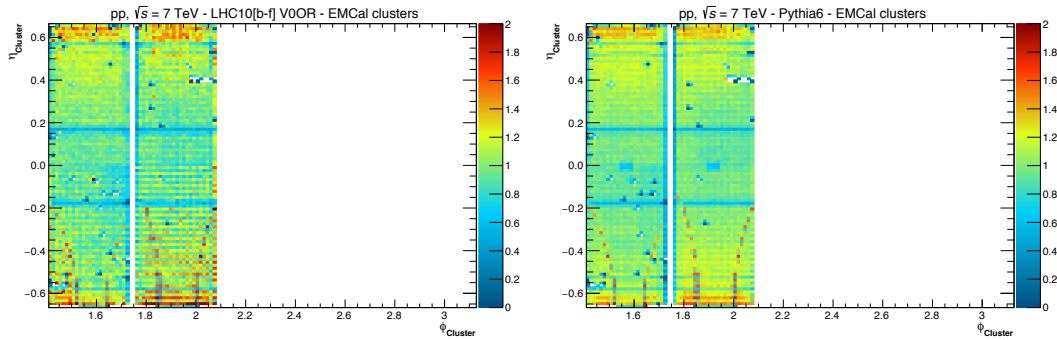


Figure 5.5.: Distribution of EMCal clusters in the η - ϕ plane for data (left) and MC (right).

5.2.3. Cluster Energy Correction

The cluster energy is given by the sum of the energies of all the cells associated to the cluster. Typically, the absolute energy is corrected for a non-linear detector response

by using test-beam measurements in order to match the cluster energies between data and Monte Carlo simulations. But since the conditions during test-beam and collision data taking do not correspond, a different approach is used in this analysis. The energy calibration can be performed independently based on a comparison of the neutral pion peak positions in data and Monte Carlo and is then applied to the cluster energies of the latter, deteriorating the resolution in the simulations [49]. Figure 5.6 shows the ratios of the reconstructed neutral pion mass in data and MC with respect to the PDG value [50]. Hereby, the neutral pions were reconstructed from the combination of calorimeter and conversion photons to be able to directly access the cluster energy dependence. Additionally, the combination benefits from the superior momentum resolution of the conversion method. It can be seen that the reconstructed mass in data is consistently underestimated by the MC simulation over all cluster energies. Thus, the MC cluster energies have to be corrected upwards in order to match the data. Figure 5.6 also shows a power law fit to the distributions in data and MC.

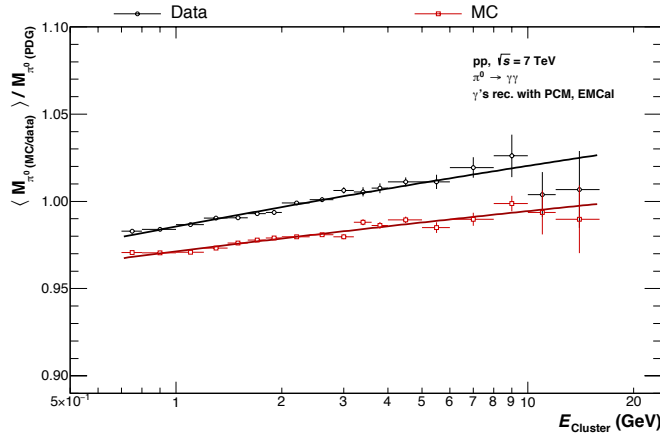


Figure 5.6.: Ratio of reconstructed π^0 mass using PCM-EMCal in data and MC to the PDG value, including a power law fit to the respective distributions.

The correction of the MC cluster energies is produced in three steps, starting with the reconstruction of neutral pions and the determination of the invariant mass in bins of the cluster energies, as it is shown in figure 5.6. The next step, is the calculation of the ratio of the reconstructed mass in MC to data. The final correction factor that has to be applied on the MC cluster energies is then either produced by a direct exponential fit to the ratio of the reconstructed masses in MC and data, or by calculating the ratio of the fits shown in figure 5.6.

The left panel of figure 5.7 shows the ratio of the reconstructed masses in MC to data. Again it can be seen, that the simulations underestimate the invariant mass that is reconstructed in the data. The exponential fit to the ratio is also shown as a red line, with the ratio of the fits from figure 5.6 shown in green as a comparison. The final correction factor, that is applied on the MC cluster energies, is shown in the right panel of figure 5.7, with the black line displaying the inverse of the direct fit to the ratio of the invariant masses, that is used in this analysis. The correction factor that is determined by the ratio of the fits shown in figure 5.6 is displayed by the green curve in

the right panel in figure 5.7. Both correction factors agree very well over a large part of the cluster energy range, with the largest deviation of about 5% at the highest cluster energies.

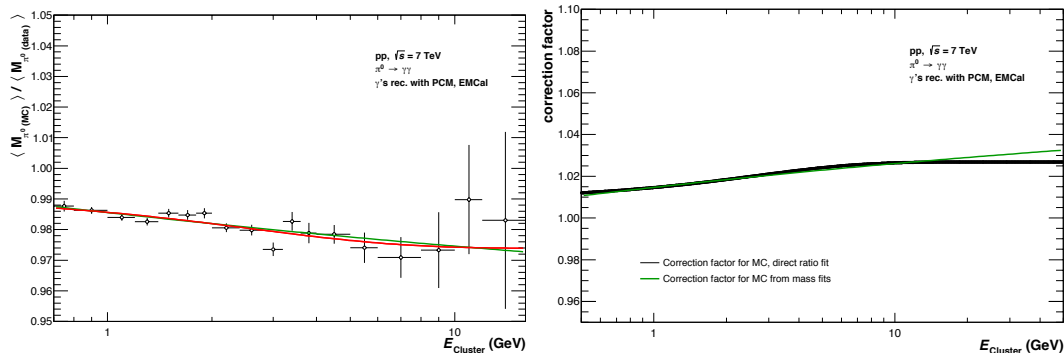


Figure 5.7.: Ratio of the reconstructed invariant π^0 mass in MC to data (left) and the MC cluster energy correction factor (right).

5.3. Corrections to Measured Photon Spectra

After the selection criteria described in the previous sections are applied on the initial sample of V0s and clusters, the identified photon candidates are either correctly selected or background with very similar characteristics. The measured raw spectra have to be corrected for reconstruction efficiencies and the resolution of the respective method, contributions from secondary decays and misidentified signals, as well as the conversion probability in the case of the conversion measurement. The correction factors are obtained from MC simulations with the exception of the secondary contribution that is determined with a data-driven approach. All corrections that are applied on the initial spectra are described in the following, with the corrections that have to be done on either method shown side-by-side. The corrections are introduced in the order in which they are applied on the measured spectra.

5.3.1. Out-of-Bunch Pileup Correction

It was already mentioned in section 3.2.4, that due to interaction rate combined with the long time integration, several events can overlap inside the TPC. This leads to tracks that are falsely assigned to the current event. During the event selection, overlapping events from the same bunch, called in-bunch pileup events, are discarded using information from the SPD layers of the ITS. The SPD, however, only provides protection against past or future events while there can still be drifting charges inside the TPC after one full revolution of the bunches inside the LHC. These TPC tracks, called out-of-bunch pileup tracks, are stored and read out for the current event due to the long integration time. This does not hold for global tracks which are also assigned with ITS information due to the much smaller integration time of the ITS. The contribution from out-of-bunch pileup has to be corrected for since the sole use of tracks with ITS information available would significantly reduce the available statistics. In the case of the

calorimeter measurement, the clusters are assigned with time information. While this information is not perfect, the relatively low interaction rate ensures that the correction for out-of-bunch pileup is not required for the EMCal measurement.

In the case of the conversion measurement, the photon candidates are composed of two charged tracks each and the final V0 sample has to be checked and corrected for contributions from pileup tracks. Due to the pairing of two tracks, three different categories of V0s can be considered concerning track information: 1) both tracks of the V0 have only TPC information, 2) one of the two tracks additionally has ITS information and 3) both tracks have information from the TPC and ITS.

Naturally the third category of photons is not affected by out-of-bunch pileup since both tracks are assigned with ITS information and thus can not originate from an earlier event. The second category should also be free of out-of-bunch pileup if the V0 candidate corresponds to a real photon, since one of the two daughter tracks was reconstructed with the ITS. However, the correction for out-of-bunch pileup is applied before the sample of photon candidates is corrected for purity and thus the V0 can contain combinatorial background. Therefore, some contribution from pileup can linger in the second category. Photons from category one are obviously most vulnerable to pileup since both charged tracks assigned to the V0 are missing ITS information and can thus belong to an earlier event, regardless of whether the candidate is a real photon or a combinatorial pair. Due to the already advanced drift of the charges in the TPC, contributions from out-of-bunch pileup show an increased distance of closest approach in the z -direction, DCA_z , of the photon momentum to the primary vertex.

The left panel of figure 5.8 shows the p_T integrated DCA_z distribution of photons from the first category. The background from out-of-bunch pileup can be seen in the widened distribution under the peak. The contribution from background is estimated using a ROOT integrated function that scans the distribution for peaks and subtracts those in an iterative process. This leads to a reasonable description of the broad and symmetric distribution under the peak. After the subtraction of the background estimate, the DCA_z distribution is much more narrowly peaked around $DCA_z = 0$ and resembles the distributions that are obtained for category three photons, which are shown in appendix A.1.

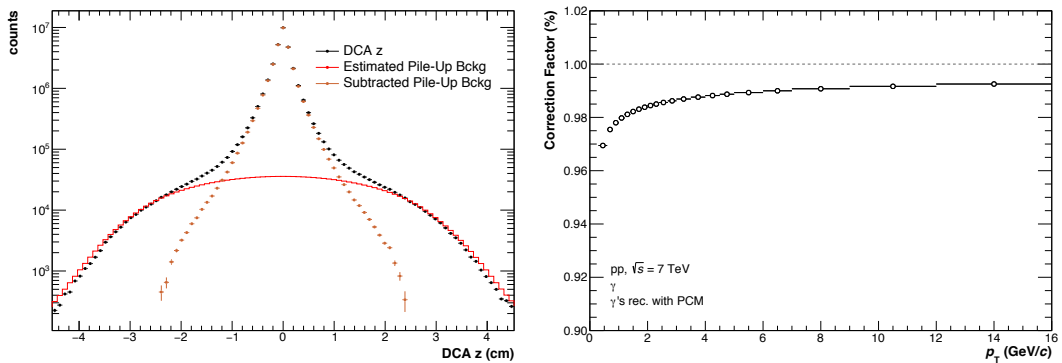


Figure 5.8.: Integrated DCA_z distribution for all photons from category one, including the out-of-bunch pileup background estimate (left) and out-of-bunch pileup correction factor (right).

The out-of-bunch pileup correction is obtained by estimating the pileup background for the first two categories of photons in p_T bins and comparing the background subtracted distributions to the original ones. Since no pileup is expected in the third category, no background estimate is performed there. The correction factor is determined according to:

$$C_{\text{pileup}}(p_T) = \frac{\gamma_{\text{pileup sub.}}^{\text{cat. 1}}(p_T) + \gamma_{\text{pileup sub.}}^{\text{cat. 2}}(p_T) + \gamma^{\text{cat. 3}}(p_T)}{\gamma^{\text{cat. 1}}(p_T) + \gamma^{\text{cat. 2}}(p_T) + \gamma^{\text{cat. 3}}(p_T)}, \quad (5.11)$$

where the subscript 'pileup sub.' labels the pileup background subtracted distributions. The result of equation 5.11 is then fitted with a power law in order to reduce statistical fluctuations. The correction factor that is applied to the measured spectrum is shown in the right panel of figure 5.8. The DCA_z distributions for the three different categories are shown in appendix A.1 in transverse momentum bins, including the background estimates. The correction factor that is obtained from equation 5.11 is the inverse of the relative contribution from out-of-bunch pileup and therefore always smaller or equal to one. As it is expected for the relatively low interaction rate, the contribution from out-of-bunch pileup is comparably low with the largest magnitude of 3% in the lowest p_T bin.

5.3.2. Secondary Correction

Particles that are produced in the initial collision are called primary particles. This definition also includes particles from strong and electromagnetic decays that happen very close to the primary vertex and can therefore not be resolved. In the case of photons, the definition of primary particles extends to photons that originate from the decay of primary particles. The dominating source of secondary photons is the weak decay of the K_S^0 through the decay chain $K_S^0 \rightarrow 2\pi^0 \rightarrow 4\gamma$. Due to the long lifetime and consequential decay length $c\tau \approx 2.68$ cm, the photons do not originate from the primary vertex. Further sources of secondary photons are weak decays of K_L^0 , Λ and other particles, where the relative contributions to the total secondary spectrum depend on the method of the measurement. Regarding the long lifetime of the K_L^0 , $\tau \approx 5.12 \times 10^{-8}$ s, photons originating from subsequent decays are not as likely being reconstructed through conversions before or in the TPC as photons from decays of the K_S^0 . In contrast, the contribution from K_L^0 is more significant in the calorimeter measurement since the EMCal is situated at larger radii.

Eventually, the inclusive spectrum should only contain primary photons, hence the contribution of secondaries has to be determined and subtracted from the measured spectrum. Secondary photons, however, can not be identified from the data alone since no tracking information and therefore no information on the production radius is available for the photon.

A data driven approach for the determination of the secondary photon contribution is used in this analysis. This approach is based on measured K_S^0 and Λ spectra in proton-proton collisions at $\sqrt{s} = 7$ TeV and uses a simulation of particle decays. The decay simulation is produced with the same framework that provides the decay photon cocktail used in the photon double ratio, described in more detail in section 7. The

mother particles are produced according to the measured and fully corrected spectra and the decays are simulated using PYTHIA 6.4. Thus, the secondary photon spectra from K_S^0 , K_L^0 and Λ are obtained excluding the detector response, which has to be folded into the spectra subsequently. This is done using the reconstruction efficiencies and conversion probabilities for secondary photons from the different sources calculated from the detector simulation. The calculation of the reconstruction efficiency and conversion probability is introduced in chapters 5.3.4 and 5.3.5, respectively. Naturally, the conversion probability is only required for the conversion measurement while the reconstruction efficiencies are calculated for both methods. While an unfolding technique is used to correct the primary spectrum for the detector response, the same is not possible for the secondary spectra due to a lack of statistics. Hence, the resolution is also obtained from MC and included into the reconstruction efficiency. The particle decays are simulated over the full range of 2π in azimuth and within the pseudorapidity coverage of the TPC. Since the solid angle of the calorimeter is reduced with respect to the simulation, the secondary spectra for the calorimeter measurement are also folded with the acceptance, which is included in the reconstruction efficiency of this method. Secondary photons that originate from material interactions can not be determined with a data driven approach and are taken from MC.

The secondary photon reconstruction efficiencies for both methods are shown in figure 5.9. Hereby, the reconstruction efficiencies for secondaries from K_L^0 and Λ are scaled from the primary reconstruction efficiency since the statistics otherwise does not allow for a reasonable description. The reconstruction efficiencies for secondaries resemble the shape of the primary reconstruction efficiency shown in section 5.3.4, although being reduced in the case of the conversion measurement due to the larger production radius. Due to the large decay length of the K_L^0 , the reconstruction efficiency for secondaries from this particular contribution is suppressed for the conversion measurement. In the case of the calorimeter measurement, the reconstruction efficiency for secondary photons from K_L^0 or Λ decays exceeds the reconstruction efficiency for secondary photons from K_S^0 decays. This is attributed to the fact that the resolution correction is folded into the reconstruction efficiency. In the case of the calorimeter measurement, the transverse momentum is reconstructed under the assumption that the particle originates from the primary vertex, thus the resolution gets worse if the particle has a longer lifetime

In addition, the secondary photon conversion probabilities are shown in figure 5.10 for the conversion measurement. The conversion probabilities for secondary photons from K_S^0 expose a different shape than the primary photon conversion probability described in section 5.3.5. A possible explanation can be given in terms of the production radius of the secondary photons. While primary photons are produced close to the collision vertex, secondary photons are produced with a distinct displacement in radial direction, reducing the material that is crossed. This affects the conversion probability particularly since the detector material is not homogeneously distributed. Again, the statistics are not sufficient to reasonably describe the conversion probability for secondaries from K_L^0 and Λ . Thus, the conversion probability for secondaries from Λ are scaled from the primary conversion probability. In the case of secondary photons from K_L^0 , the conversion probability is reasonably described up to 6 GeV/c. For larger transverse momenta and missing bins, a constant fit to the conversion probability above 2 GeV/c is used with the uncertainty given by the uncertainty of the fit.

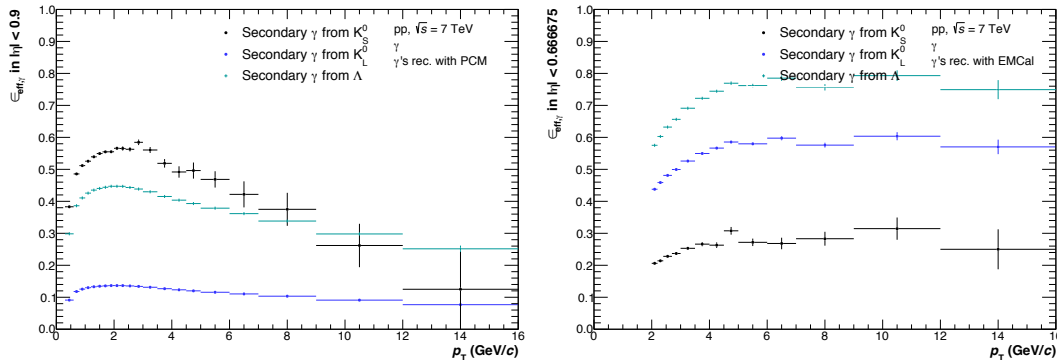


Figure 5.9.: Reconstruction efficiencies for secondary photons from K_S^0 , K_L^0 and Λ decays for the reconstruction using the conversion method (left) and the calorimeter (right).

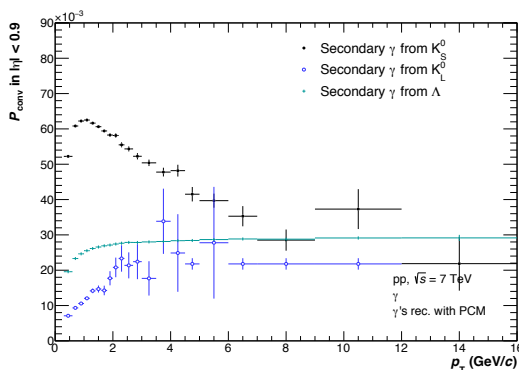


Figure 5.10.: Conversion probabilities for secondary photons from decays of K_S^0 , K_L^0 and Λ .

The raw secondary photon spectra are obtained by multiplying the secondary spectra from the decay simulation with the reconstruction efficiency and the conversion probability in the case of the conversion measurement. The raw primary photon spectrum is then calculated by subtracting the secondary from the measured photons:

$$\gamma_{\text{rec., sec. corr.}}^{\text{data}}(p_T) = \gamma_{\text{rec.}}^{\text{data}}(p_T) - \sum \gamma_{\text{sec. from X}}^{\text{decay}}(p_T), \quad (5.12)$$

where the sum runs over the different sources of secondary photons that are considered, i.e. K_S^0 , K_L^0 , Λ and material interactions. Hereby, the secondary spectra $\gamma_{\text{sec. from X}}^{\text{decay}}(p_T)$ are already multiplied with the reconstruction efficiency and conversion probability, respectively. This holds with the exception of secondary photons from material interactions that are taken directly from MC. In the case of the conversion measurement, $\gamma_{\text{rec.}}^{\text{data}}(p_T)$ was already corrected for out-of-bunch pileup.

The fractions of secondary photons from the different sources are shown in figure 5.11 for the two reconstruction methods. It can be seen, that secondary photons contribute more distinctly to the calorimeter measurement. This can be attributed to the larger

radii at which the EMCal is situated as well as the additional suppression due to the conversion probability in the conversion method. The fractions are rather flat for the reconstruction with the calorimeter while they fall steeply in the case of the conversion measurement. It can be deduced, that the contribution from secondary photons is more significant for the calorimeter measurement over the full range in transverse momentum. Furthermore, secondary photons from K_L^0 decays play a, although subordinate, role in the case of the calorimeter measurement while they are negligible for the conversion method. Secondary photons from material interactions are combined under the label 'rest' and are the second largest contributor in both measurements at low transverse momenta.

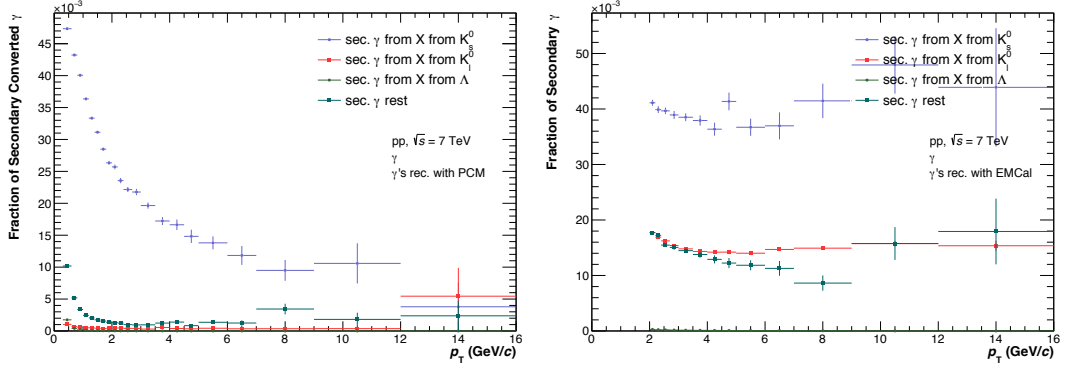


Figure 5.11.: Fractions of secondary photons to the measured photon spectrum for the conversion (left) and calorimeter (right) measurement.

5.3.3. Photon Purity

The purity is defined as the percentage of real photons in the identified sample after the subtraction of secondaries and hence a measure for the contamination from misidentified background. Naturally, the purity heavily depends on the measurement method as well as the selection criteria that are applied on the initial sample, with different sources of background being crucial for the two methods that are presented. In both cases the selection cuts for photons were optimized in such a way that the purity is maximized while maintaining a reasonable reconstruction efficiency. However, a full exclusion of background is impossible without dramatically reducing the statistics.

After the selection cuts were applied on the initial V0 sample, the main sources of background in the conversion measurement are random combinations of tracks that are paired into V0s but do not originate from a common mother particle. The topology of these combinatorial pairs is similar to that of a photon conversion since they have passed all selection cuts. Typically, the most dominant background combinations in the V0 sample are random pairs of electrons and positrons, pairs of electrons and pions and pion pairs, depending on the transverse momentum. Additional, but subordinate, contributions are pairs of heavier particles. Further contamination can come from particle decays that are misidentified as photon conversions due to a misidentification of the decay products but this is reliably removed by the cut on the Armenteros-Podolanski

plot, shown in figure 5.4.

The background in the calorimeter photon sample is of different nature than in the case of the conversion measurement. While the main source of non-photon background in the conversion measurement are combinatorial V0s, the same is not possible in the calorimeter measurement because single clusters are identified with measured photons. Therefore, the contamination of the photon sample is given by misidentified clusters, that actually were not produced by a photon. Clusters of charged particles are removed by the track matching cut. However this can only be done if a track was found in the inner detector and the extrapolation of the track to the surface of the EMCal was possible. Thus, some charged particle can pass the photon identification cuts and be misidentified as a photon, they have to be corrected for later on. Background contributions can also arise from neutral particles whose showers in the calorimeter pass the identification cuts. In this case no exclusion using track matching is possible. The dominant source of background in the calorimeter measurement are misidentified clusters from neutrons and K_L^0 .

Figure 5.12 shows the ratio of identified background sources over real primary photons from MC simulations for both measurement methods. It can be seen, that the conversion method yields a smaller contamination at lower transverse momenta while the reconstruction using the EMCal shows slightly less contamination at higher transverse momenta.

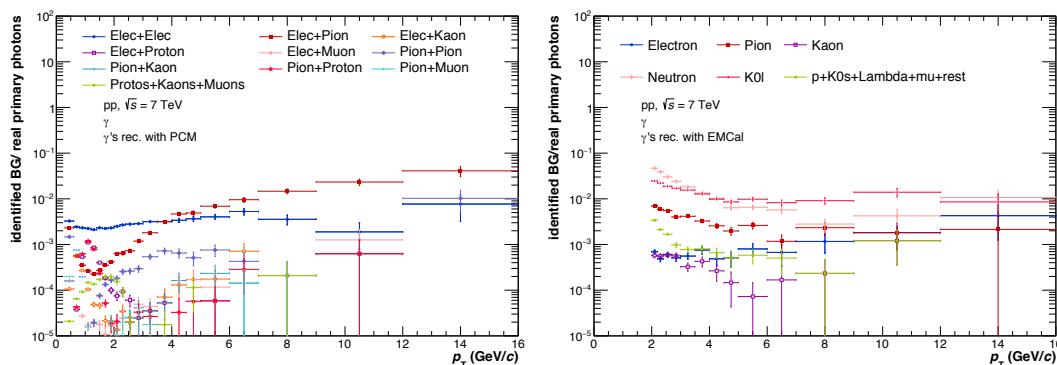


Figure 5.12.: Ratio of identified background sources to real primary photons from MC for the conversion (left) and calorimeter (right) method.

In principle, there are already methods being explored and used to determine the purity of the photon sample with a data driven approach, but in this analysis MC information is used nevertheless. The use of a data driven approach, although being interesting in its own right since it provides a good test for the simulations, is not as crucial in proton-proton collisions because the particle spectra are fairly well reproduced by the simulations. After the secondary photons are subtracted from the reconstructed sample, the purity must be defined on the sample of primary photons and is determined for both methods as:

$$P_{\gamma, \text{prim.}}(p_T) = \frac{\gamma_{\text{rec., prim.}}^{\text{MC, true}}(p_T)}{\gamma_{\text{rec.}}^{\text{MC, all}}(p_T) - \gamma_{\text{rec., sec.}}^{\text{MC, true}}(p_T)}, \quad (5.13)$$

where all spectra are reconstructed in the simulated detector, hence the label 'rec.'. The label 'true' refers to the photons being validated primary or secondary photons, respectively. The subtraction in the denominator leaves the simulated and reconstructed primary spectrum including contribution from background. Equation 5.13 is used for both measurement methods with the different reconstruction methods used accordingly.

The purities that are determined for both methods are shown in figure 5.13 and confirm the conclusions that can be drawn from figure 5.12. The conversion measurement provides a higher purity of the photon sample over a large part of the transverse momentum range but falls to large p_T . This can be attributed to the more sophisticated selection criteria that are used, with the discrimination between signal and background becoming increasingly difficult at larger transverse momenta. In contrast, the purity in the calorimeter shows a steep rise at low p_T and drops slightly to larger momenta due to the increasing probability for the merging of showers in the calorimeter.

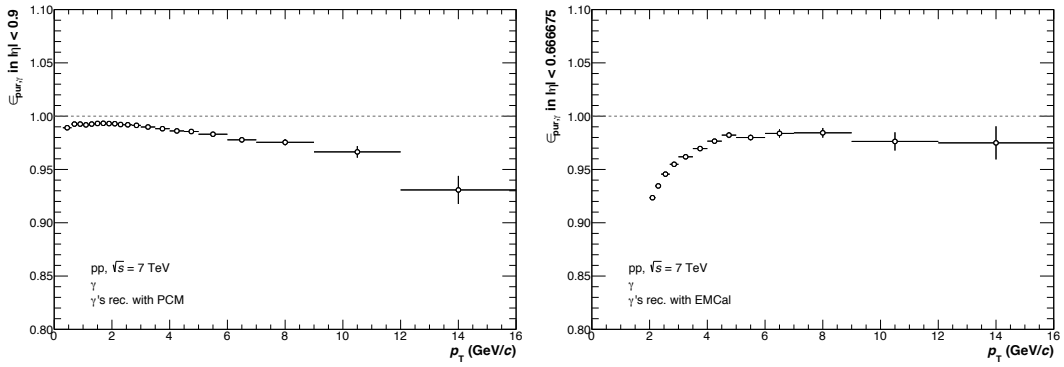


Figure 5.13.: Photon purity for the conversion (left) and calorimeter (right) measurement.

5.3.4. Reconstruction Efficiency

The reconstruction efficiency relates the measured photon spectrum to the transverse momentum distribution that is produced by nature in the collision. Two effects have to be considered, that are a non-perfect finding efficiency for the converted photons and the photons measured with the calorimeter as well as a difference between the measured and the true transverse momentum of the photons. Differences in p_T can arise from energy loss of the conversion electrons and positrons via bremsstrahlung and resolution effects. Therefore, two steps have to be taken to correct for the reconstruction efficiency: firstly, the measured spectra have to be transformed from the reconstructed to the real transverse momenta of the photons, which is done using Bayesian unfolding with the detector response. Secondly, the spectra are corrected for the reconstruction efficiency. Both, the reconstruction efficiency as well as the detector response, depend on the method that is used for the reconstruction and are evaluated for each method individually.

The basic idea of unfolding is to invert the detector response to obtain the true transverse momentum from the reconstructed one. This process can be sketched as

finding the solution to

$$p_T^{\text{rec.}} = A(p_T^{\text{rec.}}, p_T^{\text{true}}) \cdot p_T^{\text{true}}, \quad (5.14)$$

where $A(p_T^{\text{rec.}}, p_T^{\text{true}})$ is given by the detector response matrix that is obtained from Monte Carlo and relates both scales of transverse momentum. The response matrices for both photon reconstruction methods are shown in figure 5.14 and reveal different relations between the two p_T scales, depending on the method. The energy loss through bremsstrahlung of the conversion pair can be seen in the response matrix for the conversion measurement, figure 5.14 left, as an excess at low p_T^{true} compared to the reconstructed value. Due to the energy loss of the conversion pair, it is more likely to reconstruct a photon at a lower transverse momentum than it was generated. In contrast, the detector response for the calorimeter measurement rather shows a broadening from the diagonal that can be attributed to the reduced resolution of the calorimeter at lower energies as well as conversions and overlapping showers.

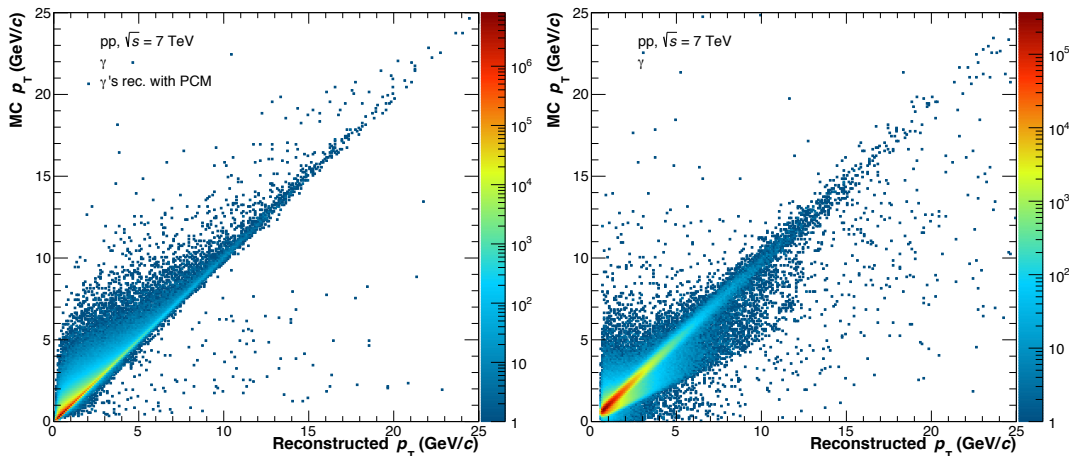


Figure 5.14.: Detector response matrices from MC for the conversion (left) and calorimeter (right) measurement, with 'MC p_T ' referring to the real transverse momentum.

The unfolding is performed with the RooUnfold package [51, 52], that can be used as an extension to ROOT. Instead of directly inverting the response matrix to solve equation 5.14, which would be very sensitive to statistical fluctuations, a Bayesian approach is used. The detector response is unfolded iteratively to obtain the true transverse momentum. In this approach, a prior is required to calculate the conditional probabilities following the Bayesian theorem. The first iteration uses the distribution of the true p_T from Monte Carlo and each subsequent iteration uses the result of the previous one as a prior. It is therefore crucial to optimize the number of iterations to prevent a bias of the unfolded spectrum.

After the unfolding, the spectrum is given as a function of the real transverse momentum p_T^{true} . This has to be considered in the calculation of the reconstruction efficiency

that is given by:

$$\epsilon_{\gamma, \text{conv.}}(p_T^{\text{true}}) = \frac{\gamma_{\text{rec., prim.}}^{\text{MC, true}}(p_T^{\text{true}})}{\gamma_{\text{prim.}}^{\text{MC, conv.}}(p_T^{\text{true}})}, \quad (5.15)$$

for the conversion measurement. Hereby, the reconstructed and validated primary photon spectrum from MC is divided by all converted photons in the simulation. The definition is chosen such, since the conversion probability of the photons in the detector material is included as an individual correction. In the case of the calorimeter measurement, the reconstruction efficiency is modified to include the correction for the geometric acceptance of the calorimeter. Furthermore, the reconstruction efficiency of the calorimeter is not restricted to converted photons and can be expressed as:

$$\epsilon_{\gamma, \text{calo.}}(p_T^{\text{true}}) = \frac{\gamma_{\text{rec., prim.}}^{\text{MC, true}}(p_T^{\text{true}})}{\gamma_{\text{prim.}}^{\text{MC}}(p_T^{\text{true}})}. \quad (5.16)$$

The use of all photons from MC ensures the incorporation of the acceptance in the reconstruction efficiency.

The reconstruction efficiencies for both methods are shown in figure 5.15 as a function of the true transverse momentum that is obtained from the unfolding procedure. In comparison to the conversion measurement, the reconstruction efficiency for the calorimeter method is additionally suppressed due to the acceptance that is included. It can be seen, that the reconstruction efficiency for the calorimeter measurement is rather flat while the reconstruction efficiency for the conversion method rises at low transverse momenta and then falls off after a maximum at $p_T \sim 2 \text{ GeV}/c$. This particular shape originates in the selection cuts that are applied on the V0 candidates, whereas the cluster selection is less constrained.

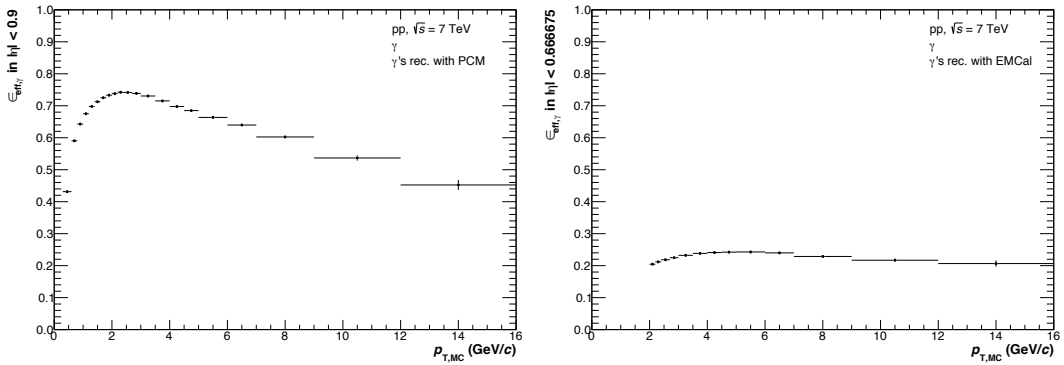


Figure 5.15.: Reconstruction efficiencies of the conversion (left) and calorimeter (right) method, with the reconstruction efficiency for the calorimeter measurement including the acceptance.

5.3.5. Photon Conversion Probability

In contrast to the measurement using the calorimeter, the conversion method is subject to the probability that a photon is converted into an electron positron pair in the detector. This process can not happen in the vacuum but needs an interaction with the material to conserve the momenta of the particles involved. In the high energy limit, the cross section of pair production flattens out and shows no energy dependence anymore. The conversion probability is then determined by the material that is traversed and specifically depends on its radiation length, which is the characteristic distance in the material that has to be travelled for one interaction. Figure 5.16 shows the radial distribution of reconstructed photon conversions in data compared to the distribution in MC. It can be seen, that the majority of photon conversions happen in the beam pipe and SPD layers of the ITS as well as the TPC inner field cage. Additional important sources of photon conversions are the remaining ITS layers and the inner containment vessel of the TPC. The TPC drift gas provides only a small contribution to the total number of photon conversions.

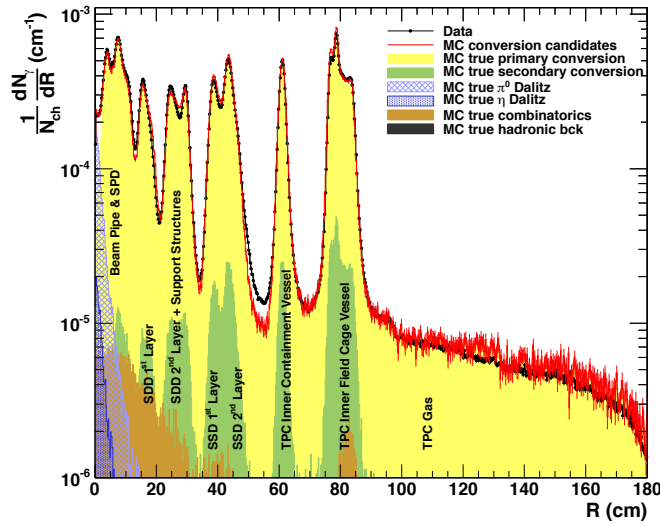


Figure 5.16.: Radial distribution of reconstructed photon conversions in data compared to MC. [43]

The energy of the photons that are measured is already high enough for the conversion probability to be mainly determined by the fiducial spatial region of the detector that is chosen for the analysis and therefore defines the amount of material that is traversed. The probability itself can not be accessed in data and has to be evaluated using MC simulations. It does, however, not depend on the detector response and is therefore calculated as a function of the true transverse momentum of the photon:

$$C_{\gamma}(p_T^{\text{true}}) = \frac{\gamma_{\text{prim.}}^{\text{MC, conv.}}(p_T^{\text{true}})}{\gamma_{\text{prim.}}^{\text{MC, all}}(p_T^{\text{true}})}, \quad (5.17)$$

where the number of the converted photons in the fiducial region is divided by the

number of all photons in said spatial region. The conversion probability is shown in figure 5.17 and levels out to about 9%, with the dashed line showing a constant fit above $p_T = 2 \text{ GeV}/c$. At larger transverse momenta the probability is constant whereas a drop is visible towards vanishing p_T . This is due to the increasing importance of Compton scattering at lower photon energies.

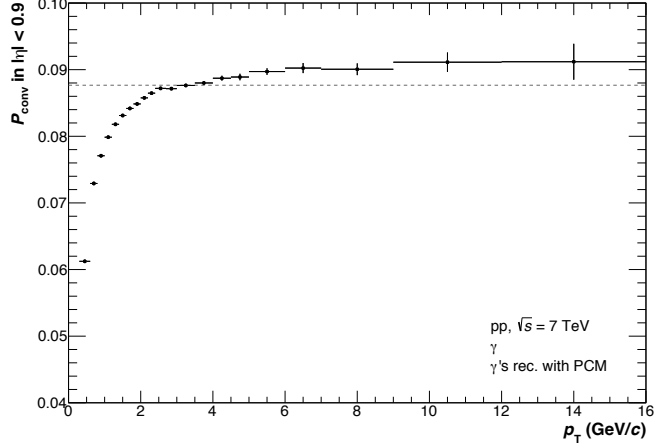


Figure 5.17.: Photon conversion probability inside the ALICE detector within the fiducial region of $|\eta| < 0.9$. The dashed line shows a constant fit to the conversion probability above $p_T = 2 \text{ GeV}/c$.

5.4. Inclusive Photon Spectrum

The fully corrected primary inclusive photon spectrum is obtained from the raw measured spectrum by applying all corrections that were described previously according to the method of the measurement. In the case of the conversion measurement, the out-of-bunch pileup correction is applied first since it is defined on the reconstructed photon sample. Then, for both reconstruction methods, the secondary photon contribution is subtracted and the resulting spectra are named $\gamma_{\text{sec.}+\text{pileup corr.}}^{\text{data}}(p_T)$ and $\gamma_{\text{sec. corr.}}^{\text{data}}(p_T)$, respectively. The resulting spectra are then multiplied with the primary photon purity to remove the contaminations. At this stage, the spectrum is still a function of the measured transverse momentum because the unfolding procedure was not applied yet. The spectra are then corrected for the detector response and the reconstruction efficiency with the use of unfolding, transforming the spectra in a function of the true transverse momenta. As a last step for the conversion measurement, the corrected spectrum is divided by the conversion probability to regain the spectrum of primary photons that were produced in the collision. The full correction formulae can be written as:

$$\gamma_{\text{full corr.}}^{\text{data,prim.}}(p_T) = \gamma_{\text{sec.}+\text{pileup corr.}}^{\text{data}}(p_T) \times P_{\gamma,\text{prim.}}(p_T) \times \frac{1}{\epsilon_{\gamma}(p_T)} \times \frac{1}{C_{\gamma}(p_T)}, \quad (5.18)$$

in the case of the conversion measurement and

$$\gamma_{\text{full corr.}}^{\text{data,prim.}}(p_{\text{T}}) = \gamma_{\text{sec. corr.}}^{\text{data}}(p_{\text{T}}) \times P_{\gamma,\text{prim.}}(p_{\text{T}}) \times \frac{1}{\epsilon_{\gamma}(p_{\text{T}})} \quad (5.19)$$

for the photons reconstructed in the calorimeter. In both cases the respective correction factors are used and unique subscripts on these factors are omitted for a more comprehensive depiction of the equations. The fully corrected spectrum is a function of the true transverse momentum instead of the reconstructed one due to the unfolding procedure that was applied.

The fully corrected spectra of both measurement methods now describe the transverse momentum dependence of all primary photons that were produced in the fiducial region of $|\eta| < 0.9$ and 2π in azimuth. Despite the smaller acceptance this also holds for the calorimeter measurement due to the correction for the acceptance that is included in the reconstruction efficiency for this method. The invariant yields can then be calculated with:

$$E \frac{d^3 N_{\gamma}}{dp^3} = E \frac{d^3 N_{\gamma}}{p_{\text{T}} dp_{\text{T}} dy d\phi} = \frac{1}{N_{\text{event}}} \frac{1}{2\pi p_{\text{T}}} \frac{\gamma_{\text{full corr.}}^{\text{data,prim.}}(p_{\text{T}})}{\Delta y \Delta p_{\text{T}}}. \quad (5.20)$$

The invariant yield is normalized to the number of events for the respective reconstruction method, listed in table 4.1, and given per unit rapidity as well as differential in p_{T} . It is worth mentioning, that for the massless photon the two quantities rapidity and pseudorapidity are identical. The inclusive primary invariant yields of both measurement methods are shown in figure 5.18. The conversion measurement allows for a transverse momentum range of $0.3 \text{ GeV}/c \leq p_{\text{T}} \leq 16.0 \text{ GeV}/c$ while the reconstruction with the calorimeter is restricted to $1.6 \text{ GeV}/c \leq p_{\text{T}} \leq 16.0 \text{ GeV}/c$, due to the neutral pion measurement that is required for the photon double ratio. Furthermore, the purity of the calorimeter measurement falls steeply to low transverse momenta, thus it would not be beneficial to measure to lower p_{T} . Figure 5.18 also shows the systematic uncertainties that were determined on the invariant photon yield for the conversion measurement. The calculation of the systematic uncertainties is described in section 8.2. The systematic uncertainties for the calorimeter measurement were not determined yet as further studies are required for a better understanding of the measurement using the EMCal.

In the bottom panel of figure 5.18, the spectra obtained with the two reconstruction methods are compared. It can be seen, that they agree up to 5% within their statistical uncertainty. The agreement diminishes towards lower transverse momenta where the resolution of the calorimeter method gets worse. At intermediate p_{T} , the calorimeter method slightly underestimates the spectrum that is obtained from the conversion method.

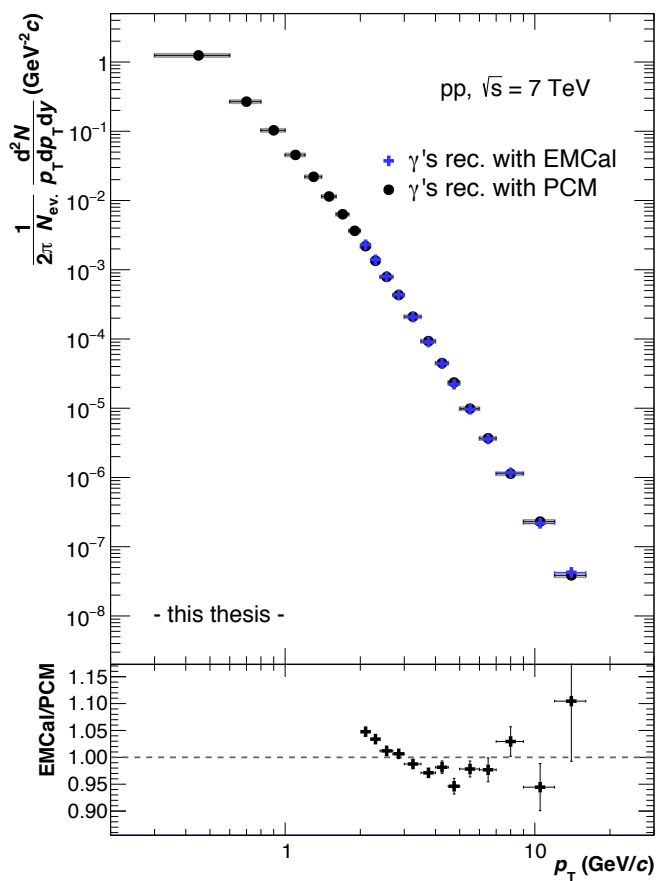


Figure 5.18.: Invariant inclusive primary photon yields reconstructed with the conversion and calorimeter method. Additionally, the systematic uncertainties of the conversion measurement are shown.

6. Neutral Pion Reconstruction

The reconstruction of neutral pions is essential for the measurement of direct photons using the photon double ratio introduced in equation 2.9. Hereby, the neutral pions are reconstructed from the two photon decay channel in order to partially cancel systematic uncertainties in the double ratio. Therefore, the two distinct methods that are used for the photon measurement must also be used for the reconstruction of the respective neutral pion spectra. The neutral pion analyses were carried out in parallel by two different analyzers and are presented in [53, 54] for the conversion measurement, and [55] for the measurement using the EMCal. In this analysis, the reconstruction of the neutral pion spectrum with the conversion method is identical to the respective reference, with the same selection cuts applied. In the case of the calorimeter measurement, the photon selection differs slightly from the selection used in the reference. This is attributed to the greater significance of the photon purity in the direct photon measurement compared to the neutral pion reconstruction, where the invariant mass analysis and the background estimation allows for a less strict selection of photon candidates. This, in turn, affects the calorimeter measurement more significantly due to the different selection of photon candidates compared to the conversion method. The photon selection criteria used for the conversion method were found to provide an optimized purity of the photon sample while maintaining a good neutral pion reconstruction efficiency. The reconstruction of the neutral pions is part of the same framework that is used for the photon measurement and is thus performed based on the photon selections presented in 5. Nevertheless, this analysis heavily benefits from the detailed studies of the neutral pions presented in the respective references.

The reconstruction of neutral pions is described briefly with a focus on the main aspects. As for the photon reconstruction presented in section 5, specifics of both reconstruction methods will be addressed since the two spectra have to be used accordingly in the calculation of the direct photon excess ratio.

6.1. Reconstruction and Signal Extraction

The neutral pions are reconstructed from the decay into two photons for either method. Hereby the sample of photons is initially identical to the one used for the measurement of the inclusive photon yield and neutral pion candidates are obtained by pairing photons event-wise within their respective sample. In the conversion method, neutral pions are combined from the V0 sample that was obtained after the selections described in section 5.1 while the EMCal measurement is based on the clusters selected according to the description in section 5.2. Neutral pions are identified by reconstructing their invariant mass $m_{\gamma\gamma}$.

However, before this is done, two additional criteria are used to select the photon pairs for the reconstruction. The rapidity region in which neutral pions are reconstructed is

further reduced, compared to the photon measurement, in order to reduce the possible loss of π^0 candidates due to a large opening angle of the photon pair. The asymmetry of the neutral pion decay,

$$\alpha_{\pi^0} = \frac{|E_{\gamma_1} - E_{\gamma_2}|}{E_{\gamma_1} + E_{\gamma_2}}, \quad (6.1)$$

can also be used to remove combinatorial pairs. This is more crucial in a high multiplicity environment where random combinations with low p_T photons are more likely and would increase the population of large α_{π^0} . In the case of the minimum bias proton-proton collisions that are examined, the multiplicity is significantly lower and this cut is essentially left open. Nevertheless, a possible effect of this cut on the invariant yield is studied in the determination of the systematic uncertainty.

After the selection according to the neutral pion candidate rapidity and asymmetry, the invariant masses of the photon pairs are calculated according to:

$$m_{\gamma\gamma} = \sqrt{2E_{\gamma_1}E_{\gamma_2}(1 - \cos\theta_{12})}, \quad (6.2)$$

where the photon energies are given by $E_{\gamma_{1,2}}$ and θ_{12} is the opening angle of the photon pair. The opening angle is given by the opening angle of the V0 pair for the conversion measurement and calculated with respect to the primary vertex for the calorimeter method. In the case of the calorimeter measurement, a minimal opening angle of $\theta_{12} > 0.02$ is requested, that corresponds to the diameter of one EMCal cell and therefore discards false combinations. For photons that originate from the same neutral pion, an invariant mass close to the π^0 rest mass of $0.135 \text{ GeV}/c^2$ will be obtained, with the mean deviation from the literature value corresponding to the resolution of the measurement.

Despite the reconstruction via the invariant mass of the pair, combinatorial background can not be recognized on the basis of single photon pairs. Furthermore, combinatorial pairs of photons can result in an invariant mass close to the rest mass of the neutral pion although they do not originate from a (common) π^0 decay. This background has to be estimated on a statistical basis, which is done by using an event mixing technique. Hereby, photons from the current event are paired with photons from different events resulting in a sample of purely combinatorial pairs since no correlations between the events exist. Many events are used in the combination to get a high statistic sample of combinatorial pairs. The invariant mass distributions before and after the subtraction of combinatorial background are shown in figure 6.1 for both methods in one exemplary p_T bin. Additionally, the combinatorial background from event mixing as well as a fit of the signal according to equation 6.3 is shown. It can be seen, that the signal peak obtained with the conversion method is narrower than the signal peak from the calorimeter reconstruction, which can be attributed to the superior momentum resolution of the TPC. Due to the optimized selection criteria, the magnitude of combinatorial background under the peak is comparably small in both cases. The neutral pion invariant mass distributions are shown in all transverse momentum bins for both reconstruction methods in appendix A.2.

The neutral pion signal is extracted from the invariant mass distributions in transverse momentum bins. The combinatorial background is normalized to the background

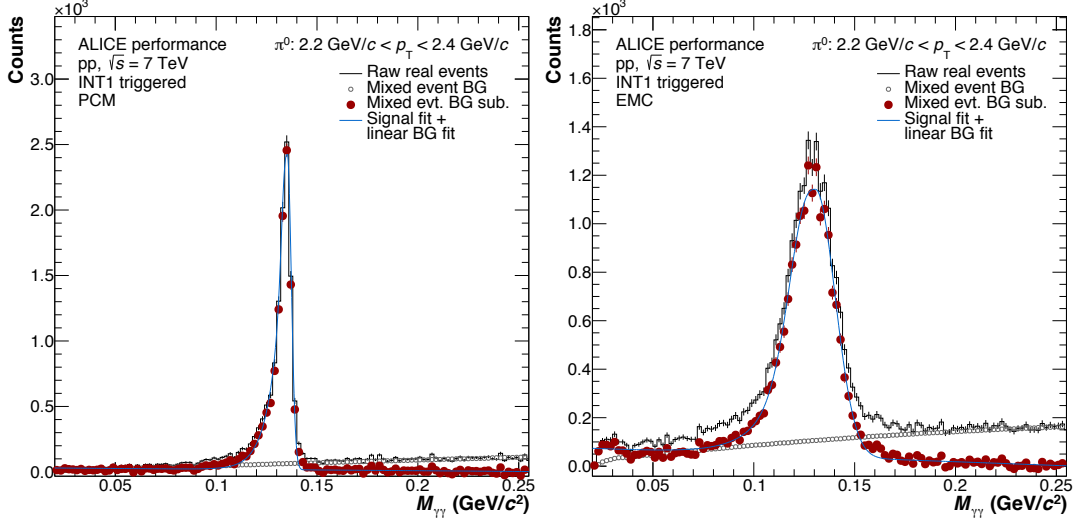


Figure 6.1.: Invariant mass distribution of photon pairs reconstructed with the conversion (left) and calorimeter (right) method in $2.2 \text{ GeV}/c < p_T < 2.4 \text{ GeV}/c$.

of the invariant mass distributions by scaling to the high-mass end of the distribution. After the subtraction, shown in figure 6.1, some residual background can remain under the peak. Furthermore, it can be seen that the peak is stronger tailed to the left side due to electron energy loss via bremsstrahlung, which is naturally more expressed in the case of the conversion measurement. In the case of the calorimeter measurement, the low-mass tail of the peak is due to the reconstruction of photons in the calorimeter that converted prior to reaching it. The invariant mass peaks are then fitted to extract the mass position, using:

$$y = A \left(G(m_{\gamma\gamma}) + E(m_{\gamma\gamma}, \lambda) (1 - G(m_{\gamma\gamma})) \Theta(m_{\pi^0} - m_{\gamma\gamma}) \right) + B + C m_{\gamma\gamma}, \quad (6.3)$$

$$\text{with } G(m_{\gamma\gamma}) = \exp \left[-0.5 \left(\frac{m_{\gamma\gamma} - m_{\pi^0}}{\sigma_{m_{\gamma\gamma}}} \right)^2 \right] \quad (6.4)$$

$$\text{and } E(m_{\gamma\gamma}, \lambda) = \exp \left(\frac{m_{\gamma\gamma} - m_{\pi^0}}{\lambda} \right). \quad (6.5)$$

Hereby, the signal peak is described with a modified Gaussian distribution to account for the residual background and the low-mass tail. The Gaussian distribution $G(m_{\gamma\gamma})$, situated at the pion mass m_{π^0} with width $\sigma_{m_{\gamma\gamma}}$, is modified with an exponential function $E(m_{\gamma\gamma}, \lambda)$, with inverse slope λ , to account for the bremsstrahlung tail. The Heaviside function $\Theta(m_{\pi^0} - m_{\gamma\gamma})$ ensures the contribution solely at the low-mass end of the peak for $m_{\gamma\gamma} < m_{\pi^0}$. Possible residual background is covered by a linear contribution to the fit: $B + C m_{\gamma\gamma}$. The signal fits after the subtraction of combinatorial background are shown in figure 6.1.

The raw π^0 yields are extracted from bin counting under the signal peak in the invariant mass distributions after the subtraction of the combinatorial background.

Neutral pion selection		
	conversion method	calorimeter method
fiducial rapidity y	$ y < 0.8$	-
max. asym. α_{π^0}	$\alpha_{\pi^0} < 1.0$	$\alpha_{\pi^0} < 1.0$
min. opening angle θ_{12}	-	$\theta_{12} > 0.02$
comb. background	event mixing	event mixing
	$N_{\text{BG events}} = 50$	$N_{\text{BG events}} = 80$
inv. mass range $m_{\gamma\gamma}$	$m_{\pi^0} - 0.035 \text{ GeV}/c^2 \leq m_{\gamma\gamma} \leq m_{\pi^0} + 0.010 \text{ GeV}/c^2$	$m_{\pi^0} - 0.032 \text{ GeV}/c^2 \leq m_{\gamma\gamma} \leq m_{\pi^0} + 0.022 \text{ GeV}/c^2$

Table 6.1.: Summary of neutral pion selection criteria.

Hereby, the ranges, listed in table 6.1, are chosen dynamically around the peak positions that are obtained in the fitting procedure. Hereby, the range is chosen wider for the calorimeter measurement to account for the broader peak. The linear contribution from residual background is subtracted additionally, if residual background was identified in the distributions.

The neutral pion selection criteria, after the photon selection was applied, are summarized in table 6.1 for the two measurement methods. The invariant mass ranges around the identified peak positions used for the signal extraction are also quoted.

6.2. Corrections to Measured Spectra

The neutral pion raw yields obtained from the signal extraction have to be corrected, like the photons, for secondary contributions, reconstruction efficiency and additionally for the detector acceptance due to the additionally reduced fiducial region of the detector. In the case of the conversion measurement, the neutral pion spectrum also needs to be corrected for out-of-bunch pileup contributions. This is done analogously to the correction that is applied on the photon spectrum measured with the conversion method. The corrections are calculated using MC information and are presented in the following section side-by-side for the two reconstruction methods. Since the background is subtracted using an event mixing technique and possible residual background is accounted for in the signal extraction, no further purity correction has to be applied as it was the case for the photons. The corrections are introduced in the order in which they are applied on the reconstructed spectra.

6.2.1. Out-of-Bunch Pileup Correction

Like for the photons, the correction for out-of-bunch pileup must only be considered for the conversion method and applied directly on the measured spectrum. Again the DCA_z distributions are used to extract the background. The same procedure as for the photons, described in section 5.3.1, is applied on the neutral pion DCA_z distributions in p_T bins and a correction factor is extracted to modify the spectrum accordingly. While only three different categories of V0s had to be considered for the photons, the pions involve six possible combinations of photon categories for the pair. The out-of-bunch

pileup correction procedure for the neutral pions is described in more detail in [53, 54]. Figure 6.2 shows the correction factor for out-of-bunch pileup that is extracted from the DCA_z distributions. The contribution from out-of-bunch pileup to the neutral pion yield is larger than for the photons, with a maximum magnitude of about 10% in the lowest transverse momentum bin.

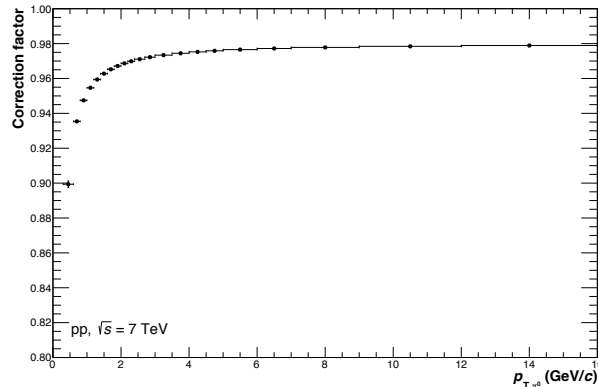


Figure 6.2.: Out-of-bunch pileup correction factor for neutral pions.

6.2.2. Secondary Correction

The largest source of secondary neutral pions is the weak decay $K_S^0 \rightarrow 2\pi^0$, that is also responsible for the largest amount of secondary photons through to the subsequent decays of the neutral pions. Additional contributions arise from the weak decays of K_L^0 , Λ and material interactions. Secondary neutral pions are subtracted from the measured yield, which was already corrected for contributions from pileup in the case of the conversion measurement, to obtain the primary neutral pion spectrum. The secondary spectra are determined from a decay simulation of the measured and parametrized K_S^0 and Λ spectra in the case of the conversion measurement. Residual contributions from material interactions are determined from MC simulations. As it was discussed for the photons in section 5.3.2, the spectra are produced as invariant yields and have to be convoluted with the reconstruction efficiencies and acceptances, which are obtained from MC. However, for the calorimeter method, the reconstruction efficiencies for secondary neutral pions are not perfectly understood yet. Therefore, the secondary spectra are directly taken from MC for the calorimeter measurement. The fractions of secondary pions from the different sources are shown in figure 6.3. The contribution from secondaries is then calculated from the secondary fractions and the measured neutral pion spectra prior to the subtraction. In the case of the conversion measurement, the secondary fractions from the decay simulation are labelled with 'Toy appr.' and compared to the secondary fractions from MC. It can be seen, that the contribution from secondaries is overestimated by the MC simulations. This can be attributed to a non-perfect coincidence between the spectra of the mother particles in data and MC. The secondary fractions for the calorimeter method are parametrized with a power law to reduce the statistical fluctuations for the calculation of the secondary contribution.

As it was observed for the secondary photon fractions, the secondary pion fractions fall less steeply in the case of the calorimeter measurement.

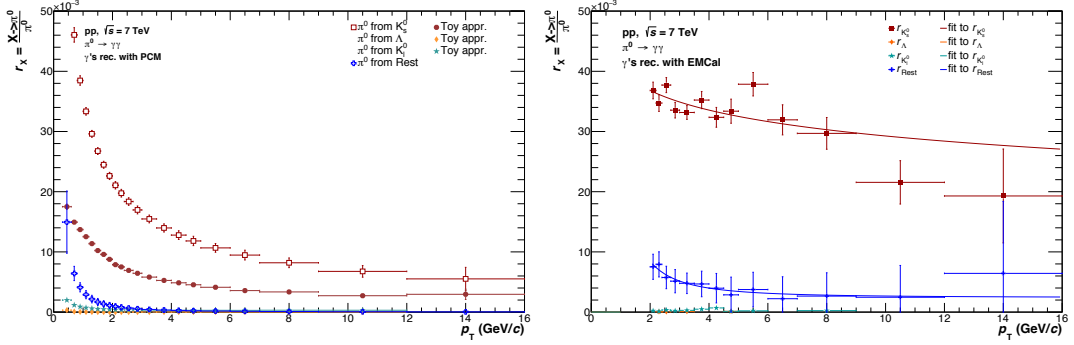


Figure 6.3.: Secondary pion fractions from different mother particles for the conversion (left) and calorimeter (right) method.

6.2.3. Acceptance and Efficiency Correction

After the correction for out-of-bunch pileup and the subtraction of secondary contributions, the spectra have to be corrected for the reconstruction efficiency and the detector acceptance to regain the spectrum that was produced in the collision. In the case of the conversion measurement, the photon conversion probability is included into the efficiency correction. While unfolding was used in the photon measurement to restore the real transverse momentum, the same can not be done for the neutral pions due to the lower statistics of the π^0 sample. Therefore the correction for the transverse momentum resolution is included into the reconstruction efficiency for both reconstruction methods. The reconstruction efficiency for either method is calculated as:

$$\epsilon_{\pi^0}(p_T) = \frac{\pi_{\text{rec., prim.}}^{0\text{MC}}(p_T)}{\pi_{\text{prim., in acc.}}^{0\text{MC}}(p_T^{\text{true}})}, \quad (6.6)$$

where $\pi_{\text{rec., prim.}}^{0\text{MC}}(p_T)$ is the spectrum of primary neutral pions, reconstructed from MC events. In the case of the conversion measurement, this spectrum is obtained from validated neutral pions, while the validation is omitted for the calorimeter measurement. This is divided by the spectrum of generated primary neutral pions within the detector acceptance, $\pi_{\text{prim., in acc.}}^{0\text{MC}}(p_T^{\text{true}})$, that is differential in the transverse momentum the particle were produced at. Hereby, the neutral pions are also corrected for the transverse momentum resolution of the reconstruction. The reconstruction efficiencies for both methods are shown in figure 6.4. The calorimeter methods provides a reconstruction efficiency that is larger in magnitude due to the additional suppression of the reconstruction efficiency for the conversion measurement by the conversion probability. However, the reconstruction efficiency rises slower in the case of the calorimeter measurement.

Furthermore, the reconstructed neutral pions have to be corrected for the geometrical

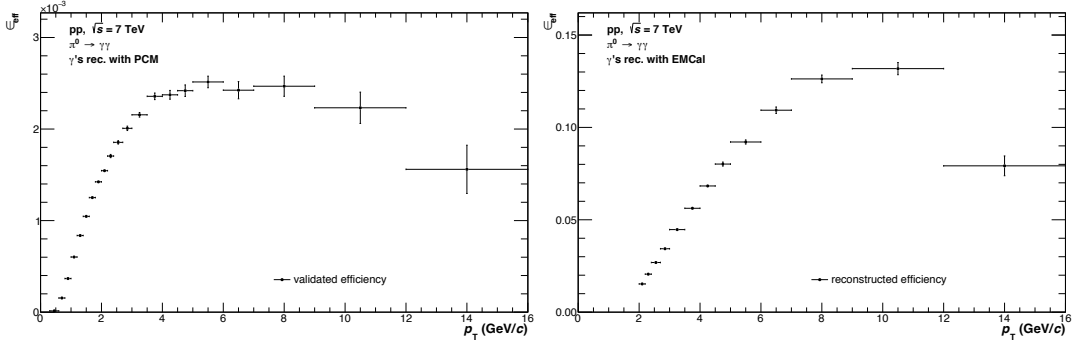


Figure 6.4.: Neutral pion reconstruction efficiency of the conversion (left) and calorimeter (right) method.

acceptance of the respective method. The acceptance is defined as:

$$A_{\pi^0}(p_T) = \frac{\pi_{\text{prim., in acc.}}^{\text{MC}}(p_T^{\text{true}})}{\pi_{\text{prim., all}}^{\text{MC}}(p_T^{\text{true}})}, \quad (6.7)$$

which is based on the generated MC spectra of primary neutral pions. Both spectra are identical up to the diminution that the numerator is taken in the acceptance of the respective reconstruction method. In the case of the conversion measurement, the acceptance is given by the fiducial region of the measurement, $|y| < 0.8$, whereas the geometrical acceptance of the EMCal is used in the case of the calorimeter measurement. The acceptances for both methods are shown in figure 6.5. The acceptance of the conversion measurement takes larger values, approaching unity at high transverse momenta, with a steep rise at low transverse momenta due to the larger opening angle of the photon pair. The calorimeter method provides a rather flat acceptance but at smaller absolute values than the conversion measurement due to the reduced coverage in solid angle.

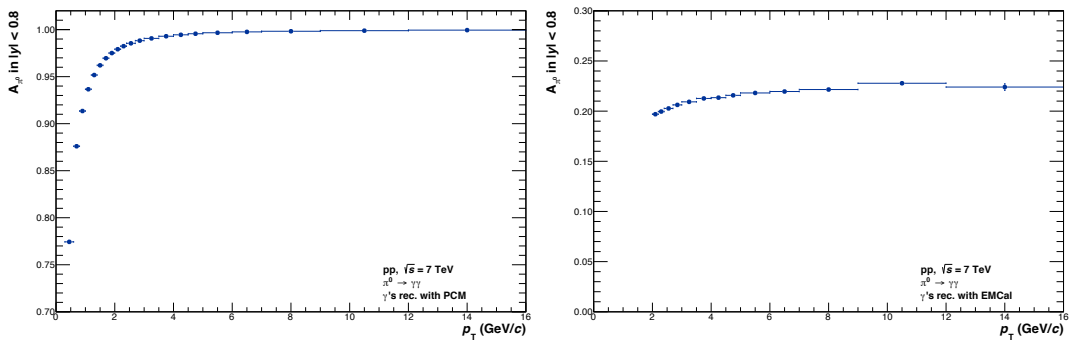


Figure 6.5.: Neutral pion acceptance of the conversion (left) and calorimeter (right) measurement.

6.3. Inclusive Neutral Pion Spectrum

The fully corrected neutral pion spectrum, reconstructed with either method, is calculated according to:

$$\pi_{\text{full corr.}}^{0\text{data,prim.}}(p_{\text{T}}) = \pi_{\text{sec. corr.}}^{0\text{data}}(p_{\text{T}}) \times \frac{1}{\epsilon_{\pi^0}(p_{\text{T}})} \times \frac{1}{A_{\pi^0}(p_{\text{T}})} \times \frac{1}{BR_{\pi^0 \rightarrow \gamma\gamma}}, \quad (6.8)$$

where $\pi_{\text{sec. corr.}}^{0\text{data}}(p_{\text{T}})$ already includes the out-of-bunch pileup correction in the case of the conversion measurement. Since in both cases the neutral pions are reconstructed from the decay into two photons, the branching ratio of $BR_{\pi^0 \rightarrow \gamma\gamma} = 98.823\%$ [50] has to be considered. The invariant yield is calculated from the fully corrected primary neutral pion spectrum according to:

$$E \frac{d^3 N_{\pi^0}}{dp^3} = E \frac{d^3 N_{\pi^0}}{p_{\text{T}} dp_{\text{T}} dy d\phi} = \frac{1}{N_{\text{event}}} \frac{1}{2\pi p_{\text{T}}} \frac{\pi_{\text{full corr.}}^{0\text{data,prim.}}(p_{\text{T}})}{\Delta y \Delta p_{\text{T}}}. \quad (6.9)$$

The invariant yields for both methods are shown in figure 6.6, the transverse momentum ranges of the measurements coincide with those quoted for the photon measurements. The calorimeter measurement starts at higher transverse momenta compared to the conversion measurement due to the limit on the cluster energy that is applied for each photon. Furthermore, the lower end of the transverse momentum range is limited by the reconstruction of the signal from the invariant mass distributions, which requires enough statistics for a reasonable detection of the signal peak. No systematic uncertainties are shown for both reconstruction methods since the systematic uncertainty will be evaluated directly on the photon double ratio. However, the neutral pion spectrum measured with the conversion method and including systematic uncertainties can be found, in a different binning in transverse momentum, in [53, 54]. The spectra are compared in the lower panel of figure 6.6 and the agreement between the two reconstruction methods is found to be slightly worse than for the photon spectra.

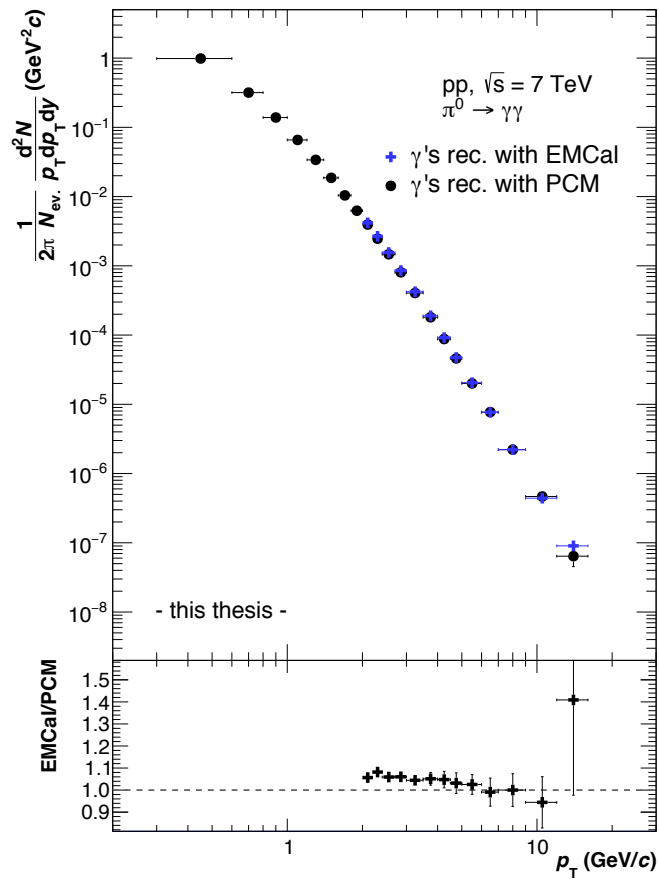


Figure 6.6.: Invariant neutral pion yields, measured with the conversion and calorimeter method.

7. Decay Photon Cocktail

The decay photon spectrum, used in the direct photon excess ratio calculated according to equation 2.9, can not be determined from the data. The decay photons are thus taken from a particle decay simulation, called cocktail simulation due to the vast amount of contributors, that is anchored to measured particle spectra. Many measurements of different particle species are available for the dataset presented, resulting in well understood spectrum of decay photons. The same decay simulation is also used to extract the secondary photon and neutral pion spectra.

In this chapter, the decay simulation is introduced. The input from measured particle spectra, which is used for the generation of the cocktail, is presented first. Then the simulation procedure itself is described in more detail and the chapter is closed with the results of the cocktail simulation as well as a validation of the process.

7.1. Cocktail Input

In the data set of proton-proton collisions at $\sqrt{s} = 7$ TeV, many different particle spectra have been measured. The measured spectra are parametrized using different functional forms and the parametrizations are used as inputs for the generation of the decay photon cocktail. Since photons originate from much more particles than were measured, the missing parametrizations are produced from transverse mass (m_T) scaling of the neutral pion parametrization in the case of mesons and the proton parametrization in the case of baryons. Transverse mass scaling is a phenomenon that was first observed by the WA80 collaboration [56] and describes the similarity of the spectra of different particle species, up to a constant factor, when expressed in terms of the transverse mass

$$m_T = \sqrt{p_T^2 + m^2}, \quad (7.1)$$

where m is the mass of the particle. The spectrum of a particle of species X can then be calculated from the spectrum of the neutral pion or proton if the particle is a meson or a baryon, respectively:

$$E \frac{d^3 N^X}{dp^3} = C_{m_T} \cdot P_{\pi^0/p}(m_T), \quad (7.2)$$

where C_{m_T} is an overall scaling factor and $P_{\pi^0/p}$ is the parametrization of the neutral pion or proton spectrum, expressed in terms of the transverse mass of the particle of species X . The scaling factor C_{m_T} describes the constant ratio of the particle spectrum to the neutral pion or proton spectrum at high transverse momenta and has to be taken from a measurement. The factor is set to one if no measured value or better suited estimate is available.

All mother particles included in the decay simulation are listed in table 7.1. For particles where a measurement is available and used for the parametrization, the reference to the corresponding measurement is given. The K_L^0 spectrum is expected to be identical to the K_S^0 spectrum, therefore the same parametrization, anchored to the measured K_S^0 , is used. The parametrizations of the remaining particles are produced from m_T scaling and the scaling factors are listed, with the scaling factor set to one if no estimate is available. The scaling factors for the η' and the Σ^0 are obtained from PYTHIA 6.4. Furthermore, the decay channels that are included into the decay simulation as well as the respective branching ratios are summarized. Hereby, the branching ratios are taken from the PDG [50] and only decays with a branching ratio above 10^{-6} are included. The branching ratios are normalized, such that the sum of all considered branching ratios is one, while maintaining the relative proportions. Since the secondary photon and neutral pion spectra from sections 5.3.2 and 6.2.2 are also taken from the same decay simulation, the branching ratios for the respective decays of K_S^0 , K_L^0 and Λ are also listed in the table.

The neutral pion and eta measurement are also available from other reconstruction methods, but the spectra from the conversion measurement presented in [53, 54] are used. These provide the best description of the decay photon spectrum in the case of the conversion measurement as well as a minimized systematic uncertainty. Due to time constraints on the computation of the decay simulation, the same cocktail is also used for the calorimeter measurement.

While the proton is not included as a possible source for decay photons or secondaries, it is still parametrized since it is used as base for the transverse momentum scaling of the baryons that are not measured, namely Δ^0 , Δ^+ and Σ^0 . The measurement of the proton is described in [57].

The measured particle spectra are parametrized in order to generate the mother particles in the decay simulation according to the data. The functional forms of the parametrizations were chosen such, that they provide an optimal fit to the measured spectra and therefore do not necessarily have any relation to a physical model.

The neutral pion spectrum was found to be described best with a modified Hagedorn parametrization that was proposed by the PHENIX collaboration [61]. The parametrization is in general used to describe particle spectra that are modified in heavy ion collisions due to effects like radial flow. However, no medium properties are expected in proton-proton collisions and therefore no physical conclusion should be drawn from the functional form of the parametrization. The parametrization can be written as:

$$E \frac{d^3 N}{dp^3} = A \cdot \left(\exp(ap_T + bp_T^2) + \frac{p_T}{p_0} \right)^{-n}. \quad (7.3)$$

The parametrization was also found to be able to optimally describe the measured K_S^0 , Λ and proton spectra when multiplied with the transverse momentum, increasing the tail at high p_T .

The measured η spectrum is described best by a Tsallis function [62], which is often

particle	mass (MeV)	C_{m_T}	measurement	decay	branching ratio
π^0	134.98	-	[53, 54]	$\gamma\gamma$	9.882×10^{-01}
				$e^+e^-\gamma$	1.174×10^{-02}
η	547.85	-	[53, 54]	$\gamma\gamma$	3.941×10^{-01}
				$\pi^0\gamma\gamma$	2.560×10^{-04}
				$\pi^+\pi^-\gamma$	4.220×10^{-02}
				$e^+e^-\gamma$	6.899×10^{-03}
				$\mu^+\mu^-\gamma$	3.090×10^{-04}
η'	957.66	0.40	-	$\rho^0\gamma$	2.908×10^{-01}
				$\omega\gamma$	2.746×10^{-02}
				$\gamma\gamma$	2.198×10^{-02}
				$\mu^+\mu^-\gamma$	1.080×10^{-04}
ω	782.65	-	[58]	$\pi^0\gamma$	8.350×10^{-02}
				$\eta\gamma$	4.600×10^{-04}
				$\pi^0\pi^0\gamma$	7.000×10^{-05}
ρ^0	775.49	1.00	-	$\pi^+\pi^-\gamma$	9.900×10^{-03}
				$\pi^0\gamma$	6.000×10^{-04}
				$\eta\gamma$	3.000×10^{-04}
				$\pi^0\pi^0\gamma$	4.500×10^{-05}
ρ^+	775.49	1.00	-	$\pi^+\gamma$	4.500×10^{-04}
ρ^-	775.49	1.00	-	$\pi^-\gamma$	4.500×10^{-04}
ϕ	1019.46	-	[59]	$\eta\gamma$	1.310×10^{-02}
				$\pi^0\gamma$	1.273×10^{-03}
				$\pi^+\pi^-\gamma$	4.100×10^{-05}
				$\pi^0\pi^0\gamma$	1.130×10^{-04}
				$\pi^0\eta\gamma$	7.300×10^{-05}
				$\eta'\gamma$	6.300×10^{-05}
Δ^0	1232.00	1.00	-	$n\gamma$	6.000×10^{-03}
				$p\gamma$	6.000×10^{-03}
Δ^+	1232.00	1.00	-	$p\gamma$	6.000×10^{-03}
Σ^0	1192.64	0.49	-	$\Lambda\gamma$	$1.000 \times 10^{+00}$
K_S^0	497.61	-	[60]	$\pi^+\pi^-\gamma$	1.787×10^{-03}
				$\pi^0\pi^0$	3.065×10^{-01}
K_L^0	497.61	-	[60]	$\pi^\pm e^\mp \nu\gamma$	3.988×10^{-03}
				$\pi^\pm \mu^\mp \nu\gamma$	4.920×10^{-04}
				$\pi^+\pi^-\gamma$	4.200×10^{-05}
				$\gamma\gamma$	5.500×10^{-04}
				$\pi^0\pi^0\pi^0$	1.946×10^{-01}
				$\pi^+\pi^-\pi^0$	1.250×10^{-01}
Λ	1115.68	-	[60]	$\pi^0\pi^0$	8.630×10^{-04}
				$n\gamma$	8.400×10^{-04}
				$n\pi^0$	3.580×10^{-01}

Table 7.1.: Mother particles included in decay simulation.

used to parametrize particle spectra in proton-proton collisions and can be written as:

$$\frac{d^2N}{dydp_T} = \frac{dN}{dy} \cdot p_T \cdot \frac{(n-1)(n-2)}{nT(nT+m(n-2))} \left(1 + \frac{m_T - m}{nT}\right)^{-n}. \quad (7.4)$$

The Hagedorn parametrization in an unmodified form was found to provide an optimized fit to the measured ω spectrum. The parametrization can be expressed as:

$$E \frac{d^3N}{dp^3} = A \cdot \left(\frac{a}{a+p_T}\right)^{-n}. \quad (7.5)$$

In the case of the ϕ , no functional form was found that satisfyingly describes the data. However, the ratio to the neutral pion is also provided and can be parametrized with the ratio of two functional forms that describe particle spectra with a separation of the soft and hard part of the spectrum. The superposition of the two parts is used to construct the particle ratio as a function of transverse momentum. The functional form is:

$$\frac{\phi}{\pi^0}(p_T) = \frac{C \cdot \exp\left(\frac{\beta p_T - m_\phi}{T\sqrt{1-\beta^2}}\right) + N \cdot C_{s/h} \cdot \left(1 + \left(\frac{p_T}{p_0}\right)^2\right)^{-n}}{C \cdot \exp\left(\frac{\beta p_T - m_{\pi^0}}{T\sqrt{1-\beta^2}}\right) + C_{s/h} \cdot \left(1 + \left(\frac{p_T}{p_0}\right)^2\right)^{-n}}, \quad (7.6)$$

where $C_{s/h}$ is a relative normalization between the soft and the hard part of the parametrization and N is the constant ratio between the two particle spectra that is approached at high transverse momenta. The soft part of the spectra is described by a blast wave inspired function that depends on the flow velocity β and the kinetic freeze-out temperature T .

Exemplarily, the π^0 and η parametrizations are shown together with the measured spectra in figures 7.1 and 7.2, respectively. Since a particular functional form is used to describe the measured spectrum in the respective range in transverse momentum, a systematic uncertainty has to be estimated due to the required extrapolation to larger transverse momenta. This is done by a transverse momentum dependent shift of the measured points prior to the parametrization of the spectra. The different parametrizations that are obtained are also shown in the left and right panels of figures 7.1 and 7.2, compared to the standard fit. The procedure that is used to determine the systematic uncertainty on the cocktail simulation is described in more detail in section 8.2. Similar figures can be found for all other measured particles in appendix A.3, with the exception of the ϕ , where the parametrized ratio to the neutral pion is shown. The parametrization of the ϕ spectrum, that is ultimately used in the decay simulation, is obtained by multiplying the parametrization of the ratio with the parametrization of the neutral pion.

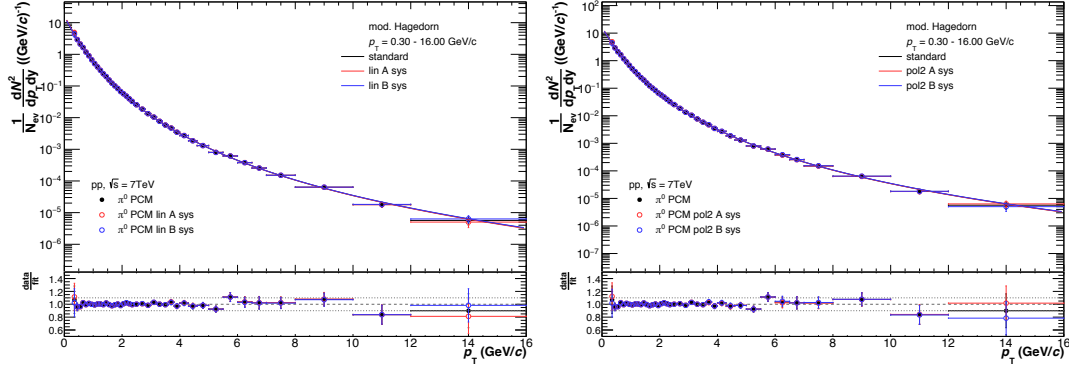


Figure 7.1.: Modified Hagedorn parametrization of the measured neutral pion spectrum including a linear (left) and polynomial second order (right) variation of the data points.

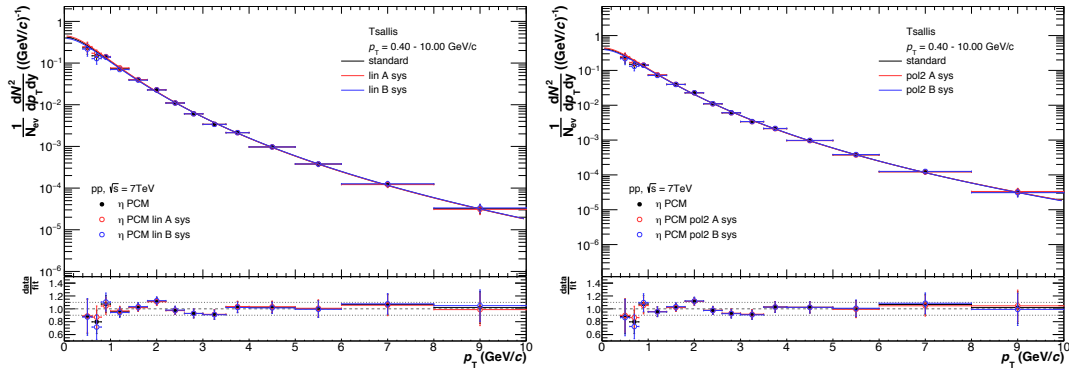


Figure 7.2.: Tsallis parametrization of the measured η spectrum including a linear (left) and polynomial second order (right) variation of the data points.

7.2. Decay Simulation

The decay photon spectrum is calculated from a simulation of the decays of the generated mother particles. Hereby the mother particles are produced randomly, following a flat distribution of the rapidity in $|y| < 1.0$ and a flat distribution of the azimuthal angle in between $0 \leq \phi \leq 2\pi$. The particles are also generated randomly from a flat distribution of the transverse momentum in the range $0.0 \text{ GeV}/c \leq p_T \leq 50.0 \text{ GeV}/c$, with the parametrizations applied as a weight to reduce statistical fluctuations, especially at high p_T . The generated range in transverse momentum is much larger than the range that will be analyzed to account for the decays to particles with lower momenta. In total, 80.5×10^6 mother particles per species included in the simulation were produced.

Figure 7.3 shows the spectra of the generated mother particles as well as the ratio of the spectra to the neutral pion for mesons and to the proton for baryons. It can be seen, that the neutral pion dominates up to a transverse momentum of about $3 \text{ GeV}/c$, where it is approached by the distributions of particles whose parametrizations are obtained from m_T scaling, like the ρ^0 or ρ^\pm . The ratio to protons is shown for baryons in the

right panel of figure 7.3 to reveal the same effect.

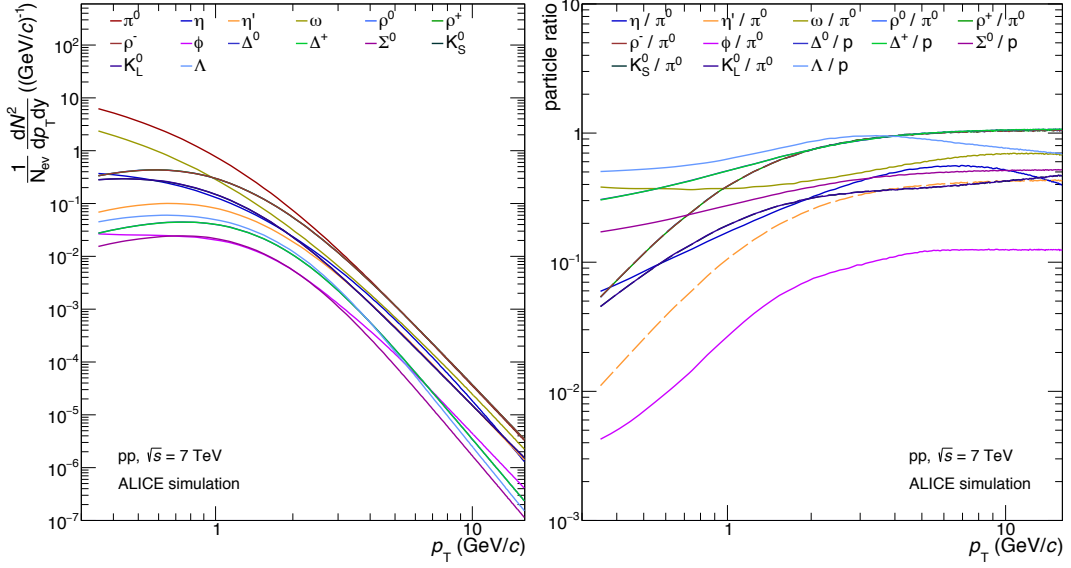


Figure 7.3.: Spectra of mother particles included in the decay simulation (left) and ratios to the neutral pion or proton (right).

After the generation, the decays of the mother particles are simulated with the PYTHIA 6.4 decay algorithms that are included in the AliRoot framework, using the branching ratios that are listed in table 7.1. The decay algorithms follow the full decay chain, allowing for the determination of the secondary spectra with the same framework that is used for the decay photon cocktail. However, for the decay photon cocktail, only direct decays into photons are considered according to the definition of primary particles.

The kinematic trees that are produced by the decay simulation are further analyzed to extract the spectra. The parametrizations that are used as an input for the simulation are already fully corrected, thus no further corrections have to be applied on the spectra that are obtained from the analysis of the simulation. However, the simulation is done in a rapidity range that exceeds the fiducial region chosen for the analysis, in order to account for decays with a larger opening angle that might occur close to the edges of the fiducial zone. Therefore, the extraction of the decay particle spectra is restricted to the same fiducial region that is used in the measurement.

7.3. Photon Cocktail Results and Validation

The decay photon cocktail is the sum of all decay photon spectra from the different mother particles. Figure 7.4 shows the decay photon spectra that are obtained from the simulation and the fractions of decay photons from different sources to the full cocktail. The right panel of figure 7.4 shows, that the neutral pion is by far the largest source of decay photons, providing about 80% of the cocktail. The second largest contribution originates in η decays and enters the full cocktail, depending on the transverse

momentum, with a maximum of about 10%. The rest of the decay photon cocktail is distributed amongst the remaining sources with the ω and η' being the third and fourth largest contributors.

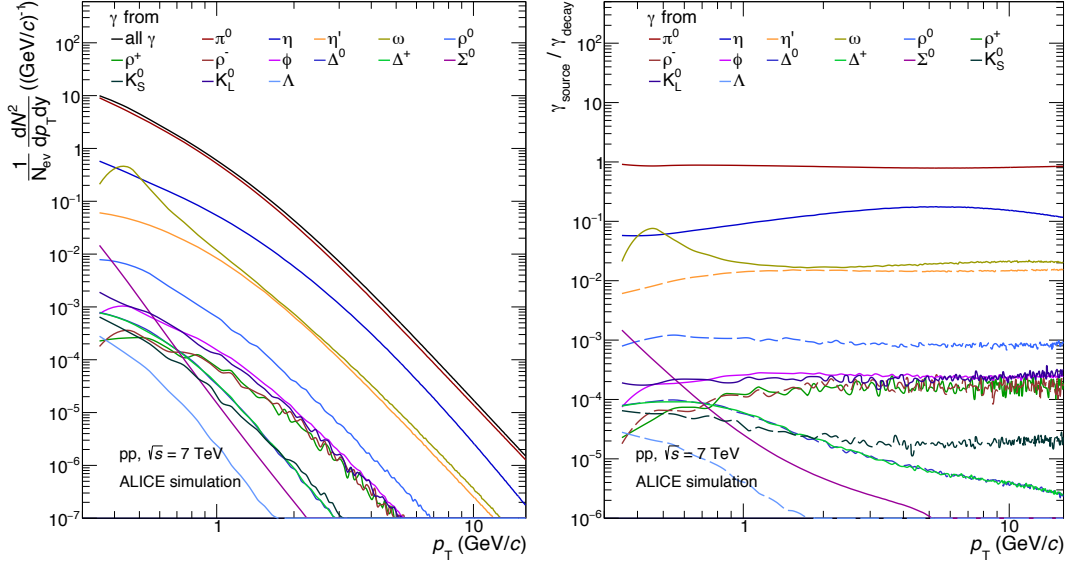


Figure 7.4.: Decay photon spectra from the decay simulation (left) and fraction of the different sources to the full cocktail (right).

The decay photon cocktail is not directly used in the photon double ratio, but divided by the neutral pion spectrum which provides an overall normalization between the measured inclusive photon spectrum and the decay photon spectrum obtained from the cocktail simulation. This, in principle, would cover possible differences between the measured neutral pion spectrum and the one that is generated in the simulation. However, the cocktail simulation is anchored to the measured π^0 spectrum and most of the decay photons originate from neutral pion decays. Thus, possible differences between the generated and measured neutral pion spectra might translate into an incorrect decay photon spectrum. The comparison of the generated and the measured neutral pion spectrum is therefore a crucial cross check of the simulation procedure. The measured and the generated spectra are shown in figure 7.5, where the measured neutral pion spectrum is reconstructed with the conversion method, corresponding to the spectrum that was used in the parametrization. It can be seen, that both spectra agree very well with slight differences at the lower and upper end of the p_T range. The observed differences are not crucial and can be explained with the diminished statistics for the signal extraction in the lowest and highest p_T bin in the data.

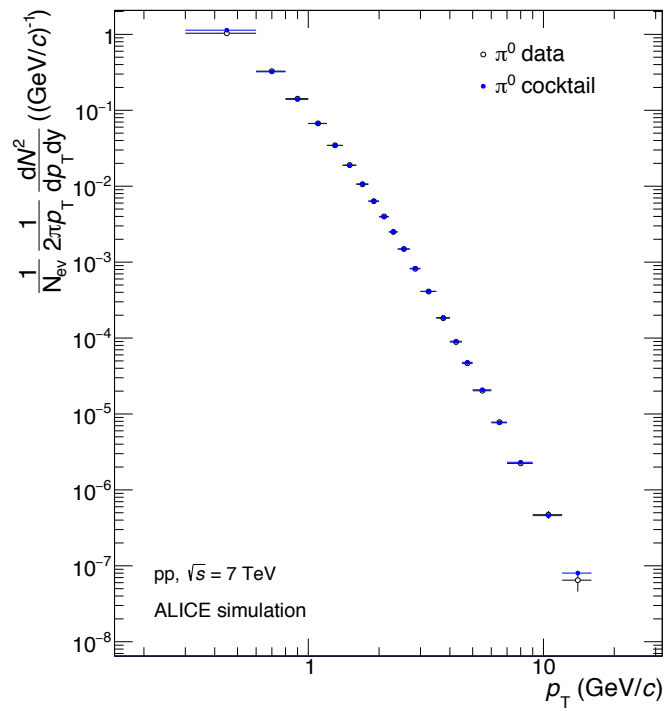


Figure 7.5.: Generated and measured neutral pion spectra.

8. Direct Photons

The extraction of direct photons is based on three cornerstones, that are the inclusive photon spectrum, the inclusive neutral pion spectrum and the decay photon cocktail, described in sections 5, 6 and 7, respectively. The three ingredients are then combined according to the direct photon excess ratio, or photon double ratio, that was originally defined in equation 2.9:

$$R_\gamma = \frac{(\gamma_{\text{inc.}}(p_\text{T})/\pi^0(p_\text{T}))_{\text{meas.}}}{(\gamma_{\text{dec.}}(p_\text{T})/\pi^0(p_\text{T}))_{\text{sim.}}} \approx \frac{\gamma_{\text{inc.}}(p_\text{T})}{\gamma_{\text{dec.}}(p_\text{T})}, \quad (8.1)$$

where, by definition, $R_\gamma \geq 1$ and the approximate equality is valid if the neutral pion spectra coincide. A direct photon signal is observed if the double ratio shows a significant excess above unity and the direct photon spectrum can be calculated according to equation 2.10.

In this chapter, the direct photon excess ratio is presented for the two photon reconstruction methods that are used. The determination of the systematic uncertainties for the measurement with the conversion method is described. No systematic uncertainties are calculated for the calorimeter measurement. Furthermore, upper limits for the direct photon spectrum are presented since no significant excess is observed.

8.1. Direct Photon Excess Ratio

The approximate equality in equation 8.1 mostly holds for the conversion measurement, as it is shown in figure 7.5, due to the use of the neutral pion spectrum reconstructed from photon conversions as an input for the cocktail simulation. However, the most dominant reason to calculate the photon double ratio according to equation 8.1 is the partial cancellation of the systematic uncertainties, i.e. the material budget in the conversion measurement. The material budget is, over a large part of the transverse momentum range, the most prominent source of systematic uncertainties in the conversion measurement. It is assumed, that the material budget enters the systematic uncertainty once with each photon and thus twice in the neutral pion measurement. Therefore it naturally cancels once when the double ratio is calculated, significantly reducing systematic uncertainty.

The numerator of the direct photon excess ratio is given by the inclusive photon to neutral pion ratio, calculated from the measured and corrected spectra. In contrast, the denominator is taken from the decay simulation with the decay photon cocktail being divided by the spectrum of generated neutral pions. Both, the numerator and the denominator of the the direct photon excess ratio, are shown in figure 8.1 for both photon reconstruction methods that were used. In the case of the conversion measurement, the systematic uncertainties of the inclusive ratio are shown and both ratios coincide within

the uncertainties. The same is not true for the calorimeter measurement, where the decay ratio exceeds the inclusive ratio over a large part of the transverse momentum range.

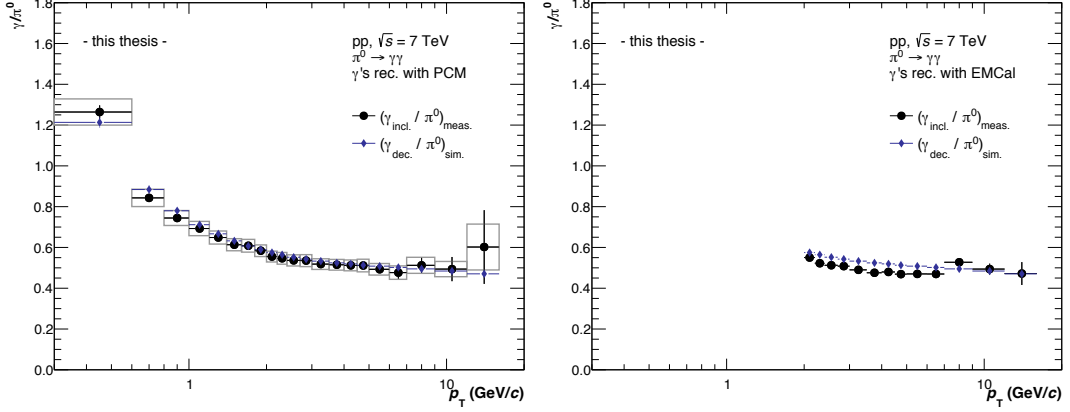


Figure 8.1.: Inclusive photon to neutral pion ratio and decay photon to neutral pion ratio from the cocktail simulation for the conversion (left) and calorimeter (right) measurement.

The direct photon excess ratios, calculated according to equation 8.1, are shown in figure 8.2 for the two reconstruction methods. In the case of the conversion method, the systematic uncertainty that is determined on double ratio is shown. The double ratio that is obtained for the conversion measurement is consistent with unity within the systematic uncertainties. No significant excess and thus no direct photon signal is observed. Additionally, the direct photon excess ratio is compared to next-to-leading order (NLO) pQCD calculations [63] for direct photons. The calculations of the direct photon spectrum are translated into a direct photon excess ratio according to:

$$R_{\gamma,\text{pQCD}} = 1 + \frac{\gamma_{\text{dir. pQCD}}}{\gamma_{\text{dec.}}} \quad (8.2)$$

Figure 8.1 shows that the measurement agrees with the prediction within the uncertainties. Towards higher transverse momenta, the prediction of the direct photon spectrum rises due to the increasing importance of photons originating in hard processes. These photons are also expected to be present in proton-proton collisions and a rise of the central values with p_T can be observed, but the uncertainties are still consistent with unity. In the case of the calorimeter measurement, the direct photon excess ratio takes values below one for a large part of the transverse momentum range. However, no statement about the agreement with unity can be done without an evaluation of the systematic uncertainties of the measurement. Compared to the conversion method, the calorimeter measurement can be additionally suppressed due to the worse transverse momentum resolution.

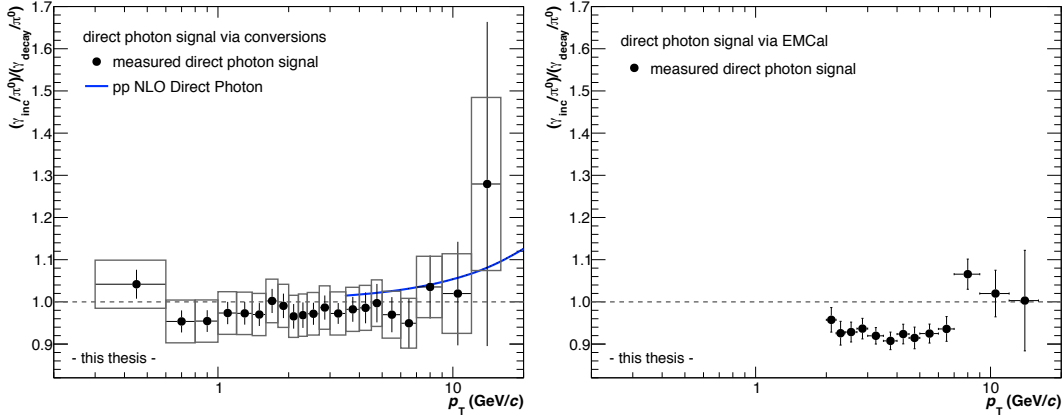


Figure 8.2.: Direct photon excess ratio from the conversion (left) and calorimeter (right) measurement and NLO pQCD calculation [63], translated to the direct photon excess ratio according to equation 8.2.

8.2. Systematic Uncertainties

The systematic uncertainties on the conversion measurement are evaluated in this section, while the systematic uncertainties on the calorimeter measurement are omitted. This is due to the fact, that the reconstruction with the calorimeter was a first attempt at the measurement using the EMCAL and further detailed investigations are required before attempting to estimate the systematic uncertainties. The systematic uncertainties are determined for the inclusive photon spectrum, the inclusive photon to neutral pion ratio and the direct photon excess ratio, which dominates the total systematic uncertainty of the direct photon spectrum. However, the direct photon spectrum can only be estimated in terms of upper limits and therefore no associated systematic uncertainties are calculated.

Several distinct sources of systematic uncertainties are considered, that apply differently on the measured quantities. A basic source of systematic uncertainties is a non-perfect coincidence between the measured data and the anchored MC simulations. This manifests itself in a dependence of the invariant yields on the specific selections that are applied in the reconstruction. If the data would be perfectly reproduced by the simulations, no dependence on the invariant yields on the specific set of cuts is expected since the corrections would exactly reproduce the behavior in the data. The different sources of systematic uncertainties that are considered are introduced in the following paragraphs, pointing out how they affect the different measured quantities, i.e. the invariant photon yield, the invariant photon to neutral pion spectrum and the direct photon excess ratio.

Material Budget The conversion probability of photons depends on the amount of material that is crossed. This is not perfectly known for the ALICE detector and therefore has to be considered as a systematic uncertainty when photons are reconstructed from the conversion into an electron-positron pair in the detector material. The conversion probability is determined from MC simulations and depends on the implementation

of the detector as well as the correct description of the processes, corresponding to the data. The discrepancy between the simulations and the experiment was studied in [64] and determined to be 4.5%, also including a variation of the rapidity range and the use of different event generators. The uncertainty is constant over the full range in transverse momentum and is assumed to apply twice on the neutral pion due to the reconstruction from a conversion photon pair. Hence, it is assumed to cancel once in the inclusive photon to neutral pion ratio and therefore only enters the direct photon excess ratio with 4.5%.

Corrections from Monte Carlo Simulations If the underlying characteristics of the measurement, e.g. the V0 finding efficiency and the tracking, are not perfectly reproduced by the data, the invariant photon and neutral pion yields will depend on the specific selections that were applied in the reconstruction. In this paragraph, only the selections used to obtain the photon sample are considered with the neutral pion specifics discussed in the next paragraph. The uncertainty attributed to this is determined by variations of the selection cuts and the comparison to the fully corrected quantities using the standard cuts on the basis of the invariant photon spectrum and the inclusive photon to neutral pion ratio directly in order to allow for (partial) cancellation of the uncertainties that is expected since the variations will affect the photon and neutral pion spectra most likely not to the same magnitude but in the same direction. Thus, the systematic uncertainties arising from this source are calculated for the invariant photon spectrum and the invariant photon to neutral pion ratio, respectively. The uncertainty is determined on a bin-by-bin basis with the mean of the maximum deviations in the positive and negative direction assigned as the systematic uncertainty attributed to the cut that is varied. The cuts that are considered in the variation belong to the three selections that were used to obtain the measured photon sample: 1) track selection criteria in the V0 finding process, 2) particle identification using the TPC dE/dx information of the tracks and 3) cuts to select photon conversions from the initial sample of V0s.

All cut variations that are considered in the calculation of systematic uncertainties from this group are summarized in table 8.1. The geometric cuts that were applied to select the fiducial detector region are not considered in the variation since they are included in the material budget uncertainty.

Neutral Pion Signal Extraction The neutral pions are reconstructed, in the conversion method, from a pair of photons measured via conversion in the detector material. Therefore, all cuts applied on the photon sample also affect the neutral pions, as discussed in the previous paragraph. However, an additional selection is applied to select photon pairs for the neutral pion reconstruction. This is the photon energy asymmetry that, while essentially left open in the standard selection, can produce a systematic uncertainty if not perfectly reproduced by the simulations. Furthermore, the neutral pion signal is extracted by an integration of the signal peak in the invariant mass distributions. Thus, the invariant neutral pion yield can depend on the integration window if the resolution in MC does not match the data. The related systematic uncertainty is estimated using two additional integration windows, narrower and wider than standard,

and determining the effect on the invariant yield. An additional source of systematic uncertainty in the signal extraction is the normalization of the combinatorial background, which is determined with an event mixing procedure. In the standard approach, the high-mass end of the invariant mass distributions is used to scale the combinatorial background. Hence, the low-mass end is used in comparison for the normalization to estimate the associated systematic uncertainty.

Both systematic uncertainties related to the neutral pion signal extraction are calculated directly on the invariant photon to neutral pion ratio. Again, the mean of the maximum deviations from the standard in both directions is calculated for each transverse momentum bin and taken as the systematic uncertainty. The variations that are considered are summarized in table 8.1, with the different signal peak integration ranges listed in table 8.2.

Cut variations				
	standard	variation 1	variation 2	variation 3
track selection				
min. track p_T	$> 0.05 \text{ GeV}/c$	$> 0.040 \text{ GeV}/c$	$> 0.075 \text{ GeV}/c$	$> 0.1 \text{ GeV}/c$
$N_{\text{cluster TPC}}/$ $N_{\text{findable clusters}}$	$> 60\%$	$> 35\%$	$> 70\%$	
min. R_{conv}	$> 5 \text{ cm}$	$> 2.8 \text{ cm}$	$> 10 \text{ cm}$	
particle identification				
$\sigma_{dE/dx,e}$	$-3 < n\sigma_e < 5$	$-4 < n\sigma_e < 5$	$-2.5 < n\sigma_e < 4$	
$p_{\text{min},\pi\text{rej.}}$	$0.4 \text{ GeV}/c$	$0.25 \text{ GeV}/c$	$0.5 \text{ GeV}/c$	
$p_{\text{max},\pi\text{rej.}}$	$3.5 \text{ GeV}/c$	$2.0 \text{ GeV}/c$	$5.0 \text{ GeV}/c$	
$n\sigma_{dE/dx,\pi\text{ rej.}}$				
low p	$n\sigma_\pi > 1$	$n\sigma_\pi > 2$	$n\sigma_\pi > 0$	
high p	$n\sigma_\pi > -10$			
photon selection				
max. q_T	$< 0.05 \text{ GeV}/c$ (2D)	$< 0.07 \text{ GeV}/c$ (1D)	$< 0.03 \text{ GeV}/c$ (2D)	$< 0.05 \text{ GeV}/c$ (1D)
$\chi_{\text{red.}}^2$	< 30	< 50	< 20	
Ψ_{Pair}	< 0.1 (2D)	< 0.2 (2D)	< 0.05 (2D)	< 0.1 (1D)
$\cos(\theta_{\text{point.}})$	> 0.85	> 0.75	> 0.9	
neutral pion signal extraction				
α meson	< 1	< 0.85	< 0.75	

Table 8.1.: Cutvariations for systematic error evaluation.

π^0 signal peak integration ranges		
standard	narrow	wide
$[M_{\pi^0} - 0.035 \text{ GeV}/c^2,$ $M_{\pi^0} + 0.010 \text{ GeV}/c^2]$	$[M_{\pi^0} - 0.015 \text{ GeV}/c^2,$ $M_{\pi^0} + 0.005 \text{ GeV}/c^2]$	$[M_{\pi^0} - 0.055 \text{ GeV}/c^2,$ $M_{\pi^0} + 0.025 \text{ GeV}/c^2]$

Table 8.2.: Neutral pion signal peak integration ranges for systematic error evaluation.

Out-of-Bunch Pileup Correction The estimation of the contribution from out-of-bunch pileup to the measured photon sample is done with an empirical method to determine the background under the signal peak in the DCA_z distributions in transverse momentum bin. Hereby, the method is chosen in such a way that the background is optimally described but the procedure nevertheless inherits a certain arbitrariness. Therefore, a systematic uncertainty has to be determined. This is done by using two different background extraction methods to estimate the contribution from out-of-bunch pileup. The different background estimates for photons from category one and two are shown in appendix A.1 in transverse momentum bins. Additionally, the relative contribution from out-of-bunch pileup is shown in figure 8.3 for the different background estimation methods versus the transverse momentum. The standard method for separate categories is used for the determination of the invariant photon yield and the two variations shown are used for the calculation of the systematic uncertainty. The standard method is also shown for all categories combined. However, this is not used since the category-wise extraction of the background is more reasonable and the difference to the method used is covered in the systematic uncertainty. The final uncertainty is again calculated directly on the invariant photon yield and the invariant photon to neutral pion ratio from the mean of the maximum deviations in both directions using the two variations.

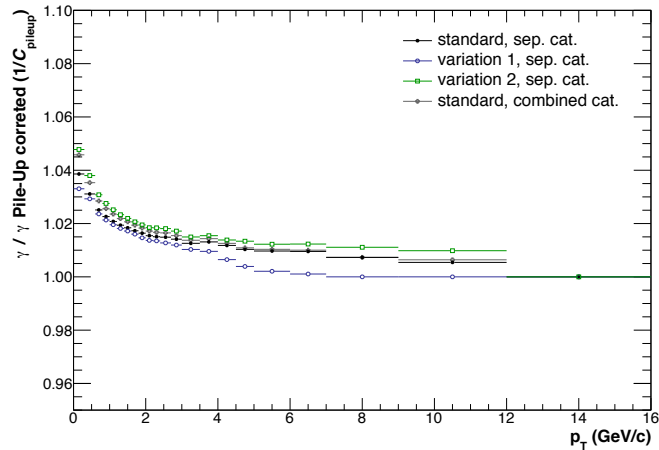


Figure 8.3.: Relative contribution from out-of-bunch pileup to the measured photon spectrum, where the background is estimated with different extraction methods.

Decay Photon Cocktail The simulation of the decay photon cocktail is anchored to the data through a parametrization of the measured spectra. The choice of a specific functional form combined with the extrapolation of the parametrization outside the measured range in transverse momentum pose a source of systematic uncertainty on the simulated decay photon spectrum. Furthermore, the systematic uncertainties of the measured spectra can enter the systematic uncertainty of the decay photon cocktail. Therefore, the calculation of the systematic uncertainty of the cocktail is based on the

systematic uncertainties of the input spectra, separating constant and p_T dependent uncertainties. The two main contributors to the cocktail are the π^0 and the η , which both were measured with the conversion method from the decay into two photons. Therefore, both spectra are assigned with a constant systematic uncertainty of 9% that is given by the material budget. This uncertainty only poses a constant offset to the cocktail calculation and therefore cancels in the calculation of the double ratio, where the decay photon spectrum is divided by the neutral pions from the simulation. The p_T dependent systematic uncertainties, that are the remaining systematic uncertainties after the subtraction of the constant part for the π^0 and the η , on all measured spectra are used to shift the data points with different slopes before the parametrization. The systematic uncertainties that are used for the shift are multiplied with different p_T dependent factors that are shown exemplarily for the neutral pion in figure 8.4. Two forms were chosen to enhance the deviation from the standard parametrization in different regions. The first form is linear with p_T , resulting in a maximum shift of the points with the full p_T dependent systematic uncertainty in the lowest bin in one direction and in the highest bin in the opposite direction. The second form is a polynomial second order that forces a maximum shift in the same direction in the lowest and highest bin as well as a maximum shift in the opposite direction at the center of the measured range. Each form gives two variations, once in one direction and inverted. To each variation of the points, a set of parametrizations is obtained that estimate the maximum deviation from the standard parametrization in terms of slope, especially covering the transverse momenta outside the measured range, where the parametrizations are not anchored to the data points. The different parametrizations that are obtained for the measured spectra are shown in figures 7.1 and 7.2 as well as in appendix A.3. The full cocktail is then produced for each variation and the systematic uncertainty is calculated on the direct photon excess ratio with the same variations in the decay photon spectrum and the neutral pion spectrum from the simulation. The overall systematic uncertainty attributed to the cocktail simulation is the mean value of the maximum deviation of both methods from the standard in both directions, evaluated on a bin-by-bin basis.

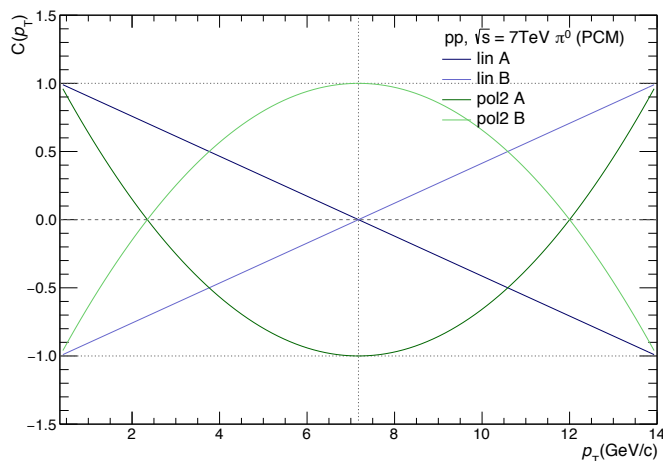


Figure 8.4.: Factor applied on the p_T dependent part of the systematic uncertainty of the neutral pion spectrum for the shift of the data points.

Additionally, a systematic uncertainty attributed to the transverse momentum scaling of the spectra lacking a measurement could be considered. However, since the neutral pion dominates the decay photon cocktail, this effect is negligible and is therefore not included in the systematic uncertainty of the cocktail calculation. Nevertheless, the spectra are also scaled from the modified parametrizations, including a certain variation of the slope.

The systematic uncertainties on the invariant photon yield, the inclusive photon to neutral pion ratio and the direct photon excess ratio are shown in figure 8.5. The total systematic uncertainty is obtained from the quadratic sum of the individual contributions. The systematic uncertainty on the inclusive photon spectrum is dominated by the material budget over the full range in transverse momentum. The remaining sources contribute almost equally to the total systematic uncertainty with the exception of the track related cuts. The inclusive photon to neutral pion spectrum is dominated by the material budget at low transverse momenta. Above a transverse momentum of about 6 GeV/ c , the systematic uncertainty related to the photon selection exceeds the material budget and dominates the total systematic uncertainty. The systematic uncertainty on the direct photon excess ratio is shown in the bottom panel of figure 8.5. The uncertainties were smoothed in order to decrease the statistical fluctuations which inevitably enter due to the determination on the basis of the photon double ratio. Again, the uncertainty is dominated by the material budget at lower transverse momenta and by the photon selection at higher transverse momenta. Compared to the systematic uncertainty of the inclusive photon to neutral pion ratio, an additional contribution enters with the decay photon cocktail. However, the decay photon cocktail only contributes with 1% to the total systematic uncertainty.

8.3. Direct Photon Spectrum

The direct photon excess ratio, measured with the conversion method, is consistent with unity within the systematic uncertainties over the full range in transverse momentum. Thus, no significant excess is observed and therefore the direct photon spectrum can not be determined. At low transverse momenta, this is consistent with the expectation of no thermal photon contribution in minimum bias proton-proton collisions. To higher transverse momenta, where the contribution from prompt and fragmentation photons is more distinct, an excess of the central values can be observed, but the measurement is still consistent with unity within the uncertainties.

Thus, the calculation of the direct photon spectrum is not possible. However, upper limits on the direct photon yield are calculated and shown in figure 8.6 for the conversion measurement. The same can not be done in the case of the calorimeter measurement due to the lack of knowledge on systematic uncertainties of the corresponding excess ratio. Due to resolution effects and the reconstruction procedure, the measured direct photon excess ratio can take values below one. This seems to be in disagreement with the definition of the excess ratio, which only allows for (real) values equal or larger than one by definition. The use of a Bayesian approach in the calculation of the upper limits exploits this knowledge by an appropriate choice of the prior. Hence, the probability

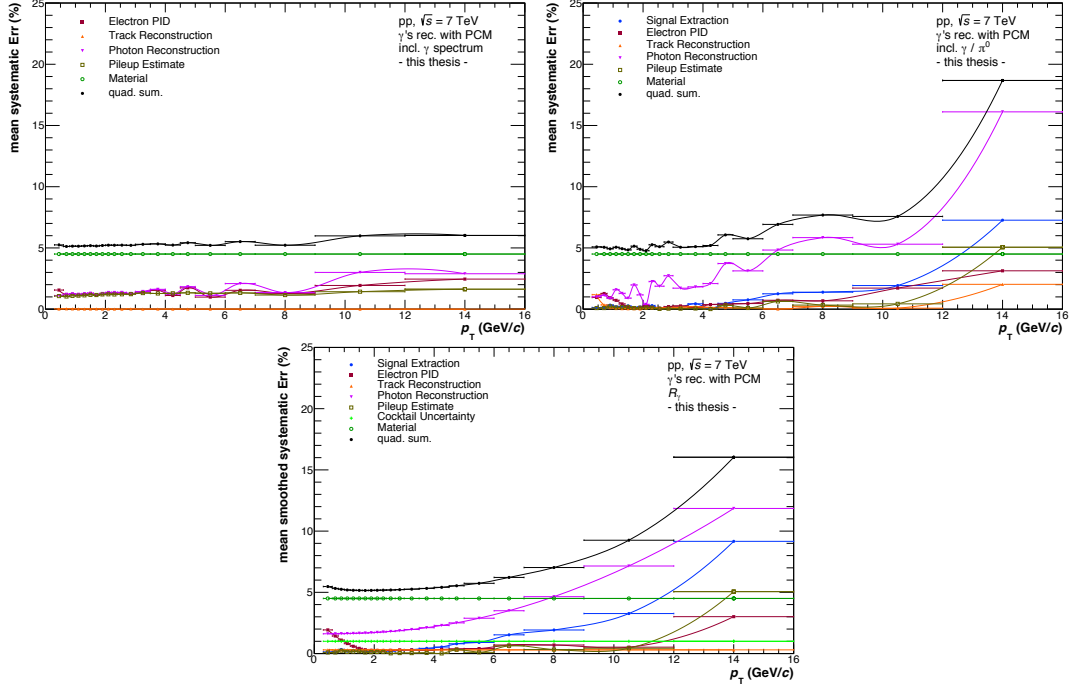


Figure 8.5.: Systematic uncertainties on the inclusive photon spectrum (top left), the inclusive photon to neutral pion ratio (top right) and the direct photon excess ratio (bottom).

for a certain real value of the direct photon excess ratio is given by:

$$P(R_\gamma^{\text{true}} | R_\gamma^{\text{meas.}}) \propto P(R_\gamma^{\text{meas.}} | R_\gamma^{\text{true}}) \cdot \Pi(R_\gamma^{\text{true}}), \quad (8.3)$$

where $R_\gamma^{\text{meas.}}$ refers to the measured value and $\Pi(R_\gamma^{\text{true}})$ is the prior that is used. The prior is given by the Heaviside function and can be written as:

$$\Pi(R_\gamma^{\text{true}}) = \Theta(R_\gamma^{\text{true}} - 1), \quad (8.4)$$

which is one for $R_\gamma^{\text{true}} > 1$ and zero everywhere else. Thus, the definition of the direct photon excess ratio is accounted for by the prior in the Bayesian approach.

The upper limits are defined as 95% confidence level and are calculated in transverse momentum bins according to:

$$\mathcal{N} \int_{-\infty}^{R_\gamma^{95\%CL}} dR_\gamma^{\text{true}} G(R_\gamma^{\text{true}}; R_\gamma^{\text{meas.}}, \sigma_{\text{tot.}}) \Theta(R_\gamma^{\text{true}} - 1) = 95\%, \quad (8.5)$$

where $G(R_\gamma^{\text{true}}; R_\gamma^{\text{meas.}}, \sigma_{\text{tot.}})$ is a Gaussian distribution with the mean given by the measured value of the direct photon excess ratio, $R_\gamma^{\text{meas.}}$, in the corresponding p_T bin. The width of the Gaussian distribution is given by the quadratic sum of the statistical and systematic uncertainty. The integral over the complete space in R_γ^{true} is normalized to one by the normalization constant \mathcal{N} . Thus, the upper limits $R_\gamma^{95\%CL}$ are extracted

by solving equation 8.5, which is given in transverse momentum bins. The upper limits on the direct photon spectrum are calculated from the upper limits on the excess ratio:

$$\gamma_{\text{dir.}}^{95\% \text{CL}}(p_T) = \gamma_{\text{incl.}}(p_T) \cdot \left(1 - \frac{1}{R_\gamma^{95\% \text{CL}}(p_T)} \right), \quad (8.6)$$

This is conceptually equivalent to the definition given in equation 2.10, but depends on the upper limits that were obtained for the direct photon excess ratio rather than the measured values. The upper limits on the direct photon spectrum are shown in figure 8.6 and compared to the pQCD predictions for the direct photon spectrum. It can be seen that the prediction is in qualitative agreement with the upper limits that were obtained. The agreement seems to get worse towards lower transverse momenta, where the prediction approaches $R_\gamma = 1$, as it can be seen in figure 8.2. Thus, the upper limits on the direct photon spectrum seem to exceed the prediction, if extrapolated towards vanishing p_T .

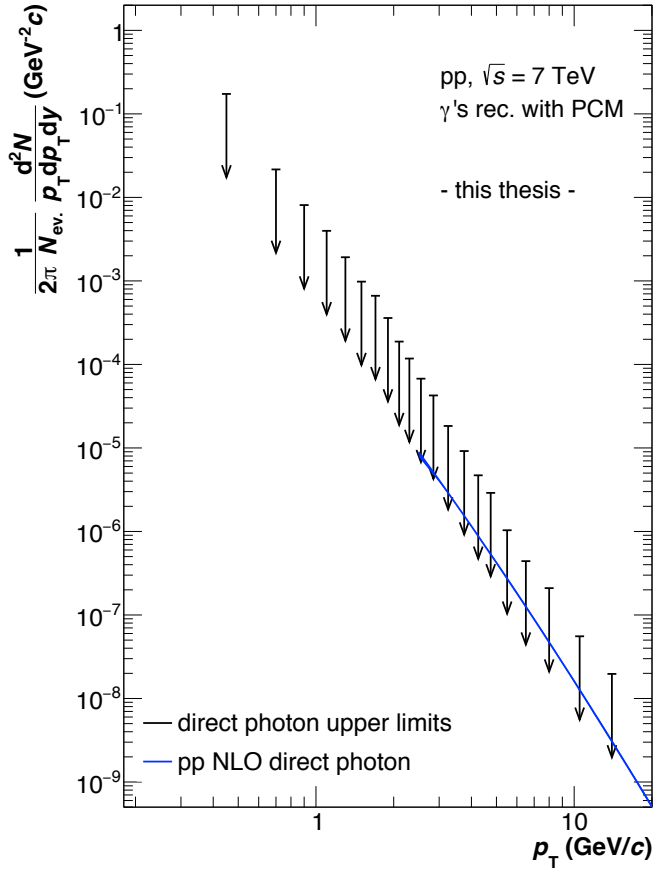


Figure 8.6.: Direct photon spectrum 95% confidence level upper limits for the conversion measurement and NLO pQCD prediction for the direct photon spectrum [63].

9. Summary

In this thesis, the measurement of direct photons in proton-proton collisions at center-of-mass energies of $\sqrt{s} = 7$ TeV with the ALICE detector was presented. Hereby, two different methods for the photon reconstruction were used, i.e. the photon conversion method and the reconstruction in the EMCal. The measurement in proton-proton collisions provide a deeper understanding of the hard production processes of photons as well as an important baseline for measurements in heavy-ion collisions. The direct photon signal was quantified with the direct photon excess ratio and no significant excess was observed with either method. Thus, upper limits on the direct photon spectrum were calculated for the measurement with the conversion method, which are in agreement with NLO pQCD calculations of the direct photon spectrum. The same could not be done for the calorimeter measurement since further detailed studies are required before attempting to evaluate the systematic uncertainties of the measurement.

The conversion measurement is a re-analysis of the measurement described in [1], using the most recent reconstruction pass available as well as an additional period in data and MC. The more recent reconstruction improves the data and the corresponding MC simulations and thus decreases the systematic uncertainty associated to the measurement. Due to the higher statistics of the sample, the measurement could be extended in transverse momentum, allowing to reach higher and lower p_T with reasonable uncertainties. Furthermore, a data-driven approach was used for the determination of the contributions from secondaries to the measured photon and neutral pion spectra. In figure 9.1, the direct photon excess ratio determined with the conversion method in this analysis is compared to the excess ratio calculated in [1]. Hereby, the transverse momentum binning of the previous analysis was used to calculate the double ratio and the corresponding systematic uncertainties. The labels correspond to the reconstruction pass of the data, with 'pass4' labeling the results of this work. The results agree within the uncertainties of the measurement and it can be seen that the systematic uncertainties were reduced over the full range in transverse momentum. Hereby, the improvement is most dramatic at higher transverse momenta. Additionally, the result shown in figure 8.2 extends the transverse momentum range of the previous measurement from 0.6 GeV/ c to 0.3 GeV/ c at the lower end and from 12.0 GeV/ c to 16.0 GeV/ c at the upper end.

The calorimeter measurement was a first attempt at the reconstruction of direct photons with the EMCal. The inclusive photon and neutral pion spectra were compared to the results from the conversion method, where differences of about 5% were observed. In the case of the neutral pion spectrum, the data-driven approach for the determination of the secondary contributions was not used since the secondary reconstruction efficiencies could not be extracted properly. The direct photon excess ratio obtained from the calorimeter measurement seems to be suppressed compared to the result of the conversion method. However, no definite statement about the agreement of the

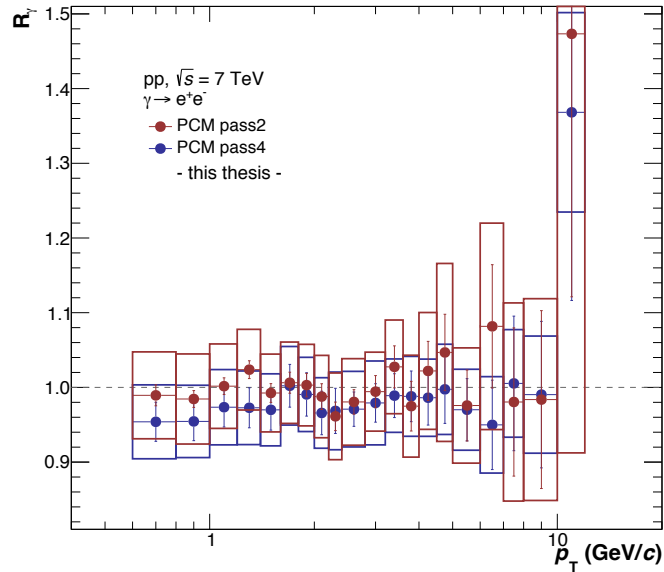


Figure 9.1.: Direct photon excess ratio from previous analysis [1] and result from this work. Pass2 refers to the previous reconstruction of the data while pass4 labels the results from this work.

excess ratios can be made without an evaluation of the systematic uncertainties of the calorimeter measurement. The transverse momentum assigned to a calorimeter cluster is calculated with respect to the primary vertex. Thus, resolution effects will have a stronger impact on the calorimeter measurement, especially concerning secondary particles which are produced with a larger displacement from the primary vertex. This could result in a non-perfect description of the secondary spectra and hence modify the invariant yields. The direct photon excess ratio can also be directly modified due to resolution effects on the inclusive photon and neutral pion spectra. An additional difficulty lies in the determination of the purity, which can be affected by the merging of electromagnetic showers in the calorimeter cells at larger transverse momenta. Further detailed studies are required to optimize the measurement and to determine reliable systematic uncertainties. However, it was shown that the measurement of the direct photon excess ratio can be performed with the EMCAL and additional investigations will help to improve the results.

10. Outlook

In the analysis presented in this work, the purity of the photon sample is determined solely based on information from the simulated events. Although the simulations are anchored to the data, differences are still present as it was shown in the calculation of the systematic uncertainties of the measurement. The purity, however, can also be determined with a data driven approach, as it was explored in [65]. This approach is tested for the reconstruction of photons with the conversion method and compared to the standard purity calculation. The 7 TeV dataset provides an optimal testing ground for the exploration of new methods to reduce the dependency on the MC simulations since the simulated particle spectra match the data reasonably well. This allows for a well defined comparison between data driven approaches and MC based corrections.

In the data driven approach for the purity estimation, the TPC dE/dx cut, that was used for the selection of V0 candidates with electron-positron tracks, is redefined to combine the information of each leg of the secondary vertex into a single variable. The first step in this direction is a relabeling of the $n\sigma$ variable used previously:

$$\kappa^\pm = \frac{dE/dx - \langle dE/dx|_{e^\pm} \rangle}{\sigma_{\langle dE/dx|_{e^\pm} \rangle}}. \quad (10.1)$$

The negative and positive charged tracks attributed to the conversion candidate are assigned with κ^- and κ^+ , respectively. While the cut on the deviation from the electron hypothesis was done separately for each track, the new variable can be used in a two dimensional way, combining the two legs of the V0 candidate. Real photon conversions, resulting in an electron-positron pair, are centered around $\kappa^\pm = 0$. Combinatorial background, where the V0 candidates consist of two tracks from different particle species, exhibit a displacement from the center in the $\kappa^+ - \kappa^-$ plane, as it was shown in [65].

The distinction between signal and combinatorial background is improved by combining the two κ^\pm variables into a single quantity:

$$K = \frac{|\kappa^+| + |\kappa^-|}{2} + 2 \cdot (\kappa^+ + \kappa^-), \quad (10.2)$$

where the first term averages the response for signal and background alike and the second term exploits the specific energy loss curves in the momentum region that is studied. The energy loss band of electrons is rather flat and the pions are clearly separated to lower values over a large part of the momentum range. Thus the κ^\pm values that are obtained will shift background contributions to lower values in K , further separating signal and background.

So far, the particle identification with the TPC was only translated into a different variable. The main advantage is the exploitation of K for a data driven approach to determine the purity of the photon sample. Therefore, the V0 candidates in MC are

combined into four different categories: 1) real electron-positron pairs, 2) electron-pion pairs, 3) pairs of oppositely charged pions and 4) remaining. These templates are calculated in transverse momentum bins and then fitted simultaneously to the total K distribution that is obtained from the data. This is shown in two exemplary transverse momentum bins in figure 10.1, where the four shaded distributions are the scaled MC templates and the line is the measured K distribution. It can be seen, that the signal peak is well separated from the pion-pion peak and mainly the pion-electron and remaining background distributions feed into the signal region. The scaling of the MC

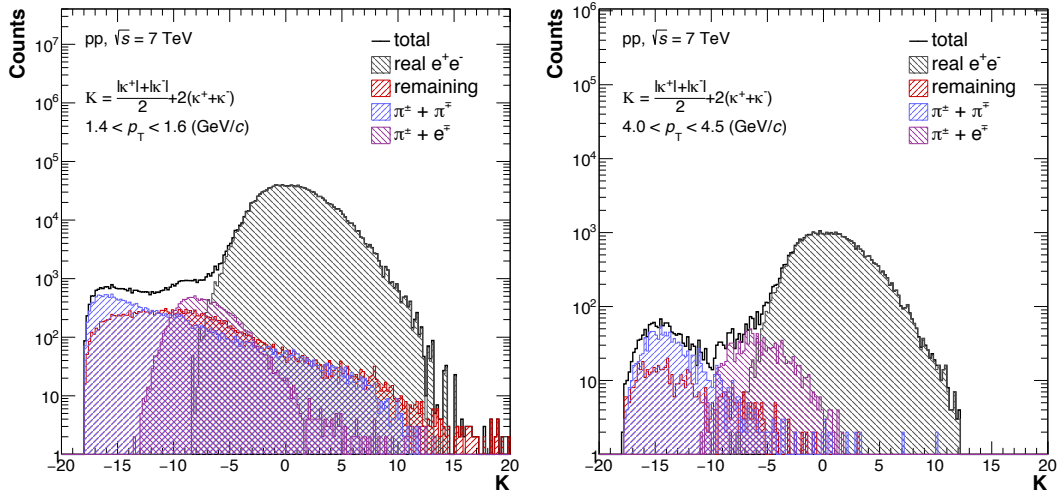


Figure 10.1.: K templates from MC and total distribution obtained from the data.

templates ensures, that the distributions that are obtained from the simulations reproduce the data. The purity of the photon sample is determined by dividing the integral of the signal peak by the integral of the background distributions in a selected K region. This K cut is then applied in the reconstruction of the photon sample, replacing the selection according to the TPC dE/dx . Different K cuts are explored and compared to the standard TPC dE/dx cut and the standard method to calculate the photon purity. The purities that are obtained from the data driven approach are shown in figure 10.2 and compared to the standard purity from MC. The purities obviously depend on the K selection, with a larger contribution from background for the largest K window. The purity from the standard MC method is comparable to the data driven purity that is obtained for the selection $-5 \leq K \leq 10$.

The invariant photon yields from the K selection and the standard TPC dE/dx method are compared in figure 10.3, with the respective purities being used. It should be noted, that the photon spectra shown in figure 10.3 are calculated without the use of the unfolding procedure. The unfolding relies on a much finer binning in transverse momentum, which complicates the scaling of the templates due to the reduced statistics. The resolution correction is therefore included in the reconstruction efficiency. However, this is not particularly crucial for the comparison of the two approaches since the spectra calculated with and without unfolding correspond very well. Additionally, the out-of-bunch pileup correction was omitted in both cases since the analysis of the specific

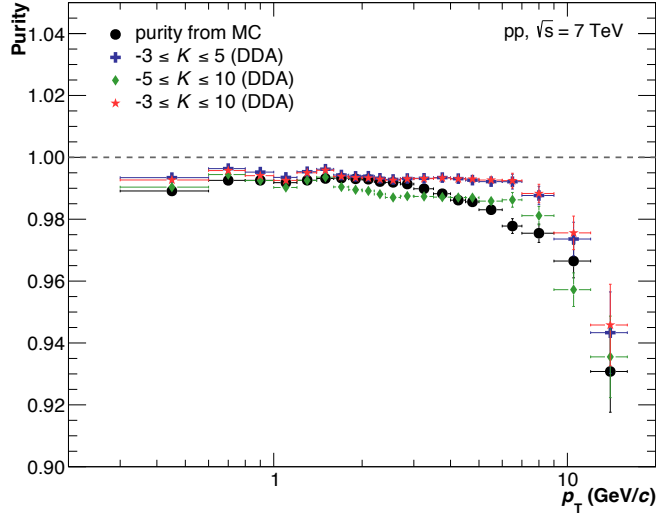


Figure 10.2.: Photon purities from data driven approach and standard method.

quantities required is very demanding in terms of memory. However, the contribution from out-of-bunch pileup is comparably small and was not considered for the standard and the data driven approach, thus the comparison of the spectra is not affected. The photon spectrum reconstructed with the standard purity method is well reproduced by the data driven purity method using the K selection above a transverse momentum of 0.6 GeV/ c . The spectrum using the MC purity approach is best reproduced by the data driven purity approach with the most open K cut. In the first transverse momentum bin, the differences between the different methods and the different K windows are largest due to the crossing of the electron and the pion band at low momenta. This makes the distinction between signal and background exceptionally difficult and the purity therefore heavily depends on the selection window.

It can be concluded that the data driven purity approach provides reasonable results that compare well to the standard MC purity approach. Since the particle spectra in data are very well reproduced by the MC simulations for proton-proton collisions, the comparison shown provides a suitable test of the method. However, to improve the stability of the method, all background sources that do not correspond to electron-pion or pion-pion pairs were grouped into one template. This can be dangerous since the different contributions that enter might inherit structures that are not accounted for by the fitting of the templates. Therefore, it could be possible that the background under the signal peak is not reasonably described, which translates into deviations between the photon purity in the data and the purity that is observed. This possible source of systematic uncertainty can be reduced by dividing the remaining background into different sub-groups and study those in more extensive detail, prior to the estimation of the purity.

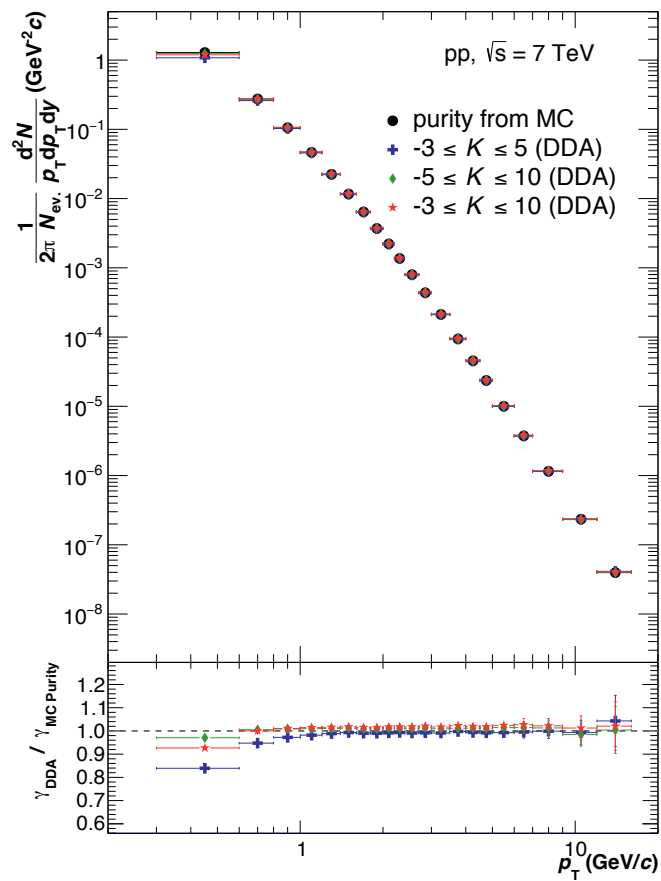


Figure 10.3.: Invariant photon yields for different K selections and the standard method.

A. Appendix

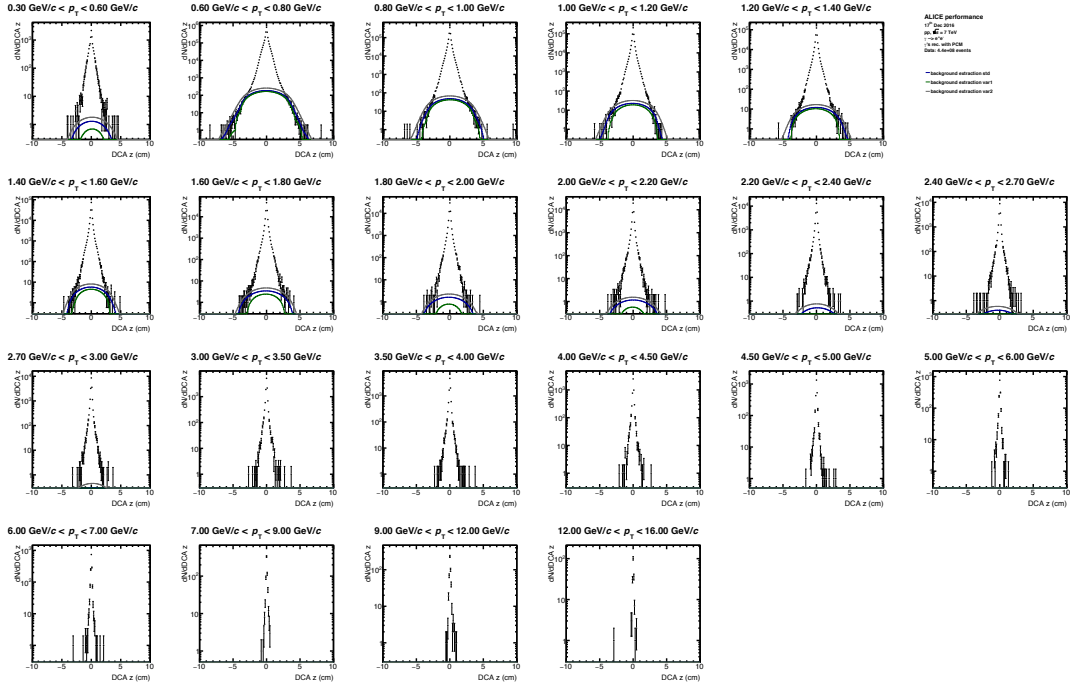


Figure A.2.: DCA_z distributions for photons from category two in p_T bins, including the out-of-bunch pileup background estimates.

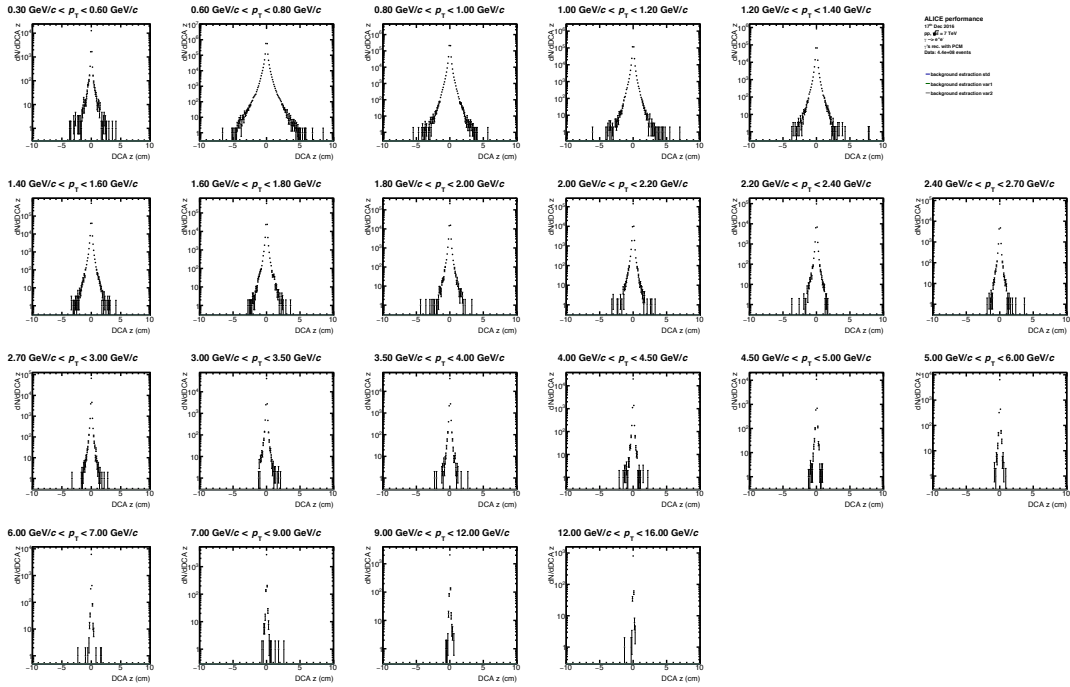


Figure A.3.: DCA_z distributions for photons from category three in p_T bins, where no out-of-bunch pileup is expected.

A.2. Neutral Pion Invariant Mass Distributions

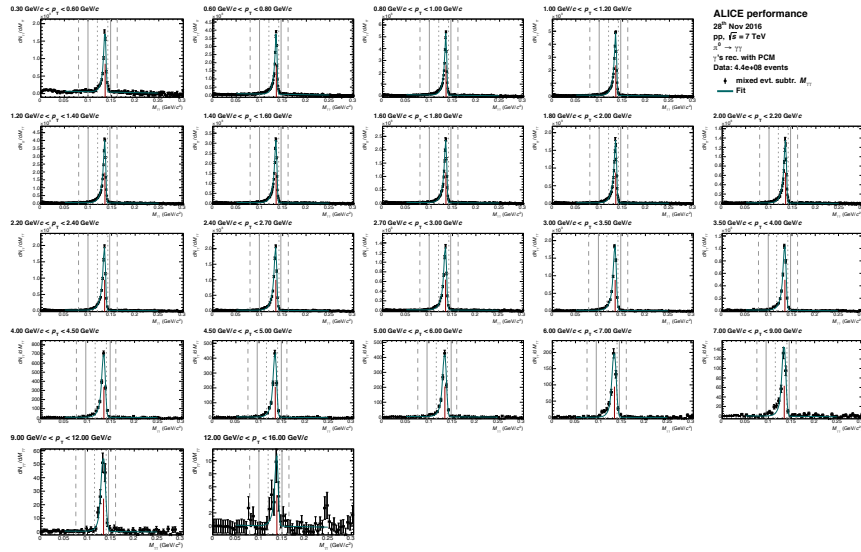


Figure A.4.: Invariant mass distribution of neutral pion candidates reconstructed with the conversion method after the background subtraction.

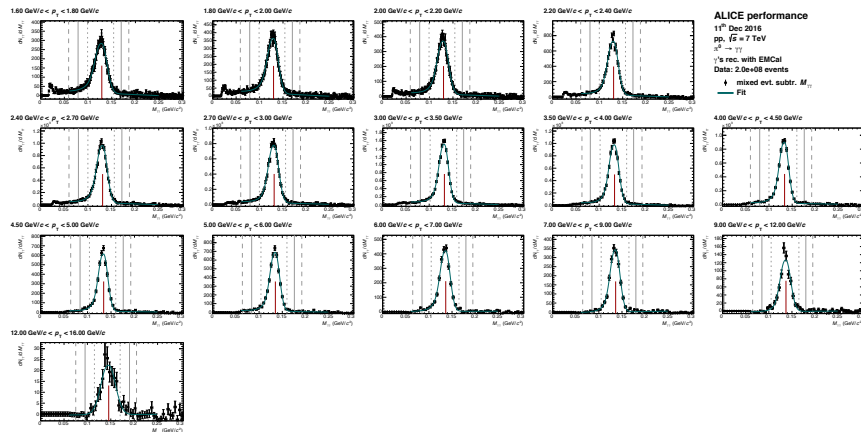


Figure A.5.: Invariant mass distribution of neutral pion candidates reconstructed with the calorimeter method after the background subtraction.

A.3. Cocktail Simulation Input Parametrizations

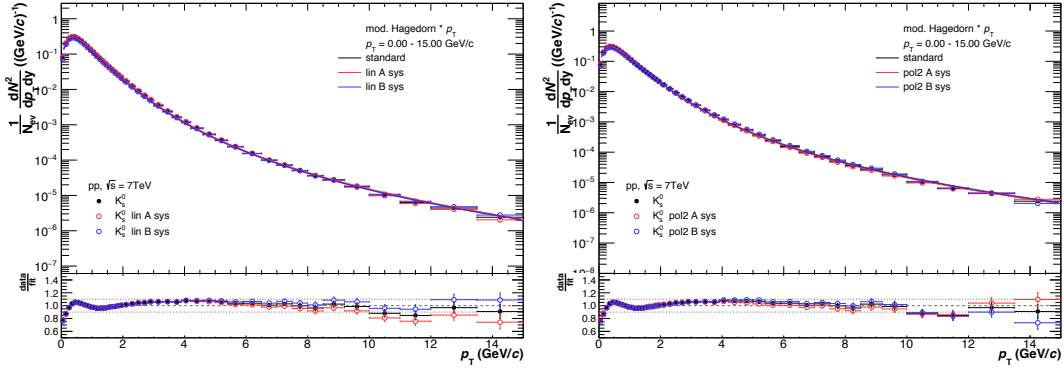


Figure A.6.: Measured K_S^0 spectrum with modified Hagedorn parametrization multiplied by p_T as well as linear (left) and polynomial second order (right) variation for the determination of the systematic uncertainty.

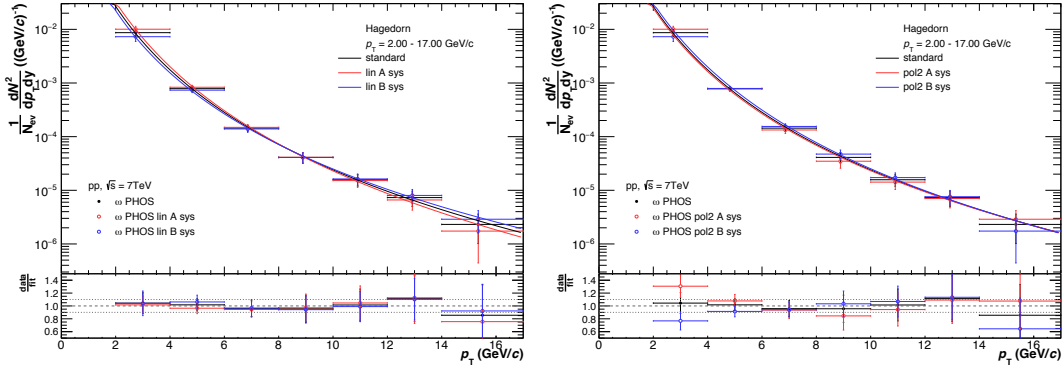


Figure A.7.: Measured ω spectrum with Hagedorn parametrization as well as linear (left) and polynomial second order (right) variation for the determination of the systematic uncertainty.

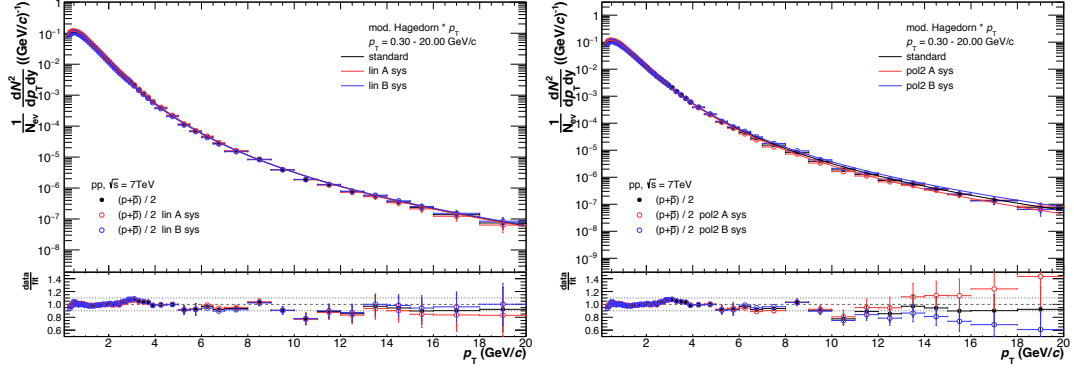


Figure A.8.: Measured proton spectrum with modified Hagedorn parametrization multiplied by p_T as well as linear (left) and polynomial second order (right) variation for the determination of the systematic uncertainty.

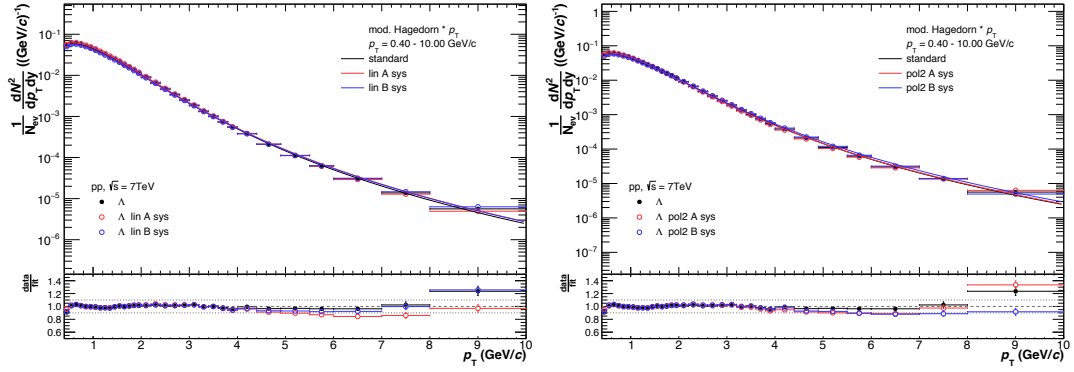


Figure A.9.: Measured Λ spectrum with modified Hagedorn parametrization multiplied by p_T as well as linear (left) and polynomial second order (right) variation for the determination of the systematic uncertainty.

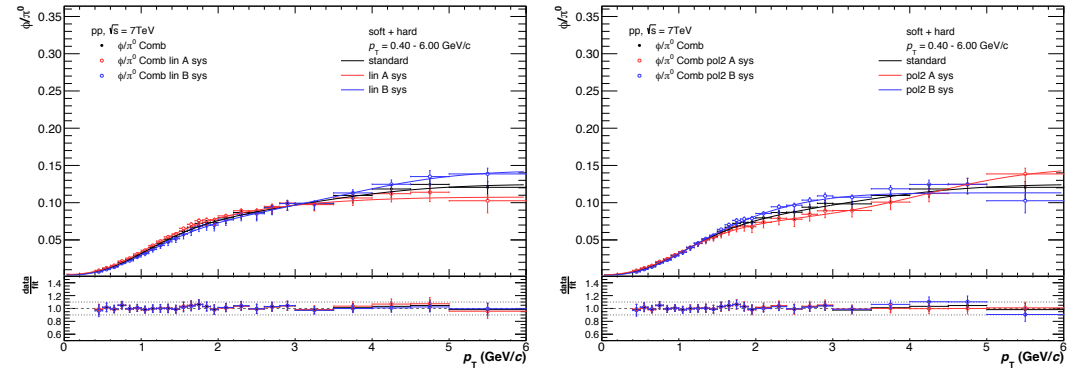


Figure A.10.: Measured ϕ to π^0 ratio with parametrization as well as linear (left) and polynomial second order (right) variation for the determination of the systematic uncertainty.

Bibliography

- [1] M. Wilde, “Measurement of direct photons in pp and pb-pb collisions with conversion pairs”, PhD thesis, University of Münster, 2015.
- [2] S. L. Glashow, “Partial-symmetries of weak interactions”, *Nuclear Physics* **22** (1961), no. 4, 579–588.
- [3] S. Weinberg, “A model of leptons”, *Phys. Rev. Lett.* **19** Nov (1967) 1264–1266.
- [4] A. Salam and J. C. Ward, “Weak and electromagnetic interactions”, *Il Nuovo Cimento Series 10* **11** (1959), no. 4, 568–577.
- [5] F. J. Hasert *et al.*, “Search for elastic muon-neutrino electron scattering”, *Physics Letters B* **46** (1973)a, no. 1, 121–124.
- [6] **Gargamelle Neutrino**, F. J. Hasert *et al.*, “Observation of neutrino like interactions without muon or electron in the gargamelle neutrino experiment”, *Phys. Lett.* **B46** (1973)b 138–140.
- [7] “Wikipedia.org: Standard Model”.
https://en.wikipedia.org/wiki/Standard_Model
- [8] **ATLAS**, G. Aad *et al.*, “Observation of a new particle in the search for the Standard Model Higgs boson with the ATLAS detector at the LHC”, *Physics Letters B* **716** (2012), no. 1, 1–29, 1207.7214.
- [9] K. Ranjan, “Observation of a new boson at the LHC with the CMS Experiment”, *Nuclear Physics B - Proceedings Supplements* **251-252** (2014) 129–134, 1207.7235.
- [10] **CMS**, V. Khachatryan *et al.*, “Constraints on parton distribution functions and extraction of the strong coupling constant from the inclusive jet cross section in pp collisions at $\sqrt{s} = 7$ TeV”, *Eur. Phys. J.* **C75** (2015), no. 6, 288, arXiv:1410.6765.
- [11] M. Thomson, “Modern particle physics”, Cambridge University Press, New York, 2013.
- [12] S. Bethke, “The 2009 world average of alpha s”, *European Physical Journal C* **64** (2009), no. 4, 689–703, 0908.1135.
- [13] D. J. Gross and F. Wilczek, “Ultraviolet behavior of non-abelian gauge theories”, *Physical Review Letters* **30** (1973)a, no. 26, 1343–1346, arXiv:1011.1669.

- [14] D. J. Gross and F. Wilczek, “Asymptotically free gauge theories. I”, *Physical Review D* **8** (1973)b, no. 10, 3633–3652, [arXiv:1011.1669](#).
- [15] H. D. Politzer, “Reliable perturbative results for strong interactions?”, *Physical Review Letters* **30** (1973), no. 26, 1346–1349.
- [16] R. Hagedorn, “Statistical thermodynamics of strong interactions at high energies”, *Nuovo Cimento, Suppl.* **3** (1965), no. CERN-TH-520, 147–186.
- [17] R. Fries and B. Müller, “Heavy ions at lhc: Theoretical issues”, *The European Physical Journal C - Particles and Fields* **34** (2004), no. 1, s279–s285.
- [18] B. J. Schaefer and M. Wagner, “On the QCD phase structure from effective models”, *Progress in Particle and Nuclear Physics* **62** (2009), no. 2, 381–385, [0812.2855](#).
- [19] P. Braun-Munzinger and J. Stachel, “The quest for the quark-gluon plasma”, *Nature* **448** (2007) 302–309.
- [20] F. Karsch, “Lattice QCD at high temperature and the QGP”, *AIP Conference Proceedings* **842** (2006), no. June, 20–28, [arXiv:0601013](#).
- [21] Y. Aoki, Z. Fodor, S. D. Katz, and K. K. Szabó, “The QCD transition temperature: Results with physical masses in the continuum limit”, *Physics Letters, Section B: Nuclear, Elementary Particle and High-Energy Physics* **643** (2006), no. 1, 46–54, [arXiv:0609068](#).
- [22] S. Borsanyi, G. Endrodi, Z. Fodor, A. Jakovac, S. D. Katz, S. Krieg, C. Ratti, and K. K. Szabo, “The QCD equation of state with dynamical quarks”, *JHEP* **11** (2010) 077, [arXiv:1007.2580](#).
- [23] J.-F. Paquet *et al.*, “Production of photons in relativistic heavy-ion collisions”, *Phys. Rev.* **C93** (2016), no. 4, 044906, [arXiv:1509.06738](#).
- [24] M. H. Thoma, “Damping rate of a hard photon in a relativistic plasma”, *Physical Review D* **51** (1995), no. 2, 862–865, [arXiv:9405309](#).
- [25] C. Gale, “Photon Production in Hot and Dense Strongly Interacting Matter”, [0904.2184](#).
- [26] **ALICE**, J. Adam *et al.*, “Direct photon production in Pb-Pb collisions at $\sqrt{s_{NN}} = 2.76$ TeV”, *Phys. Lett.* **B754** (2016), no. September, 235–248, [arXiv:1509.07324](#).
- [27] “The accelerator complex”, Jan 2012.
<http://cds.cern.ch/record/1997193>
- [28] L. Evans and P. Bryant, “LHC Machine”, *Journal of Instrumentation* **3** (2008), no. 08, S08001.
- [29] M. Benedikt, P. Collier, V. Mertens, J. Poole, and K. Schindl, “LHC Design Report vol.III: The LHC Injector Chain”, 2004.

-
- [30] C. Lefevre, “LHC the guide”, 2009, unpublished.
<http://home.web.cern.ch/about/accelerators/large-hadron-collider>
- [31] **ALICE**, “ALICE Webpage”.
<http://aliceinfo.cern.ch/>
- [32] **ALICE**, K. Aamodt *et al.*, “The ALICE experiment at the CERN LHC”, *Journal of Instrumentation* **Volume 3** (2008), no. 08, S08002.
- [33] J. Alme *et al.*, “The ALICE TPC, a large 3-dimensional tracking device with fast readout for ultra-high multiplicity events”, *Nuclear Instruments and Methods in Physics Research, Section A: Accelerators, Spectrometers, Detectors and Associated Equipment* **622** (2010), no. 1, 316–367, 1001.1950.
- [34] **ALICE**, P. Cortese *et al.*, “Alice electromagnetic calorimeter technical design report”, Tech. Rep. CERN-LHCC-2008-014. ALICE-TDR-14, Aug 2008.
- [35] **ALICE**, “AliRoot”. a.
<http://git.cern.ch/pubweb/AliRoot.git>
- [36] **ALICE**, “AliPhysics”. b.
<http://git.cern.ch/pubweb/AliPhysics.git>
- [37] “Root Webpage”.
<http://root.cern.ch>
- [38] S. Mrenna and P. Skands, “PYTHIA 6.4 Dedicated to the Memory of Bo Andersson”, 2006.
- [39] T. Sjöstrand, S. Mrenna, and P. Skands, “A brief introduction to PYTHIA 8.1”, *Computer Physics Communications* **178** (2008), no. 11, 852–867, 0710.3820.
- [40] R. Brun, F. Bruyant, M. Maire, A. C. McPherson, and P. Zandarini, “GEANT3”, 1987.
- [41] J. Allison *et al.*, “Geant4 developments and applications”, *IEEE Transactions on Nuclear Science* **53** (2006), no. 1, 270–278.
- [42] S. Agostinelli *et al.*, “GEANT4 - A simulation toolkit”, *Nuclear Instruments and Methods in Physics Research, Section A: Accelerators, Spectrometers, Detectors and Associated Equipment* **506** (2003), no. 3, 250–303, 1005.0727v1.
- [43] **ALICE**, B. B. Abelev *et al.*, “Performance of the ALICE experiment at the CERN LHC”, *International Journal of Modern Physics A* **29** (2014), no. 24, 1430044, 1402.4476.
- [44] **ALICE**, B. Alessandro *et al.*, “ALICE: Physics Performance Report, Volume II”, *Journal of Physics G: Nuclear and Particle Physics* **32** (2006), no. 10, 1295–2040.
- [45] H. Bethe, “Zur Theorie des Durchgangs schneller Korpuskularstrahlen durch Materie”, *Annalen der Physik* **397** (1930) 325–400.

- [46] F. Bloch, “Zur Bremsung rasch bewegter Teilchen beim Durchgang durch Materie”, *Annalen der Physik* **408** (1933) 285–320.
- [47] T. Dahms, “Measurement of photons via conversion pairs with the PHENIX experiment at RHIC”, Master’s thesis, Stony Brook University, 2005.
- [48] T. Awes, F. Obenshain, F. Plasil, S. Saini, S. Sorensen, and G. Young, “A simple method of shower localization and identification in laterally segmented calorimeters”, *Nuclear Instruments and Methods in Physics Research Section A: Accelerators, Spectrometers, Detectors and Associated Equipment* **311** (1992), no. 1, 130 – 138.
- [49] Mühlheim, Daniel Michael, “Neutral meson measurements with EMCal in ALICE in pp collisions at 8 TeV”, 2016.
<https://aliceinfo.cern.ch/Notes/node/489>
- [50] **Particle Data Group**, K. A. Olive *et al.*, “Review of Particle Physics”, *Chin. Phys.* **C38** (2014) 090001.
- [51] “Proceedings, PHYSTAT 2011 Workshop on Statistical Issues Related to Discovery Claims in Search Experiments and Unfolding, CERN, Geneva, Switzerland 17-20 January 2011”, CERN. CERN, Geneva, 2011.
- [52] T. Adye, “Unfolding algorithms and tests using RooUnfold”, in “Proceedings, PHYSTAT 2011 Workshop on Statistical Issues Related to Discovery Claims in Search Experiments and Unfolding, CERN, Geneva, Switzerland 17-20 January 2011”, pp. 313–318, CERN. CERN, Geneva, 2011. [arXiv:1105.1160](https://arxiv.org/abs/1105.1160).
- [53] N. Schmidt, “Neutral meson and direct photon measurements with conversions in ALICE in proton-proton collisions at $\sqrt{s} = 7$ and 8 TeV”, Master’s thesis, University of Heidelberg. *work in progress*.
- [54] N. Schmidt, “Neutral meson measurements with PCM in ALICE in pp collisions at 8 TeV”, 2016.
<https://aliceinfo.cern.ch/Notes/node/567>
- [55] D. M. Mühlheim, PhD thesis, University of Münster. *work in progress*.
- [56] **WA80**, R. Albrecht *et al.*, “Production of eta mesons in 200-A/GeV S+S and S+Au reactions”, *Phys. Lett.* **B361** (1995) 14–20, [arXiv:hep-ex/9507009](https://arxiv.org/abs/hep-ex/9507009).
- [57] **ALICE**, J. Adam *et al.*, “Measurement of pion, kaon and proton production in proton-proton collisions at $\sqrt{s} = 7$ TeV”, *Eur. Phys. J.* **C75** (2015), no. 5, 226, [arXiv:1504.00024](https://arxiv.org/abs/1504.00024).
- [58] Riabov, Viktor, “Omega production measured in the $\pi^+\pi^-\pi^0$ channel in pp collisions at 7 TeV”, 2012.
<https://aliceinfo.cern.ch/Notes/node/90>
- [59] **ALICE**, B. Abelev *et al.*, “Production of $K^*(892)^0$ and $\phi(1020)$ in pp collisions at $\sqrt{s} = 7$ TeV”, *Eur. Phys. J.* **C72** (2012) 2183, [arXiv:1208.5717](https://arxiv.org/abs/1208.5717).

- [60] **ALICE**, J. Adam *et al.*, “Multiplicity-dependent enhancement of strange and multi-strange hadron production in proton-proton collisions at $\sqrt{s} = 7$ TeV”, [arXiv:1606.07424](#).
- [61] **PHENIX**, A. Adare *et al.*, “Detailed measurement of the e^+e^- pair continuum in $p + p$ and Au+Au collisions at $\sqrt{s_{NN}} = 200$ GeV and implications for direct photon production”, *Phys. Rev.* **C81** (2010) 034911, [arXiv:0912.0244](#).
- [62] J. Cleymans and D. Worku, “Relativistic Thermodynamics: Transverse Momentum Distributions in High-Energy Physics”, *Eur. Phys. J.* **A48** (2012) 160, [arXiv:1203.4343](#).
- [63] L. E. Gordon and W. Vogelsang, “Polarized and unpolarized isolated prompt photon production beyond the leading order”, *Phys. Rev.* **D50** (1994) 1901–1916.
- [64] F. Bock, “ALICE Capabilities for Studying Photon Physics with the Conversion Method at LHC Energies”, Bachelor’s thesis, University of Heidelberg, 2010.
- [65] M. Sas, “Neutral Mesons and Direct Photon Flow”, Master’s thesis, University of Utrecht, 2016.

Acknowledgements

I would like to thank Prof. Klaus Reygers for the opportunity to work on this very interesting topic and deepen my understanding of photons in particular as well as particle and high-energy physics in general. I would also like to thank my second referee, Prof. Stephanie Hansmann-Menzemer, since I realize that it also requires quite some time and work to read through the thesis. Furthermore, I would like to thank the Photon Conversion Group in general for the lively discussion and Friederike Bock, Daniel Mühlheim and Nicolas Schmidt in particular for the pleasant, though efficient, collaboration. I learned a lot about physics and the work in the field and I'm grateful for that. I would also like to thank my office colleagues Lucia Leardini and Meike Danisch for the great working atmosphere and enjoyable discussions, be it on physics topics or otherwise.

Last but not least, I would like to express my gratitude towards my friends, family and my girlfriend. Thank you for the motivation and the support.

Erklärung:

Ich versichere, dass ich diese Arbeit selbstständig verfasst habe und keine anderen als die angegebenen Quellen und Hilfsmittel benutzt habe.

Heidelberg, den 20.12.2016

.....